Oxidative Medicine and Cellular Longevity

Redox: a Bridge to Inflammation in Neurodegenerative Diseases

Lead Guest Editor: Xiaolei Shi
Guest Editors: Alok Shiomurti Tripathi, Fang Zongping, and Wang Liao

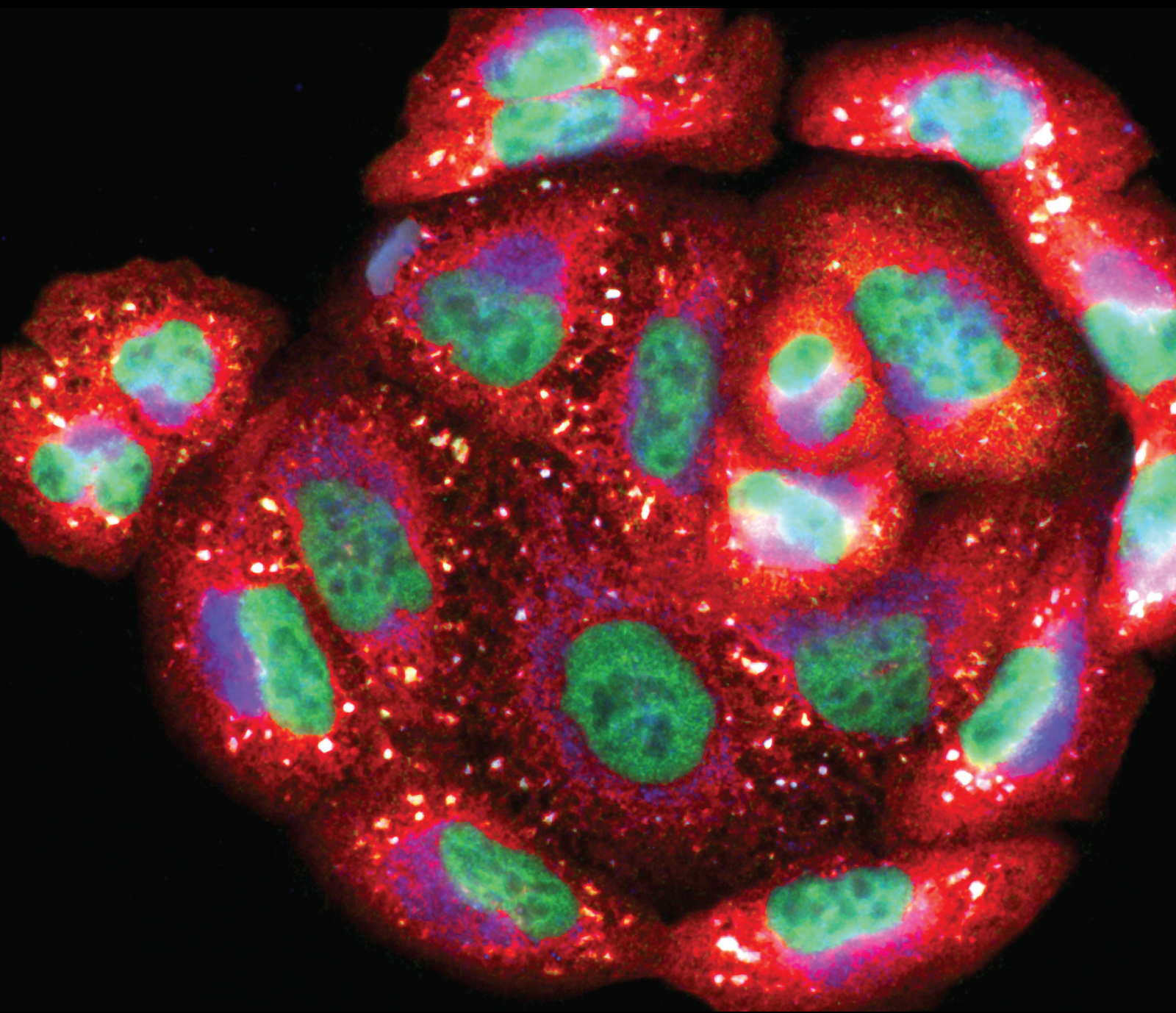

Redox: a Bridge to Inflammation in Neurodegenerative Diseases

Oxidative Medicine and Cellular Longevity

Redox: a Bridge to Inflammation in Neurodegenerative Diseases

Lead Guest Editor: Xiaolei Shi
Guest Editors: Alok Shiomurti Tripathi, Fang Zongping, and Wang Liao

Chief Editor

Jeannette Vasquez-Vivar, USA

Associate Editors

Amjad Islam Aqib, Pakistan
Angel Catalá, Argentina
Cinzia Domenicotti, Italy
Janusz Gebicki, Australia
Aldrin V. Gomes, USA
Vladimir Jakovljevic, Serbia
Thomas Kietzmann, Finland
Juan C. Mayo, Spain
Ryuichi Morishita, Japan
Claudia Penna, Italy
Sachchida Nand Rai, India
Paola Rizzo, Italy
Mithun Sinha, USA
Daniele Vergara, Italy
Victor M. Victor, Spain

Academic Editors

Ammar AL-Farga, Saudi Arabia
Mohd Adnan, Saudi Arabia
Ivanov Alexander, Russia
Fabio Altieri, Italy
Daniel Dias Rufino Arcanjo, Brazil
Peter Backx, Canada
Amira Badr, Egypt
Damian Bailey, United Kingdom
Rengasamy Balakrishnan, Republic of Korea
Jiaolin Bao, China
Ji C. Bihl, USA
Hareram Birla, India
Abdelhakim Bouyahya, Morocco
Ralf Braun, Austria
Laura Bravo, Spain
Matt Brody, USA
Amadou Camara, USA
Marcio Carocho, Portugal
Peter Celec, Slovakia
Giselle Cerchiaro, Brazil
Arpita Chatterjee, USA
Shao-Yu Chen, USA
Yujie Chen, China
Deepak Chhangani, USA
Ferdinando Chiaradonna, Italy
Zhao Zhong Chong, USA
Fabio Ciccarone, Italy
Alin Ciobica, Romania
Ana Cipak Gasparovic, Croatia
Giuseppe Cirillo, Italy
Maria R. Ciriolo, Italy
Massimo Collino, Italy
Manuela Corte-Real, Portugal
Manuela Curcio, Italy
Domenico D'Arca, Italy
Francesca Danesi, Italy
Claudio De Lucia, USA
Damião De Sousa, Brazil
Enrico Desideri , Italy
Francesca Diomede, Italy
Raul Dominguez-Perles, Spain
Joël R. Drevet, France
Grégory Durand, France
Alessandra Durazzo, Italy
Javier Egea, Spain
Pablo A. Evelson, Argentina
Mohd Farhan, USA
Ioannis G. Fatouros, Greece
Gianna Ferretti, Italy
Swaran J. S. Flora, India
Maurizio Forte, Italy
Teresa I. Fortoul, Mexico
Anna Fracassi , USA
Rodrigo Franco, USA
Juan Gambini, Spain
Gerardo García-Rivas, Mexico
Husam Ghanim, USA
Jayeeta Ghose, USA
Rajeshwary Ghosh, USA
Lucia Gimeno-Mallench , Spain
Anna M. Giudetti, Italy
Daniela Giustarini, Italy
José Rodrigo Godoy, USA
Saeid Golbidi, Canada
Guohua Gong, China
Tilman Grune, Germany
Solomon Habtemariam, United Kingdom
Eva-Maria Hanschmann, Germany
Md Saquib Hasnain, India
Md Hassan, India

Contents

Hindawi
Oxidative Medicine and Cellular Longevity
Volume 2022, Article ID 5583512, 22 pages
https://doi.org/10.1155/2022/5583512

Research Article

Rosiglitazone Ameliorates Spinal Cord Injury *via* Inhibiting Mitophagy and Inflammation of Neural Stem Cells

Qingqi Meng,[1] **Zhiteng Chen**,[2] **Qingyuan Gao**,[2] **Liqiong Hu**,[3] **Qilong Li**,[2] **Shutai Li**,[2] **Lili Cui**,[4] **Zhencheng Feng**,[1] **Xingliang Zhang**,[5,6] **Shiyun Cui**,[7] **and Haifeng Zhang**[2,8]

[1]*Department of Orthopedics, Guangzhou Red Cross Hospital, Jinan University, Guangzhou 510220, China*
[2]*Department of Cardiology, Sun Yat-sen Memorial Hospital, Sun Yat-sen University, Guangzhou 510120, China*
[3]*Department of Intensive Care Unit, Guangzhou Red Cross Hospital, Jinan University, Guangzhou 510220, China*
[4]*Guangdong Key Laboratory of Age-Related Cardiac and Cerebral Diseases, Institute of Neurology, The Affiliated Hospital of Guangdong Medical University, Zhanjiang 524001, China*
[5]*Institute of Pediatrics, Department of Pediatric Surgery, Shenzhen Children's Hospital, Shenzhen 518038, China*
[6]*Department of Pediatrics, The Affiliated Hospital of Guangdong Medical University, Zhanjiang 524001, China*
[7]*Department of Oncology, The First Affiliated Hospital of Nanjing Medical University, Nanjing 210029, China*
[8]*Laboratory & Medical Research Center, Sun Yat-sen University, Guangzhou 510275, China*

Correspondence should be addressed to Xingliang Zhang; xinglang_zhang@163.com, Shiyun Cui; cuishiyun@njmu.edu.cn, and Haifeng Zhang; hetven_chang@163.com

Received 5 February 2021; Revised 3 October 2021; Accepted 14 November 2021; Published 4 January 2022

Academic Editor: Xiaolei Shi

Background. Neurodegenerative diseases, such as Alzheimer's disease, and traumatic brain and spinal cord injury (SCI) are prevalent in clinical practice. Inhibition of hyperactive inflammation and proliferation of endogenous neural stem cells (NSCs) is a promising treatment strategy for SCI. Our previous studies demonstrated the beneficial effects of rosiglitazone (Rosi) on SCI, but its roles in inflammation inhibition and proliferation of NSCs are unknown. *Methods*. SCI in a rat model was established, and the effects of Rosi on motor functions were assessed. The effects of Rosi on NSC proliferation and the underlying mechanisms were explored in details. *Results*. We showed that Rosi ameliorated impairment of moto functions in SCI rats, inhibited inflammation, and promoted proliferation of NSCs *in vivo*. Rosi increased ATP production through enhancing glycolysis but not oxidative phosphorylation. Rosi reduced mitophagy by downregulating PTEN-induced putative kinase 1 (PINK1) transcription to promote NSC proliferation, which was effectively reversed by an overexpression of PINK1 *in vitro*. Through KEGG analysis and experimental validations, we discovered that Rosi reduced the expression of forkhead box protein O1 (FOXO1) which was a critical transcription factor of PINK1. Three FOXO1 consensus sequences (FCSs) were found in the first intron of the PINK1 gene, which could be potentially binding to FOXO1. The proximal FCS (chr 5: 156680169–156680185) from the translation start site exerted a more significant influence on PINK1 transcription than the other two FCSs. The overexpression of FOXO1 entirely relieved the inhibition of PINK1 transcription in the presence of Rosi. *Conclusions*. Besides inflammation inhibition, Rosi suppressed mitophagy by reducing FOXO1 to decrease the transcription of PINK1, which played a pivotal role in accelerating the NSC proliferation.

1. Introduction

Neurodegenerative diseases are chronic central nervous system diseases caused by the loss of neurons or their myelin sheath. Common examples include Alzheimer's disease and traumatic brain or spinal cord injury (SCI) [1–3]. SCI is a devastating medical condition that leads to the deterioration of health and substantial consumption of healthcare resources [4]. The initial neural tissue disruption during SCI can trigger secondary damage and extensive inflammatory reactions, leading to cell death at the injury site. Also, SCI triggers the active form of proinflammatory cytokines such as

interleukin-1 beta (IL-1β) to initiate neuroinflammation [5, 6]. SCI can be a complication of numerous insults (e.g., trauma and compression for various reasons), leading to new neurologic damage. It is associated with a poor prognosis, and thousands of individuals are affected by this condition each year. Therefore, SCI is one of the most severe neurologic disorders, and its treatment has been a significant challenge.

Following SCI, transplanting neural stem cells (NSCs)/neural progenitor cells (NPCs) is a promising strategy to enhance neuro-regeneration. Unfortunately, the survival of grafted NSCs/NPCs after SCI is dissatisfactory. Therefore, it is crucial to develop new methods to increase the survival of NSCs/NPCs [7]. The repair of SCI largely depends on the proliferation of NSCs/NPCs [8, 9]. In mice, the lack of spinal cord NSCs exacerbates proinflammatory cytokine expression and cripples neuronal cell survival and functional recovery [10]. Although many studies have explored effective strategies to accelerate the proliferation of NSCs, only a few of them have been of practical importance [11]. Among the strategies with potential clinical significance, thiazolidinediones (TZDs) may be the most promising. TZDs, a class of heterocyclic compounds consisting of a five-membered C_3NS ring, are classical antidiabetic drugs. They ameliorate insulin resistance by activating peroxisome proliferator-activated receptor-gamma (PPAR-γ). Rosiglitazone (Rosi) is one of the extensively used TZDs, and our previous study demonstrated its role in improving limb function in SCI rats [12]. However, the underlying mechanisms are still elusive.

Considering the great importance of NSC proliferation in SCI therapies, there were some preliminary explorations about the role of TZDs on it. Some studies have reported the effects of TZDs on mitochondrial functions, which are vital for stem cell survival and proliferation. For example, Rosi protects the NSCs against various toxicities *via* mitochondria-related inflammation and apoptosis [13–15]. Mitophagy is an essential biological process that modulates mitochondria-related oxidation and inflammation [16–18]. The maturation of mitophagy increases fatty acid utilization and decreases glucose utilization [19], which often implies a reduction in proliferation. This is particularly important for NSCs because they are highly dependent on glycolysis for maintaining their growth and homeostasis [20, 21]. Indeed, mitophagy is associated with the repressed proliferation of some stem cells and malignant cells [22, 23]. The association between TZDs and mitophagy is unknown. Therefore, we hypothesized that Rosi regulates mitophagy and switches substrate metabolism, thereby promoting the proliferation of NSCs and accelerating the repair of SCI. We first demonstrated the effects of TZDs on NSC proliferation under SCI and the role of mitophagy in that process. Subsequently, we explored the detailed mechanism by which Rosi regulates mitophagy.

2. Materials and Methods

2.1. Animal Treatments and Cell Cultures. All of the animal experiments complied with the ARRIVE guidelines. They were conducted in accordance with the National Institutes of Health Guide for the Care and Use of Laboratory Animals (NIH Publication No. 8023, revised 1978). SCI was induced in animals as per previous reports. Briefly, 12-week-old male Sprague–Dawley (SD) rats were housed at room temperature in a 12-hour light/dark cycle, and they were allowed access to chow diet and water *ad libitum*. The rats were anesthetized and dropped using an impactor (weight: 10 g; diameter: 2.5 mm) from a height of 25 mm to induce SCI. Afterward, T_9 to T_{10} laminectomy was performed. SCI rats were randomly assigned to the Rosi- and the DMSO-treated groups, which then intragastrically received Rosi (3 mg/kg/day, GSK, Middlesex, United Kingdom) or the same volume of saline, respectively. Rosi was dissolved in DMSO as stock solution, which was diluted with saline for experiments. After 8 weeks of treatment, motor function recovery from SCI was assessed using the Basso–Beattie–Bresnahan locomotor rating scale (BBB scale). The rats were killed, and then, the injured spinal cords (centered on the lesion point) from SCI model rats were harvested for subsequent assays. Especially, before the spinal cord was harvested for flow cytometry, 5-bromo-2′-deoxyuridine (BrdU, 50 mg/kg/day) was intraperitoneally delivered into rats one time for seven consecutive days.

NSCs were cultured as described in our previous report [12]. Briefly, NSCs were obtained from the spinal cord of newborn SD rats (within 24 hours). Dissociated cells were suspended in DMEM/F12 medium (high glucose, Thermo Fisher Scientific, Massachusetts, USA) supplemented with 10% fetal bovine serum (Thermo Fisher Scientific, Massachusetts, USA), 2% B27 (Thermo Fisher Scientific, Massachusetts, USA), 20 μg/L epidermal growth factor (Sigma, Missouri, USA), 20 μg/L base fibroblast growth factor (Sigma, Missouri, USA), 50 μmol/L 2-mercaptoethanol (Sigma, Missouri, USA), 0.5 mmol/L L-glutamine (Thermo Fisher Scientific, Massachusetts, USA), and 1% streptomycin and penicillin (Thermo Fisher Scientific, Massachusetts, USA). NSCs were seeded 12 hours before treatments. Rosi (Cayman Chemical, Michigan, USA) was used at the indicated concentration.

To avoid the influence of other cells in spinal cord, NSCs in saline or Rosi-treated rats were isolated by antinestin magnetic beads. The dissociation solution consisted of 150 U/mL collagenase type 1, 1 mg/mL trypsin, and 15 U/mL DNaseI in the Krebs-Henseleit buffer. The isolated cells were resuspended in 1 : 100 antinestin beads and incubated for 15 min at 4°C. After washing nestin antibody-bound cells by adding equilibration buffer, the cells were resuspended in 100 μL of DMEM/F12 medium containing magnetic bead–conjugated goat anti-rabbit beads and were incubated for 15 min at 4°C. Subsequently, 2 mL of culture medium was added to the tube that was placed in the magnetic separator. The supernatant containing cells that had not bound magnetic beads was collected, and 2 mL culture medium was added to the tube. The magnet was then removed, and the cells that had bound magnetic beads were collected. Magnetically separated nestin postive fibroblasts can be used for PCR, western blot, and other downstream applications.

For the detection of PTEN induced putative kinase 1 (PINK1) and forkhead box protein O1 (FOXO1), NSCs were treated with Rosi for 48 hours. For the dual-luciferase reporter gene assay and chromatin immunoprecipitation (CHIP), Rosi was administered after 18 hours of induction of FOXO1 using doxycycline (DOX) dissolved in

phosphate-buffered saline (PBS). Afterward, NSCs were cultured and incubated in tetracycline-free serum in the presence of Rosi or the DMSO control for 24 hours. Carbonyl cyanide 3-chlorophenylhydrazone (CCCP, Sigma, Missouri, USA) and actinomycin D (ActD, 1 μg/mL, Sigma, Missouri, USA) were used at the indicated concentrations and time points.

2.2. Plasmid Construction and Lentivirus Packaging. Lentivirus plasmids expressing mitoTimer, FOXO1, and PINK1 were constructed. The mitoTimer and PINK1 were gifts from Roberta Gottlieb (Addgene plasmid, 50547) and Mark Cookson (Addgene plasmid, 13323), respectively. FOXO1 was synthesized *in vitro*. To avoid the disadvantages caused by a consecutive expression, the coding sequence for each of the three genes was cloned into the tetracycline-induced expression backbone vector (pLVX-TetOne-Puro, Clontech, Otsu, Japan) using incision enzymes *Eco*R I/*Bam*H I (mitoTimer), *Age* I/*Eco*R I (PINK1), and *Bam*H I/*Bst*Z1107 I (FOXO1). The constructed vectors were confirmed by DNA sequencing.

For lentivirus packaging, packaging vectors (psPAX2 and pMD2.G) and expression vectors (pLVX-TetOne-Puro-mitoTimer/FOXO1/PINK1) were cotransfected into 293T cells using FuGene transfection reagents. Titers of the pseudovirus were determined by PCR, and a known titer of the lentivirus was used as the control. Primers targeting the long terminal repeat were used in PCR. A multiplicity of infection (MOI) of 30 was used in all of the experiments. The indicated concentration of DOX was used to induce expression.

2.3. CCK-8 Measurement, ATP Production, Edu Staining, Cell Counting, and Glucose and Lactic Acid Assays. The proliferation of NSCs was assessed by the Cell Counting Kit-8 (CCK-8, Dojindo Molecular Technologies, Kumamoto, Japan), adenosine triphosphate (ATP) production (Biovision Inc., California, USA), 5-ethynyl-2′-deoxyuridine (Edu) (Ribobio, Guangzhou, China) incorporation, and cell counting. After treated with DMSO or Rosi for 18 hours, 24 hours, and 36 hours, proliferation of NSCs was assessed by CCK-8, ATP production, and Edu incorporation, respectively. CCK-8 and ATP production were measured according to the instructions of the manufacturers. Edu is a thymidine analogue, which can replace thymine to infiltrate the replicating DNA molecules during cell proliferation. The Edu-binding fluorescent dye accurately reflects cell proliferation. The cells were collected and washed with PBS three times for subsequent Edu and nuclear staining according to the manufacturer's instructions. Cells were collected and resuspended for counting using Countstar (ALIT Life Science Co. Limited, Shanghai, China).

For intracellular glucose assessment, cells were treated with DMSO or Rosi for 12 hours in DMEM medium. Afterward, cells were ultrasonically fragmented in glucose-free PBS and centrifuged. Glucose levels in the supernatants were determined using a commercially available kit (Biovision Inc., California, USA). Total protein levels in the precipitation were determined and used for normalization. For the lactic acid assay, cells were subjected to the same treatments for 24 hours, and both the supernatants and cells were collected. Lactic contents in the supernatant were determined using a biochemical analyzer. Cells were counted, and lactic acid concentration per cell was calculated.

2.4. Biochemical Detections. Cells were treated in the complete medium as indicated, and they were subjected to total or mitochondrial protein extraction using the respective kits. Protein concentration was determined by the Bradford protein assay. Extracted proteins were then resolved on SDS-PAGE, and they were transferred to a polyvinylidene fluoride membrane. Blots were incubated with the antibodies for FOXO1 (Cell Signaling Technology, Massachusetts, USA), PINK1 (Abcam, Massachusetts, USA), β-actin (Cell Signaling Technology, Massachusetts, USA), Complex I (NDUFB8, Cell Signaling Technology, Massachusetts, USA), Complex IV (mt-CO1, Cell Signaling Technology, Massachusetts, USA), FUNDC1 (Abcam, Massachusetts, USA), Bnip3 (Abcam, Massachusetts, USA), and Nix (Cell Signaling Technology, Massachusetts, USA) or voltage-dependent anion-selective channel 1 (VDAC1, Cell Signaling Technology, Massachusetts, USA) at 4°C overnight. Afterward, bound antibodies were visualized using peroxidase-coupled secondary antibodies and ECL reagents (Thermo Fisher Scientific, Massachusetts, USA). The bands of interest were quantified using the Image J densitometry scanning program. For Western blots of complexes I and IV and VDAC1, total mitochondrial proteins were isolated using the commercially available kit (Qiagen, Duesseldorf, German). β-Actin and VDAC1 were used as the loading control for total proteins and mitochondrial proteins, respectively.

The productions of IL-1β (BMS630, Invitrogen) and IL-6 (BMS625, Invitrogen) in the primary NSCs from SCI rats were measured by enzyme-linked immunosorbent assay (ELISA) according to the manufacturer's instructions.

2.5. Real-Time RT-PCR Assays. NSCs were grown in 6-well plates. Total RNA was isolated using TRIZOL reagent (Takara, Tokyo, Japan). The integrity and purity of total RNA were electrophoretically and spectroscopically confirmed. Reverse transcription of 800 ng of total RNA was performed with a commercially available kit (Takara, Tokyo, Japan) using hexamer primers. Detailed procedures were performed according to the manufacturer's protocol. Real-time PCR was performed on a LightCycler® 96 System (Roche, Basel, Switzerland) with SYBR® Premix Ex Taq™ II (Takara, Tokyo, Japan). Instead of the first-strand cDNA, water was used as the negative control, and primers using plasmid-containing genes of interest were used as positive controls. β-Actin mRNA levels were used to normalize each sample and gene. All of the primers used in real-time RT-PCR are listed in Table S1–3.

2.6. Mitophagy and Oxygen Consumption Detection. Mitophagy was assessed by colocalization of LC3B and the mitochondrial marker (Tomm20) stained by immunofluorescence. Cells were grown on a glass slide in 6-well plates

with the indicated treatments. For immunofluorescence, cells were washed and fixed in 4% paraformaldehyde. Cell membranes were permeabilized with 1% Triton. LC3B (Abcam, Massachusetts, USA) and Tomm20 (Abcam, Massachusetts, USA) antibodies were incubated for 12 hours. Alexa 488-labeled rabbit IgG antibody and Dylight 549-labeled mouse IgG antibody were incubated. Finally, cell nuclei were restained with DAPI and examined by confocal imaging (LSM70, Carl Zeiss, Oberkochen, Germany).

The mitoTimer is modified from a fluorescent timer, in which fluorescence shifts over time from green to red as the protein matures. It is a tool for monitoring mitochondrial turnover [24]. Enhanced mitophagy accelerates mitochondrial clearance, which results in the reduction of red fluorescence. Besides, mitoTimer can only be imported to the healthy mitochondria. Therefore, enhancement of green fluorescence indicated an increase in healthy mitochondrial biogenesis. Doxycycline (3 μg/mL, MP Biomedicals, Ohio, USA) was used to induced mitoTimer expression 24 hours before treatments, and the results were observed under confocal fluorescence microscopy.

For the oxygen consumption test, cells were treated with DMSO or Rosi for 48 hours, and the medium was removed. According to the manufacturer's instructions, oxygen consumption was detected using a commercially available kit (Abcam, Massachusetts, USA). Succine and adenosine diphosphate (ADP) were used to induce the state 2 and state 3 respiration, respectively.

2.7. Flow Cytometry. The proportion of Nestin- and BrdU-positive ($Nestin^+/BrdU^+$) cells in the spinal cord of SCI rats was measured by flow cytometry. Rats were anesthetized, and the spinal cords were removed, which were then subjected to trypsin and collagenase for digestion of the matrix, and single-cell suspensions were prepared. Cells were incubated with the primary antibodies against Nestin (Abcam, Massachusetts, USA) and BrdU (Abcam, Massachusetts, USA), followed by a FITC- or Cy3-labeled secondary antibody. Subsequently, cells were washed and resuspended in PBS, and they were subjected to flow cytometry analysis. Auto-fluorescence and isotype controls were used routinely as controls.

Mitochondria were stained with mitoTracker Green (Thermo Fisher Scientific, Massachusetts, USA), together with mitoTracker Red (Thermo Fisher Scientific, Massachusetts, USA) or mitoSOX (Thermo Fisher Scientific, Massachusetts, USA). mitoTracker Green stains all of the mitochondria independent of the membrane potential, while mitoTracker Red accumulation in the mitochondria relies on the normal membrane potential. mitoSOX serves as a mitochondrial reactive oxygen species (ROS) probe. NSCs were incubated with mitoTracker Green/Red or mitoTracker Green/mitoSOX (concentrations of all agents were 100 nmol/L) for 15 min, followed by washing twice with PBS to remove the unbound dyes. Cells were collected and resuspended in PBS. Finally, cells were subjected to flow cytometry analysis. All flow cytometry data were analyzed using the FlowJo software X (Oregon, USA). The unstained cells were used to set the gates in the FlowJo program.

2.8. Bioinformatic Analysis, Dual-Luciferase Reporter Gene Assay, Site-Directed Mutagenesis, and Chromatin Immunoprecipitation (CHIP). Bioinformatic analysis, dual-luciferase reporter gene assay, site-directed mutagenesis, and chromatin immunoprecipitation were used to identify the FOXO1 binding sites in the PINK1 gene. Except for the gene promoter miner (GPMiner), which was performed according to another study [25], all other assays and analyses were performed as per our previous report [26].

Promoter region sequences were determined to search the potential transcription factor-binding sites. Putative core regulatory elements (e.g., GC boxes, INR, CAAT boxes, or TATA boxes) were bioinformatically analyzed by the Genomatix MatInspector [26] (Transcription factor binding sites, weight matrices; Matrix Library Version 9.4; Core similarity of 0.75 and Matrix similarity of "Optimized") and GPMiner [25], respectively. The predictive sequence that regulates PINK1 transcription was validated by the dual-luciferase reporter gene assay. Segments with the indicated region in the *PINK1* gene were cloned into pGL3-Basic vectors. To better demonstrate that Rosi repressed PINK1 transcription through FOXO1, we used DOX (1 μg/mL) to induce FOXO1 expression in NSCs. NSCs were electroporated (1×10^4 cells; voltage: 250 V; capacitor: 600 μF; plasmid: 1 μg, respectively, for each) to import pGL3 and pRL-TK and seeded in 96-well plates. Cells were cultured for 24 hours after electroporation. Detection procedures were performed according to the manufacturer's protocol. Luciferase activities were normalized to the cotransfected pRL-TK plasmid.

Site-directed mutagenesis was performed using the commercially available QuikChange®-II kit (Agilent Technologies, California, USA). Briefly, PCR was performed to obtain the amplicon containing the desired nucleotide mutations using the nonmutated plasmid as the template. PCR products were purified and subjected to *Dpn* I digestion to erase the unmutated plasmid, and the cells were then transformed into competent cells. The mutated plasmid was sequenced confirmed. All of the primers used are listed in Supplementary materials.

CHIP was performed using the Pierce Agarose CHIP Kit (Thermo Fisher Scientific, Massachusetts, USA) as per our previous report [26]. Cells were plated in a 10 cm dish with the indicated treatments. The medium was removed, and the cells were washed with precooled PBS. Cells were cross-linked in 1% formaldehyde and resuspended, followed by sequential lysis of the cells and nuclear membrane. After lysis, sonication (8 seconds with a 10-second intermission for six times) was performed to generate sheared DNA fragments. Supernatants were collected and subjected to agarose protein A/G to remove the nonspecific bound DNA. Agarose was removed, and supernatants, whose 10% volume was collected for the input, were collected for chromatin immunoprecipitation with the FOXO1 antibody overnight at 4°C followed by the new agarose protein A/G. The supernatants were removed, and agarose was collected for elution and reverse-cross linking to recover the bound DNA. Finally, the recovered DNA was purified and used as the template for PCR detection using primers flanking the

FOXO1 binding sites in the first intron of the *PINK1* gene. Primers' sequences are listed in Supplementary Tables.

2.9. Statistical Analysis. Data are expressed as the mean ± SEM. Statistical significance among groups was determined by using the *t*-test (the unpaired *t*-test was used for the independent groups, while the paired *t*-test was used for assessing the preoperation and postoperation JOA scores in the clinical data) or one-way ANOVA followed by the SNK test for multiple comparisons if three or more groups were involved. The Chi-square test was used to test for equality of proportions between populations. Logistic regression was used to measure the influence of the independent variables (age, gender, HbA1c, and Rosi/no-Rosi treatment) on the dependent variable (mean difference in the JOA score between the preoperation and postoperation categories was as follows: H-JOAIR, mean difference in JOA > 2; otherwise, L-JOAIR). Visualized results (nomogram) were obtained. A nomogram was produced by R-statistics version 3.5.0 with the RMS package [27], and the remaining statistical graphs were created by the GraphPad Prism Software (California, USA).

3. Results

3.1. Rosi Ameliorates Spinal Cord Injury, Inhibits Inflammation Factors, and Promotes Glucose Utilization for ATP Production in the Proliferation of NSCs. To assess the effects of Rosi treatment on the recovery of spinal cord function after SCI, we compared the BBB scores between the saline- and Rosi-treated rats. The score was dramatically higher in rats treated with Rosi (Figure 1(a)), indicating that Rosi accelerated SCI recovery. To investigate the change of inflammation of primary NSCs from SCI rats in response to Rosi treatment, the expression levels of inflammatory cytokines were examined by ELISA. The expression levels of IL-1β and IL-6 in the Rosi group were significantly lower than those in the control group (Figure 1(b)).

Given that proliferation of NSCs is crucial for the recovery of SCI, we examined the proliferation of NSCs in the spinal cord of SCI rats treated with saline or Rosi by flow cytometry. Primary NSCs were isolated from rats receiving saline or Rosi treatment, and proportions of Nestin positive ($Nestin^+$) and/or BrdU positive ($BrdU^+$) cells were determined. Nestin is a characteristic marker of NSCs. BrdU is a thymine derivative, which can stably integrate into the replicating DNA instead of thymine (T). Thus, a BrdU-specific antibody can detect cell proliferation. The proportion of Nestin positive cells (including $Nestin^+/BrdU^-$ and $Nestin^+/BrdU^+$, 53.68 ± 4.19%) in Rosi-treated rats was increased by 15.86% in comparison with the saline-treated group (46.33 ± 5.67%). Nestin and BrdU double-positive ($Nestin^+/BrdU^+$) cells in Rosi-treated group were increased by 0.54-fold compared to the control group (30.04 ± 5.17% vs. 19.46 ± 4.03%; $P < 0.01$) (Figures 1(c) and 1(d)). These data indicated that Rosi not only increased the number of NSCs but that it also promoted the proliferation of NSCs. To further confirm the increased proliferation of NSCs upon Rosi administration, we investigated the effects of Rosi on NSCs *in vitro* by CCK-8, cell counting, and Edu staining. The Rosi administration tended to increase the NSCs viability in a dose-dependent manner, as shown by CCK-8. The 20 μg/mL group, particularly the 30 μg/mL and 50 μg/mL groups, showed a significant increase in NSC viability compared with the control group (Figure 1(e)). The results from cell counting showed that Rosi treatment resulted in a 1.5-fold increase in NSCs on day 7; moreover, it shortened the doubling time to approximately 48 hours, which was even shorter (within 24 hours) at higher concentrations of Rosi treatment (Figure 1(f)). Given that DNA replication is necessary for cell proliferation, we finally assessed cell proliferation by Edu staining assay. The proportion of Edu positive-NSCs significantly increased after Rosi treatment (Figures 1(g) and 1(h)).

Considering that ATP is essential for cell proliferation, we explored changes of its production in response to Rosi. As shown in Figure 1(i), compared with the control group, ATP production upon Rosi administration increased slightly in 20 μg/mL or 30 μg/mL groups and notably (1.69-fold) at 50 μg/mL group. Glucose and fatty acids are the leading resources for ATP production, mainly via oxidative phosphorylation (OXPHOS) in mitochondria. The oxygen consumption assays showed that Rosi did not significantly affect OXPHOS (Figure S1A–E). Therefore, we further determined whether the ATP production enhanced by Rosi came from glycolysis. In the presence of oligomycin, an ATP synthase inhibitor during OXPHOS process, ATP production in Rosi-treated cells was much higher than that in the control group (Figure 1(j)). Notably, the amount of ATP production (approximately 230 nmol/L) in response to Rosi at 50 μg/mL was higher than that in the control group regardless of oligomycin intervention (Figures 1(i) and 1(j)), indicating that the Rosi-induced increase in ATP production was mainly the result of glycolysis. Rosi at 30 μg/mL and 50 μg/mL significantly increased glucose uptake by NSCs (Figure 1(k)) but did not obviously alter the supernatant lactate content (Figure S2).

3.2. Rosi Promotes Proliferation of NSCs via Inhibition of PINK1-Mediated Mitophagy. Mitophagy has been shown to play an essential role in both cell proliferation and substrate metabolism. Therefore, we explored whether mitophagy is implicated in the proliferation of NSCs induced by Rosi. After treatment with Rosi or DMSO, NSCs were observed with laser confocal microscopy for immunofluorescence colocalization of autophagy marker LC3B and mitochondrial marker Tomm20. Rosi decreased the punctuated distribution of LC3B in the cytoplasm, which colocalized with Tomm20, indicating inhibition of mitophagy (Figure 2(a)). The mitochondria quality and state can be monitored by an indicator protein mitoTimer protein located in the mitochondrial membrane [24]. The low red/green ratio of mitoTimer indicates that mitochondria are younger and healthier. In contrast, the increase in red/green ratio indicates the aging of mitochondria, suggesting that mitophagy responsible for clearing aged mitochondria is blocked. Compared with the DMSO-treated control group, the mitophagy inducer CCCP markedly reduced the red/green ratio, which

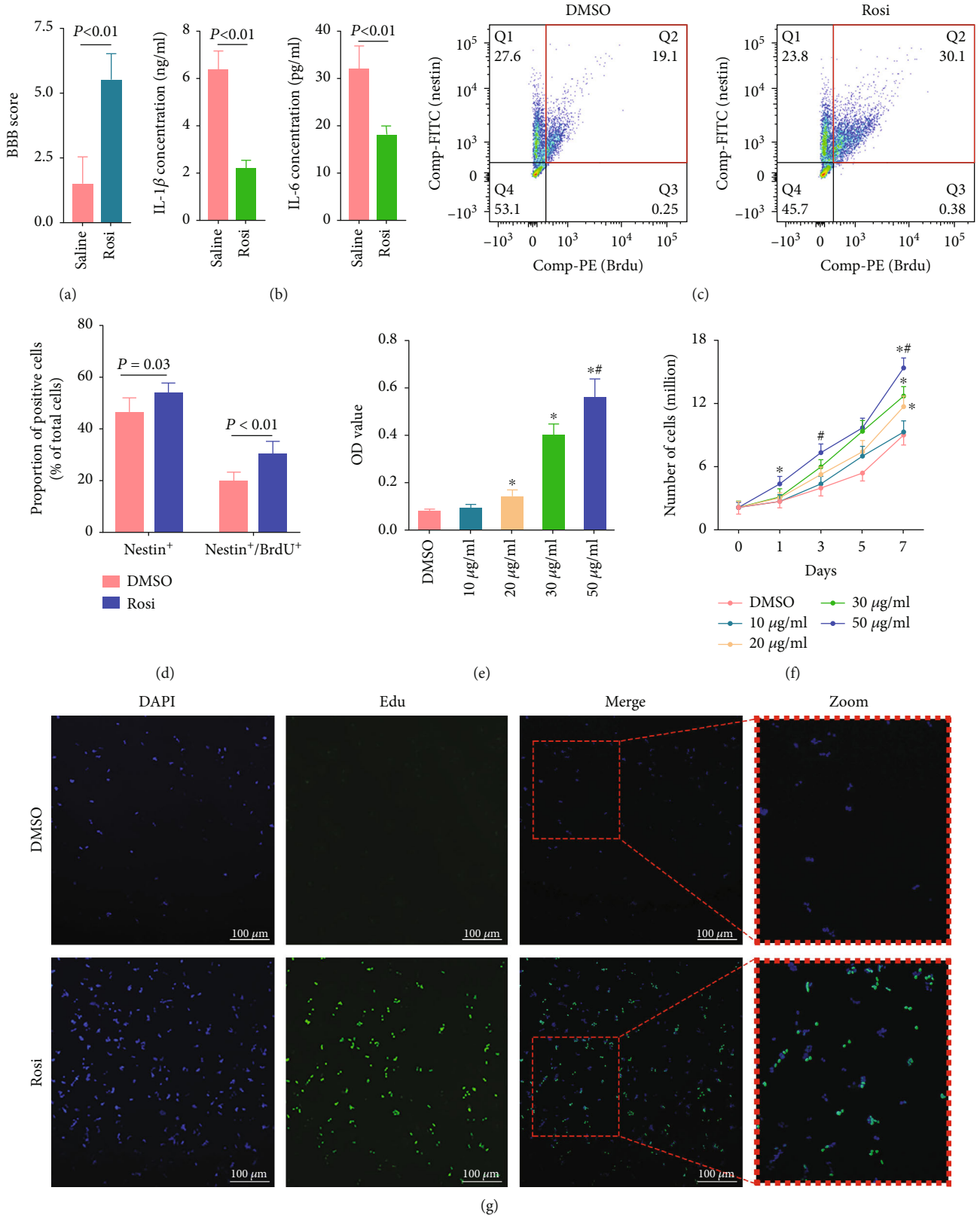

Figure 1: Continued.

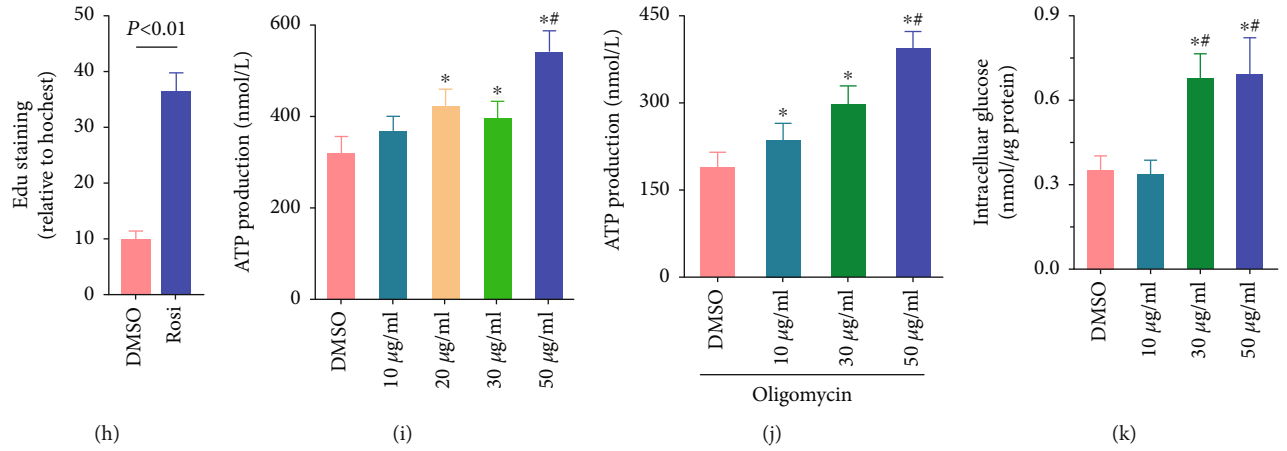

Figure 1: Rosi ameliorates spinal cord injury, inhibits inflammation factors, and promotes NSC proliferation. (a) BBB scores in SCI rats with or without Rosi treatment. (b) The levels of IL-1β and IL-6 in NSCs by ELISA kit. (c) Representative plots of flow cytometry. The Nestin$^+$/BrdU$^+$ cells in the red rectangle are those of interest. (d) Flow cytometry results showing Nestin$^+$ cells and Nestin$^+$/BrdU$^+$ cells in the spinal cord of SCI rats undergoing DMSO or Rosi treatments. (e, f) CCK-8 measurement and cells counting in NSCs treated with DMSO or different concentrations of Rosi. $^{\#}P < 0.05$ versus 30 μg/mL Rosi. (g, h) Images of Edu staining in NSCs treated by DMSO or Rosi. DAPI (blue) and Edu (green) represent the nucleus and the newly synthesized DNA, respectively. (i) Effects of Rosi on ATP production. $^{\#}P < 0.05$ versus 30 μg/mL Rosi. (j) Effects of Rosi on ATP levels produced by glycolysis. $^{\#}P < 0.05$ versus 30 μg/mL Rosi. (k) Effects of different Rosi concentrations on intracellular glucose content. $^{\#}P < 0.05$ versus 20 μg/mL Rosi. Data represent six (a) or three (b, c, e–g, i–k) independent experiments and are expressed as mean ± SEM (a–c, e–g, i–k). $^{*}P < 0.05$ versus DMSO treatment.

was in accordance with the clearance of mitochondria by CCCP. Nevertheless, the Rosi-treated cells showed an obvious increase in red/green ratio, indicating the delayed clearance of mitochondria (Figure 2(b)). Interestingly, green fluorescence was also increased under Rosi treatment, indicating enhanced mitochondrial biogenesis (Figure 2(b)).

There are three canonical pathways inducing mitophagy, namely, PINK1/Parkin, Bnip3L/Nix (including Bnip3), and Fundc1. However, levels of Bnip3, Nix, and Fundc1 were not significantly different between DMSO- and Rosi-treated NSCs (Figure S3). In contrast, Western blot results showed that the expressions of mitochondrial PINK1 were decreased in Rosi-treated NSCs (Figure 2(c)). Results from PCR also yielded consistent results (Figure 2(d)). Similarly, PINK1 levels in the NSCs from the injured spinal cords were decreased in rats receiving Rosi (Figures 2(e) and 2(f)).

To study the effects of the depressed PINK1 and subsequent mitophagy impairment in Rosi-induced NSC proliferation, we performed rescued experiments. To avoid the excessive burden of mitochondria caused by consecutive expression of PINK1, we adopted a tetracycline-induced expression system to control the forced expression of PINK1 in NSCs. After the inhibition of mitophagy under Rosi administration was relieved by either the forced expression of PINK1 or the mitophagy inducer CCCP, proliferation of NSCs was assessed. The levels of PINK1 inhibited by Rosi (50 μg/mL) were restored only in the presence of DOX. CCK-8 and cell counting assays showed that forced PINK1 expression and CCCP administration decelerated the proliferation of NSCs (Figures 2(g) and 2(h)).

We next investigated the association between decreased PINK1 and inhibited mitophagy under Rosi treatment. The forced expression of PINK1 in NSCs by DOX enhanced the puncta of LC3B and the colocalization between LC3B and mitochondrial marker Tomm20 (Figure 3(a)), demonstrating the restoration of mitophagy inhibited by Rosi. In mitoTimer-expressing NSCs under Rosi treatment, compared with the vehicle control cells, the forced expression of PINK1 by DOX resulted in significantly reduced red fluorescence and slightly reduced green fluorescence, thereby verifying that the forced expression of PINK1 conspicuously reversed the suppressed mitophagy in the presence of Rosi (Figure 3(b)). Because PINK1 expression was induced up to the levels similar to those in steady-state NSCs without treatment, these results (Figures 3(a) and 3(b)) imply that excessive mitophagy may exist in NSCs. To further clarify this implication, NSCs were treated with Rosi or DMSO, and mitochondria were stained with mitoTracker Green plus mitoTracker Red or mitoSOX, which indicated healthy mitochondria and mitochondrial reactive oxygen species (ROS) contents, respectively. Flow cytometry showed that both the impaired mitochondria (mitoTracker Green$^+$/mitoTracker Red$^-$) and mitochondrial ROS (mitoTracker Green$^+$/mitoSOX$^+$) were similar between Rosi- and DMSO-treated cells (Figures 3(c) and 3(d)).

Taken together, all of the above data showed that Rosi promoted proliferation of NSCs, at least in part, via mitophagy inhibition, which was mediated by a reduction in mitochondrial PINK1. Besides, excessive mitophagy could exist in NSCs.

3.3. Rosi Inhibits PINK1 Expression through FOXO1 Downregulation. The above data demonstrated that PINK1 and mitophagy played essential roles in the Rosi-induced proliferation of NSCs, and we next elucidated the underlying mechanism regulating PINK1 expression. We first used ActD, a transcription inhibitor, to prevent RNA polymerase elongation for assessing the mRNA stability to determine

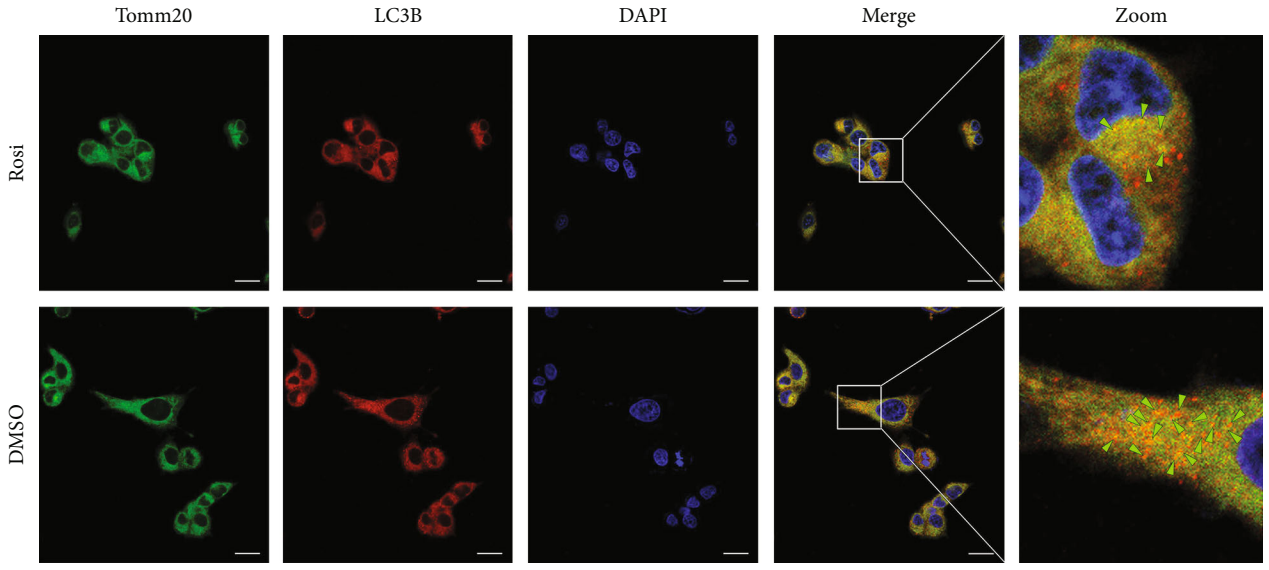

(a)

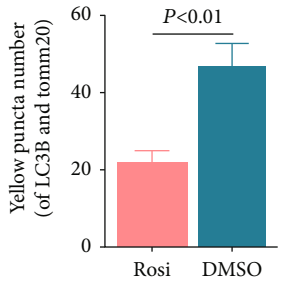

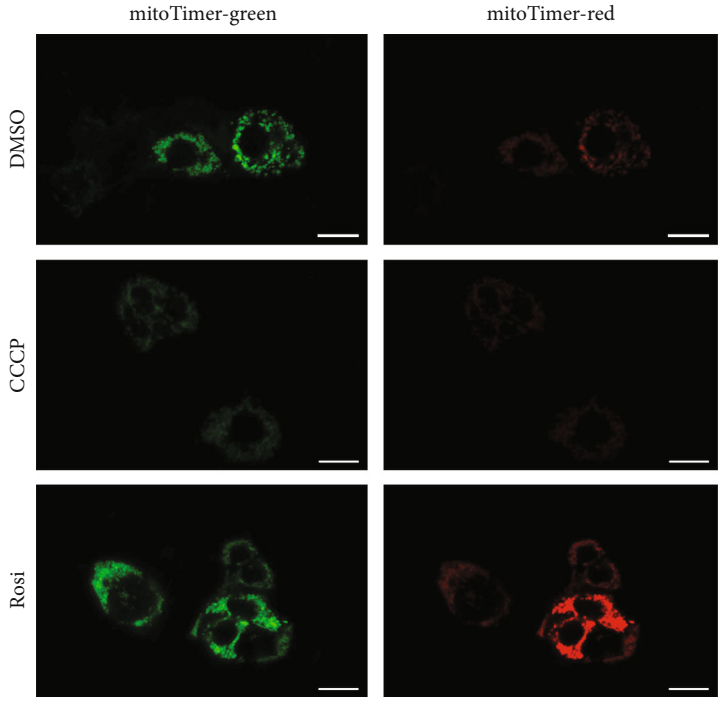

(b)

Figure 2: Continued.

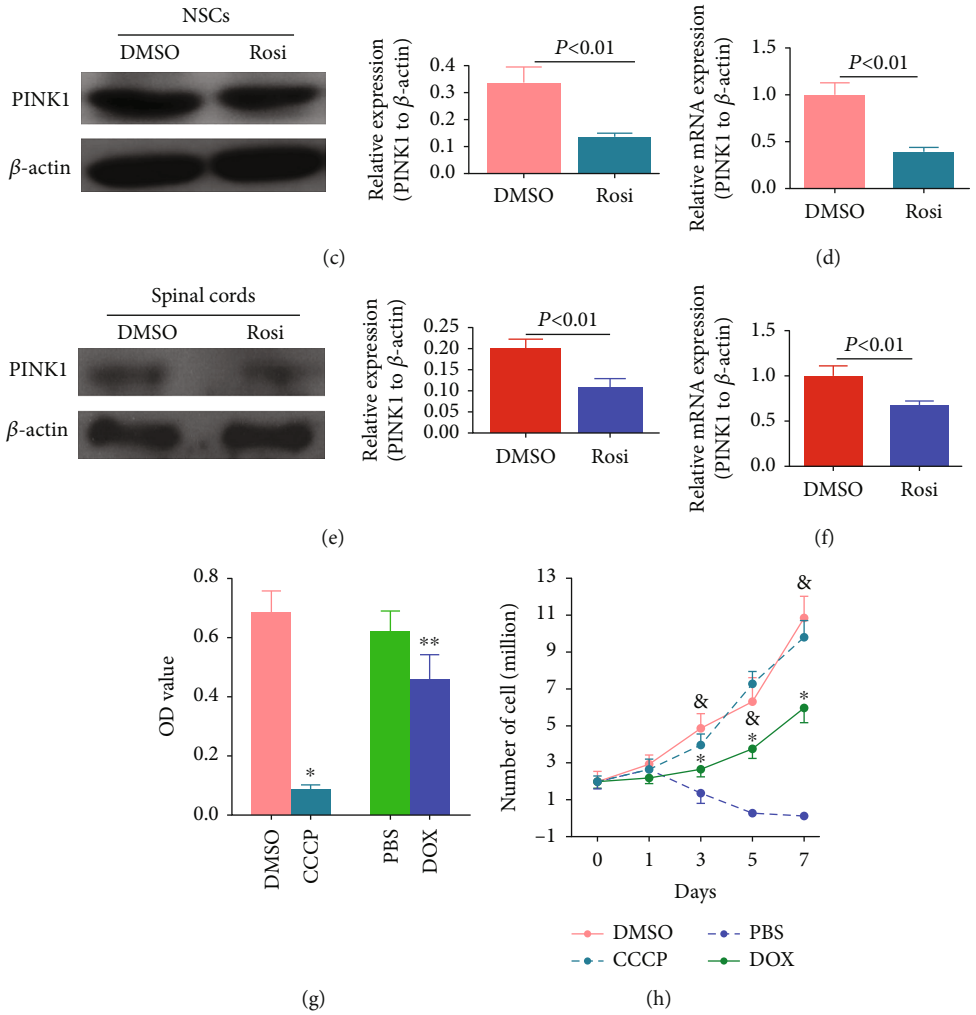

Figure 2: The roles of mitophagy played in Rosi-induced NSC proliferation. (a) Confocal immunofluorescence images showing LC3B (red) and Tomm20 (green) costaining in NSCs. The statistical analyses were performed base on four randomly selected scopes under the confocal microscope. Scale bar represents 10 μm. (b) Confocal fluorescence images showing the fluorescence of mitoTimer. Green fluorescence represents younger and healthier mitochondria (usually less than 48 hours), while red fluorescence represents mitochondria existing for a longer time (usually longer than 48 hours). Scale bar represents 10 μm. (c) Western blot images showing the effects of Rosi on PINK1 expression in Rosi-treated NSCs. (d) PCR results showing the effects of Rosi on PINK1 expression in Rosi-treated NSCs. (e) Western blot images showing the effects of Rosi on PINK1 expression in the NSCs from the injured spinal cords. (f) PCR results showing the effects of Rosi on PINK1 expression in the NSCs from the injured spinal cords. (g, h) CCK-8 measurement (g) and cell counting (h) showing effects of restored mitophagy by either CCCP administration or the forced PINK1 expression on Rosi-induced cell proliferation. Rosi was applied in all the groups in addition to the indicated treatments. Data represent three independent experiments and are expressed as mean ± SEM. $^{*}P < 0.05$ versus DMSO treatment; $^{**}P < 0.05$ versus PBS treatment.

whether the transcriptional or posttranscriptional mechanisms were involved. The degradation rates of PINK1 RNA showed a similar pattern between the Rosi-treated group and the DMSO control group (Figure 4(a)). As shown in Figure 4(b), the mRNA level of PINK1 in NSCs upon Rosi administration was decreased by three-quarters compared with that in the control group. After NSCs were pretreated with ActD and treated with Rosi or DMSO, the mRNA level of PINK1 in NSCs after Rosi administration decreased by about one-quarter in comparison with that after DMSO administration. These results indicated that the inhibition of transcription was the primary mechanism of Rosi-induced PINK1 suppression.

To account for the Rosi-induced PINK1 transcriptional reduction involved in mitophagy inhibition, we next identified the related transcription factors of PINK1. Rosi is a specific agonist of the nuclear receptor transcription factor PPAR-γ. A wide range of target genes of PPAR-γ were subjected to enrichment analysis of the KEGG signaling pathway, but none of them were directly associated with mitophagy. Rosi as a TZD antihyperglycemic agent mainly works by improving insulin action. Rosi can increase the uptake of glucose by NSCs (Figure 1(k)). Therefore, we focused on the genes involved in the insulin and glycolysis pathways as well as mitophagy, and we found eight candidate transcription factors. Except for STAT3, NF-κB, and

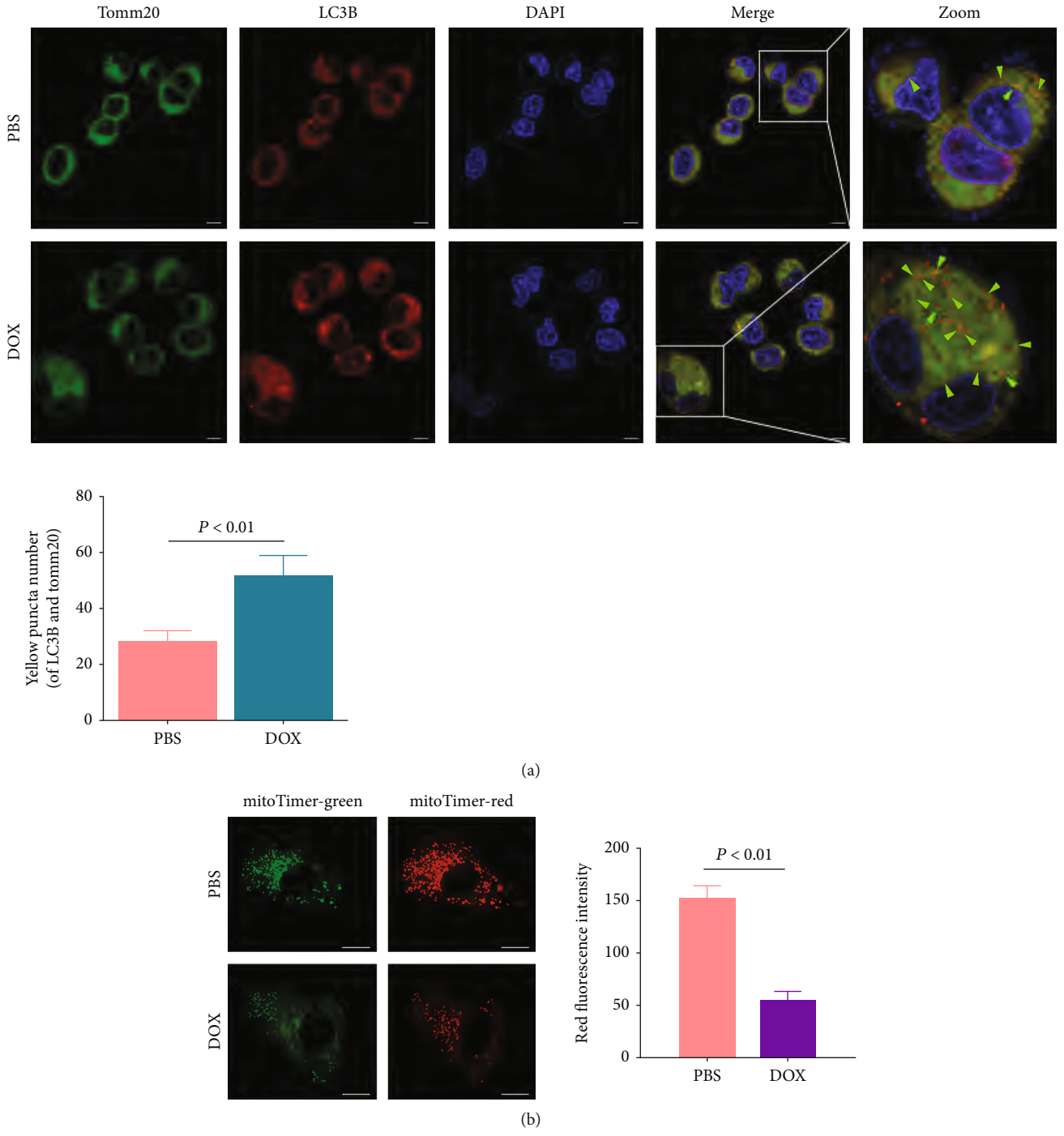

Figure 3: Continued.

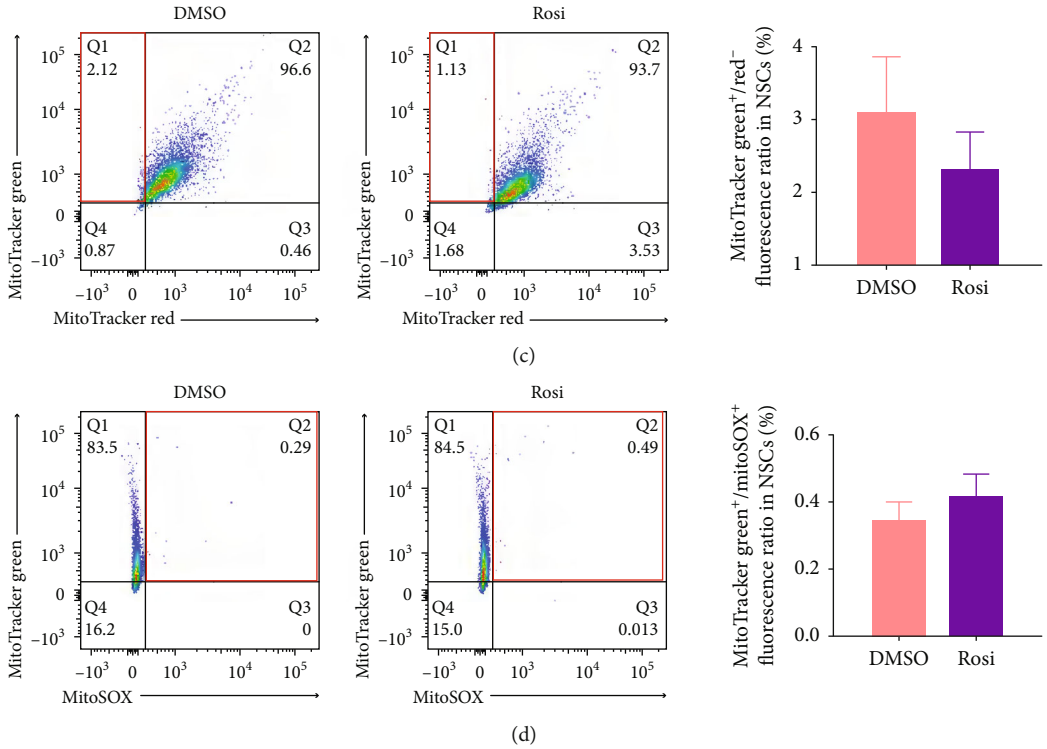

Figure 3: Overexpression of PINK1 counteracted relieved Rosi-induced suppression of mitophagy. (a, b) Confocal immunofluorescence images showing costaining of LC3B (red) and Tomm20 (green) (a) and mitoTimer (b) in NSCs, in which the forced PINK1 expression was induced by DOX or by the PBS as control and then subjected to Rosi. The forced PINK1 expression was controlled at the level similar to that without Rosi treatment. The statistical analyses were performed base on four randomly selected scopes under the confocal microscope. Scale bar represents 10 μm. (c, d) Flow cytometry results showing mitoTracker Green$^+$/mitoTracker Red$^+$ cells (c) and mitoTracker Green$^+$/mitoSOX$^+$ cells (d) with DMSO or Rosi treatments. The cells in the red rectangle are those of concern. Data represent three independent experiments.

CRTC2, the mRNA expression levels of other candidates were significantly altered by Rosi administration, among which FOXO1 mRNA was exclusively decreased (Figure 4(c)). A CREB or LXR antagonist did not abolish the effects of Rosi on PINK1 expression (Figure 4(d)). Due to the unavailability of the FOXO1 agonist, we used the tetracycline-induced system to restore FOXO1 expression. The forced FOXO1 expression reversed the decrease in PINK1 expression under Rosi (Figure 4(d)). Downregulation of FOXO1 proteins in NSCs was confirmed by western blotting (Figure 4(e)). Besides, the changes of FOXO1 levels could also be observed in the NSCs purified from Rosi-treated SCI rats (Figure 4(e)). The Rosi-induced reduction in PINK1 protein level was reversed by the forced FOXO1 expression (Figures 4(f)).

Next, we determined whether the forced FOXO1 expression can counteract the promotion of NSC proliferation by Rosi. The tetracycline-induced expression system was used for the forced expression of FOXO1, and DOX at 1 μL/mL resulted in a similar FOXO1 expression level as that in the DMSO control cells, which was used in the subsequent experiments. The forced FOXO1 expression by DOX was able to counteract the Rosi-induced increase of NSC proliferation, as demonstrated by CCK-8 measurement (Figure 5(a)), ATP production (Figure 5(b)), and Edu incorporation (Figures 5(c) and 5(d)). FOXO1 expression slightly increased state 3 mitochondrial respiration (Figure 5(e)) and greatly increased oxygen consumption in FA media (Figure 5(f)), indicating that FOXO1 increased the mitochondrial respiratory capacity and promoted OXPHOS. However, the main mitochondrial complexes I and IV were not significantly altered by the forced FOXO1 expression (Figure 5(g)). Under oligomycin treatment, there was a decrease in ATP production by glycolysis in FOXO1-expressing NSCs (Figure 5(h)). These results supported the claim that FOXO1 expression was decreased by Rosi and inhibited glycolysis, but it enhanced the mitochondrial oxidation capacity. As expected, the forced FOXO1 expression promoted mitophagy, as indicated by both immunofluorescence colabeled LC3B/Tomm20 and the mitoTimer indicator (Figure S4). This result was concordant with the finding that the respiratory capacity was increased. Still, no change in mitochondrial complex contents was observed since mitophagy is the main mechanism that ensures OXPHOS enzymatic activity.

Taken together, these data demonstrated that the effects of Rosi on the promotion of NSC proliferation and inhibition of PINK1 expression were mediated by the suppression of transcription factor FOXO1 expression rather than other transcription factors involved in TZDs-related pathways.

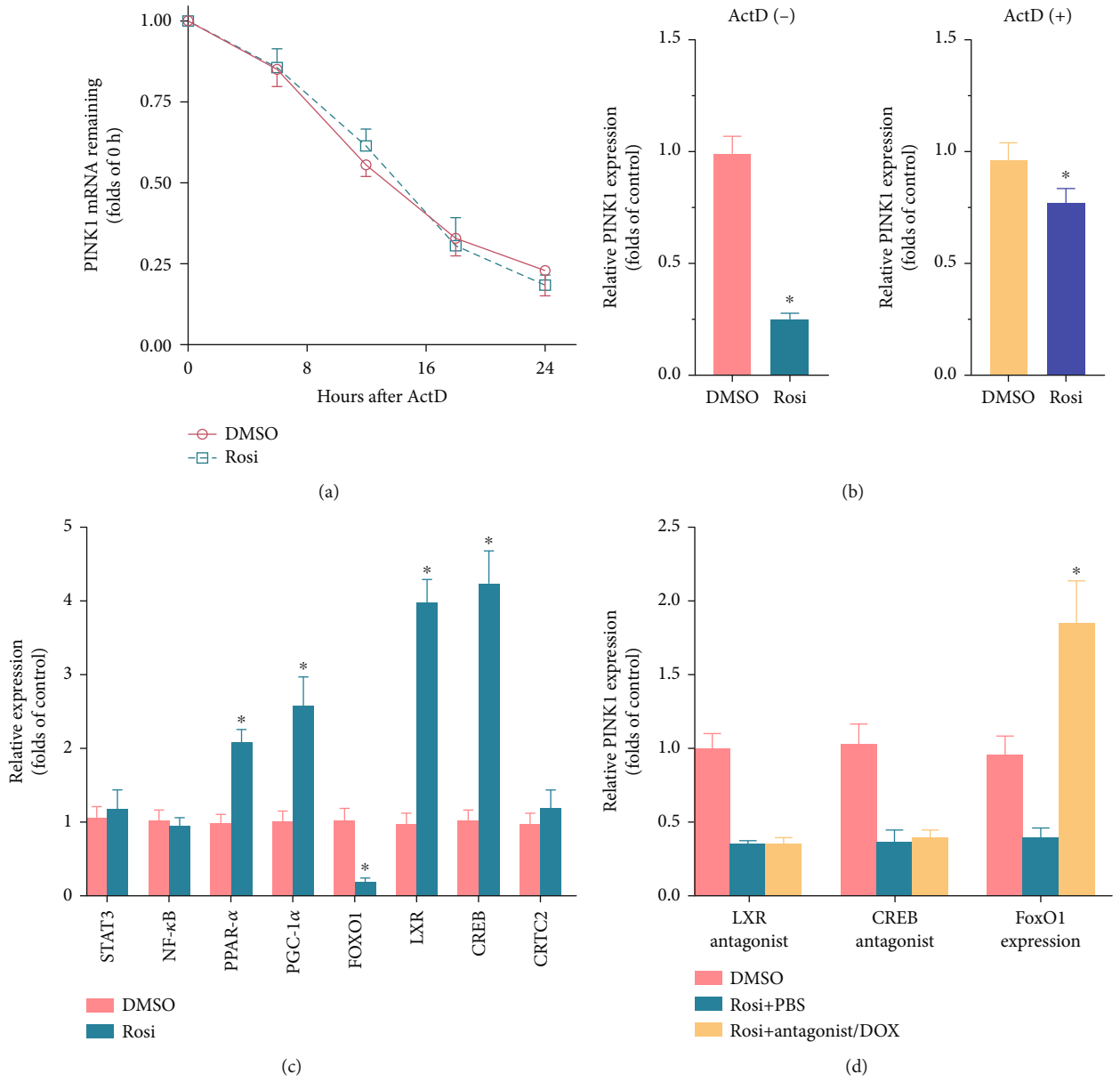

Figure 4: Continued.

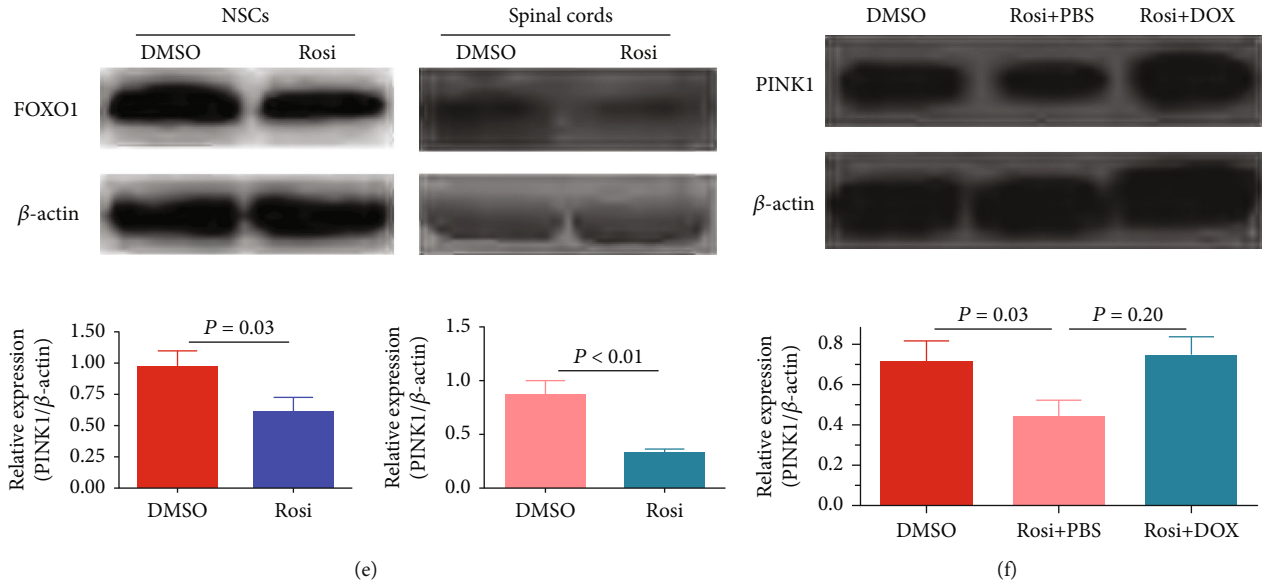

Figure 4: Identification of FOXO1 as a key transcription factor in Rosi-induced PINK1 suppression. (a) PINK1 mRNA stability test. DMSO or Rosi was administered to NSCs for 12 hours before ActD treatment. PINK1 mRNA was measured immediately, 8 hours, 16 hours, and 24 hours after ActD treatment. (b) Effects of ActD on PINK1 mRNA contents in cells treated by DMSO control or Rosi. The data of ActD(-) group (for both DMSO and Rosi) were normalized to PINK1 expression levels in the cells without any treatment. The data of ActD(+) group (for both DMSO and Rosi) were normalized to PINK1 expression levels in cells with ActD treatment. (c) Effects of Rosi on mRNA expression of the eight transcription factors identified to be involved in TZDs-related pathways by KEGG analysis. (d) Effects of antagonists/agonists against the mostly altered transcription factors by Rosi (LXR, CREB, and FOXO1) on PINK1 mRNA expression. (e) Western blot images showing the effects of Rosi on FOXO1 protein expression. (f) Effects of the forced FOXO1 expression on Rosi-induced PINK1 expression. β-Actin was used as an internal reference (a–f). The mRNA content was measured by RT-qPCR. Data represent three independent experiments and are expressed as mean ± SEM (a–d). $^{*}P < 0.05$ versus DMSO or PBS.

3.4. FOXO1 Directly Binds to the First Intron of PINK1 and Promotes Transcription. To unravel the underlying mechanism by which FOXO1 as a transcription factor regulates PINK1 expression, we studied the role of FOXO1 in the promoter activity of PINK1. The genomic location of the rat PINK1 gene promoter has not yet been identified. The rat PINK1 genomic sequences are located on chromosome 5, spanning 12113 bp (chr5: 156677146 to 156689258). Transcription starts from 156677146 nt, while translation starts from 156677182 nt. We adopted the −2300 bp (chr5: 156675183–156677182) counting from the translation start site, as described in the previous reports [26, 28]. Putative FOXO1 binding sites (FOXO1 consensus sequence (FCS)) inside this sequence were predicted by the GenomatixMatInspector. Unexpectedly, no FCSs were found in the sequences. We continued to explore the potential FCS in the first intron since the first intron is widely believed to regulate gene transcription, and it could be a part of the promoter. It spans a total of 4980 bp (chr5: 156677569–156682548), and three putative FCSs (FCS1, chr5: 156680169–156680185, +3022 bp; FCS2, chr5: 156681222–156681238, +4076 bp; FCS3, chr5: 156681244–156681260, +4098 bp; counting from the translation site) were identified.

We next validated the effects of these putative regulatory sequences on FOXO1-induced PINK1 expression using the dual-luciferase reporter gene assay. First, both the −2300 bp and the first intron sequences were ligated into the pGL3-Basic vector to evaluate all potential sequences' overall effects. To best mimic the finding that Rosi promotes PINK1 transcription via suppression of FOXO1, we used the inducible expression system and induced FOXO1 expression before Rosi administration to avoid the constitutive expression of FOXO1, which completely abolished the effects of Rosi. The FOXO1 expression was induced for 24 hours in the medium containing DOX (1 μg/mL). NSCs were transfected with luciferase activity reporter vectors and cultured in a tetracycline-free medium containing Rosi (50 μg/mL) for another 24 hours. The results of luciferase activity are summarized in Figure 6(a). The constructed sequences activated transcription, which was augmented by the forced FOXO1 expression. Rosi counteracted this effect in situations with and without the induced FOXO1 expression (Figure 6(a)). This result demonstrated the regulatory function of the whole sequence and directly showed negative regulation of the PINK1 promoter activity by Rosi.

To more precisely identify the sequence response to FOXO1, the whole sequence (−2300 bp counting from the translation start site to the end of the first intron, except exon1) was divided into three reporters (reporter 1: 2300 bp; reporter 2: 2460 bp; reporter 3: 2523 bp; Figure 6(b)), and we examined the effect of each reporter on the PINK1 transcriptional activity. FOXO1 expression was induced before Rosi administration, as stated above. As shown in Figure 6(b), reporter 3 responded to Rosi most obviously, resulting in a 5.39-fold decrease in luciferase activity. Reporters 1 and 2 also responded to Rosi, resulting

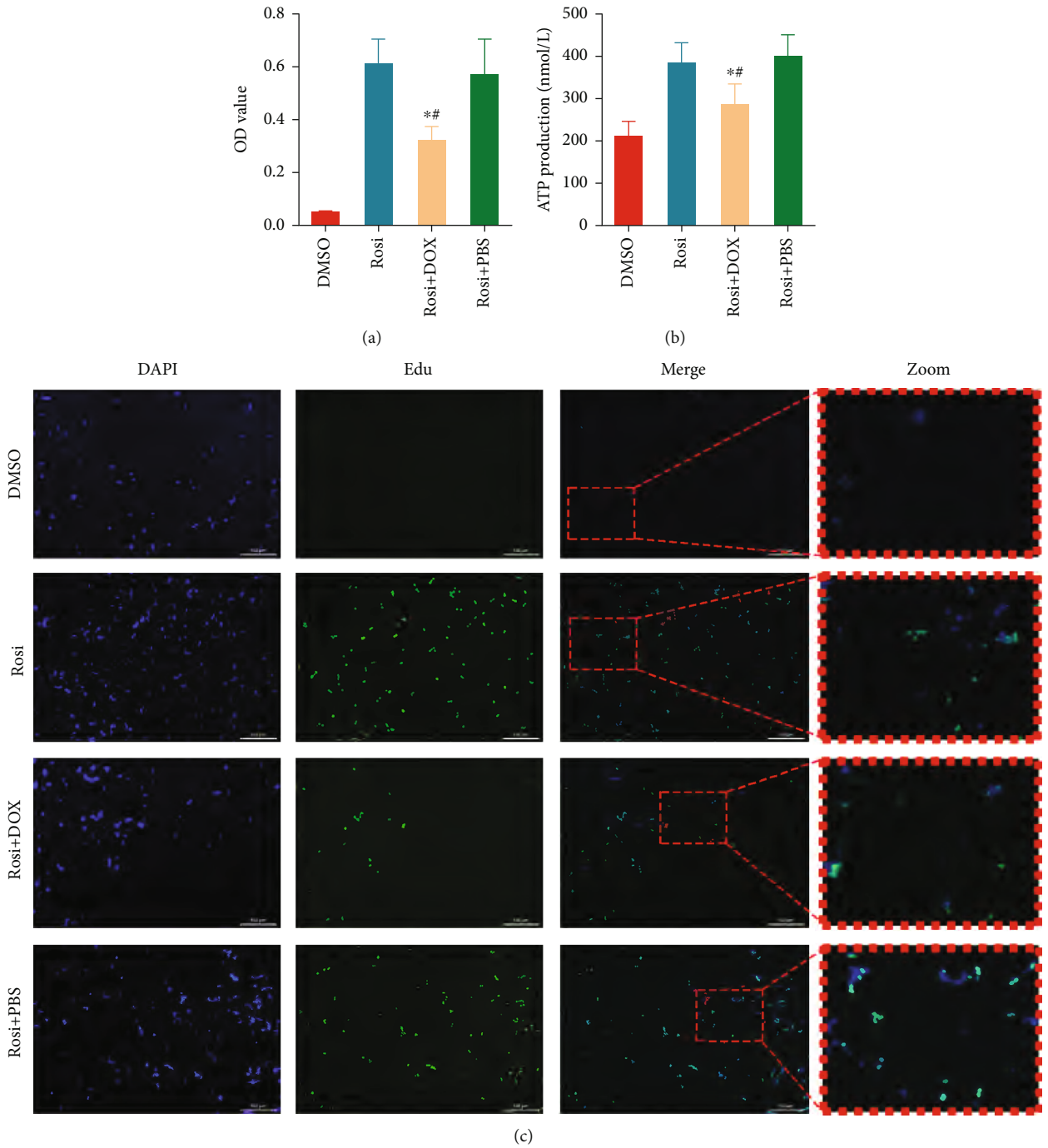

Figure 5: Continued.

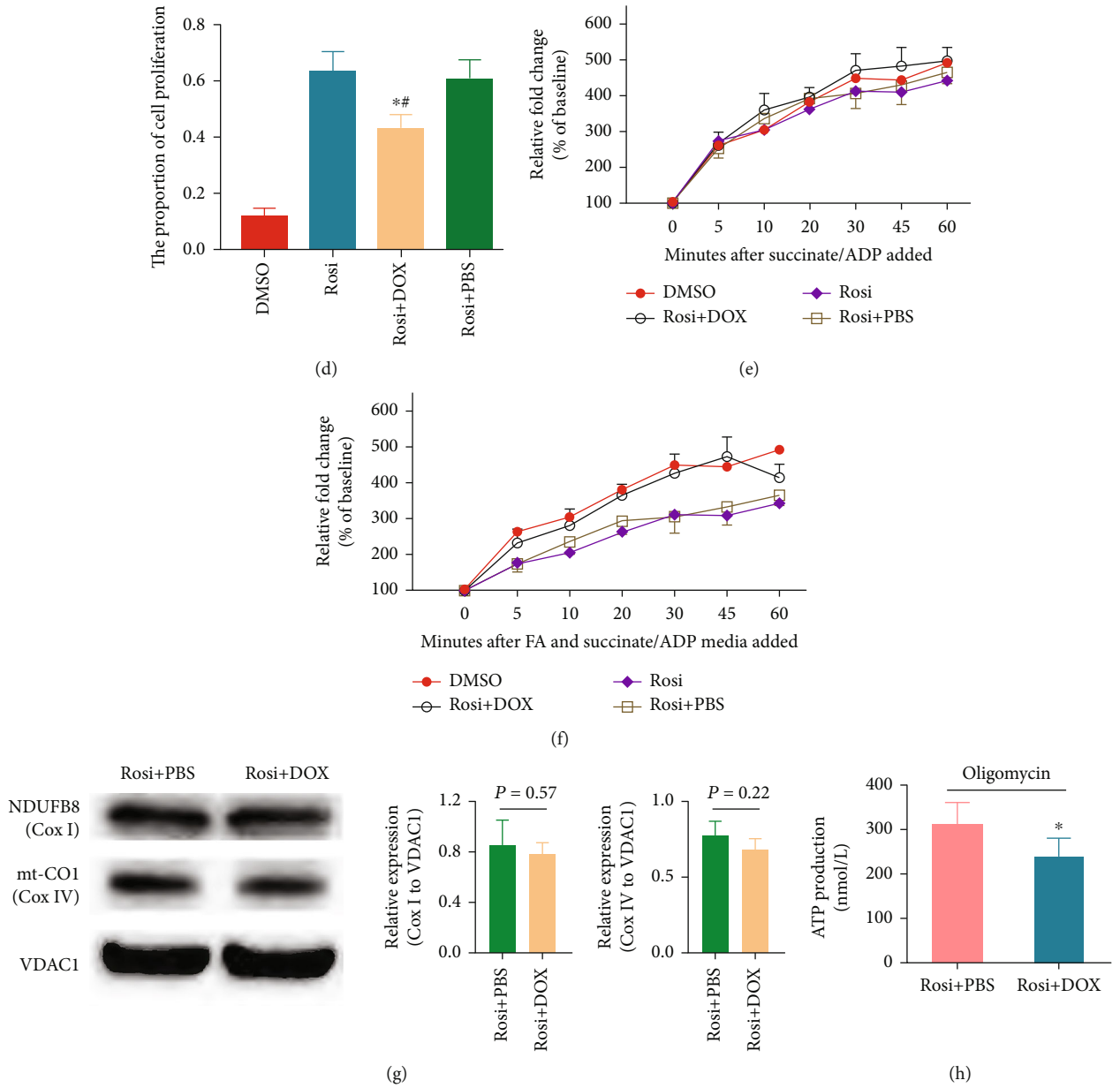

Figure 5: Effects of the forced FOXO1 expression on cell proliferation, mitochondrial OXPHOS, and glycolysis. (a–d) Effects of the forced FOXO1 expression on cell proliferation reflected by CCK-8 measurements (a), ATP production (b), and Edu staining (c, d). The proportions of cell proliferation among four groups were statistically analyzed. DAPI (blue) and Edu (green) represent the nucleus and the newly synthesized DNA, respectively. (e, f) Effects of FOXO1 expression on state 3 respiration in the absence (e) or presence (f) of fatty acid. (g) Ratios of Cox I or IV/VDAC1 were determined by densitometric analysis. Representative immunoblots of Cox I and Cox IV under the forced FOXO1 expression by DOX. VDAC1 served as the loading control. (h) Effect of Rosi on ATP level produced by glycolysis. FOXO1 was induced by DOX to the level similar to that without Rosi. Data represent three independent experiments and are expressed as mean ± SEM (a–c, e–h). $^{*}P < 0.05$ versus Rosi+PBS; $^{\#}P < 0.05$ versus DMSO. FA: fatty acid.

in a 2.47- and 1.46-fold luciferase activity decrement, respectively (Figure 6(b)). Hence, reporter 3, which contained all three FCSs, was the most important in Rosi-induced repression of PINK1 transcription.

We further divided reporter 3 into nine fragments to analyze the functional sequences in detail, with an approximate 50–100 bp overlap between the fragments to ensure that the core sequences were not destroyed. Primers used were listed in Supplementary Tables. The first FOXO1 consensus sequence (FCS1) was located in the −2523 segment, while the second and third consensus sequences were located in the −1779 segment (Figure 6(c), counting from the end of the first intron). Since there is only a 5 bp distance between the second and the third FOXO1 consensus sequences and that it is not easy to analyze them separately, we analyzed these two sequences (FCS2 and FCS3) as a whole (FCS2). Seven of 10 segments showed increased luciferase activity upon FOXO1 expression (Figure 6(d)).

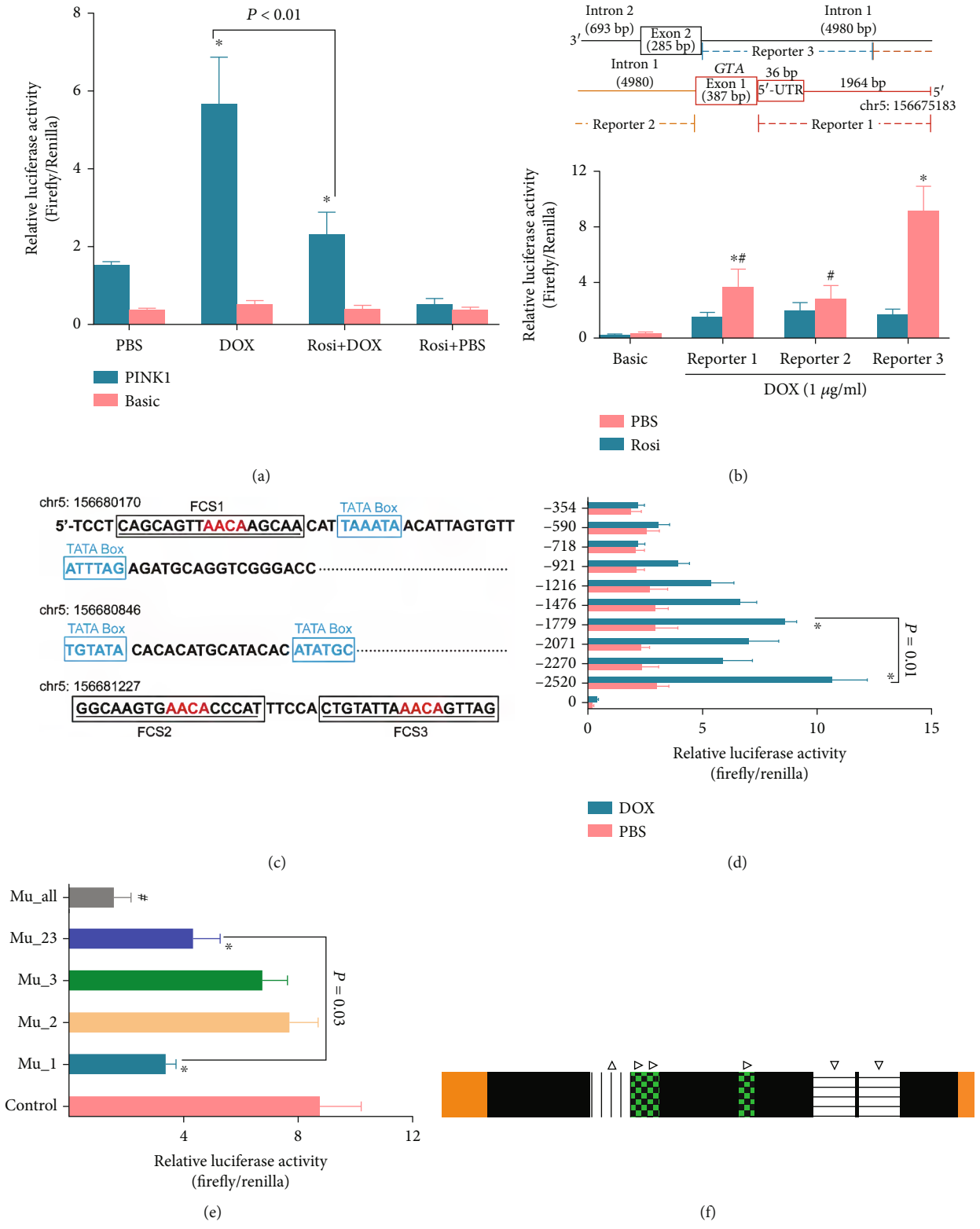

Figure 6: Continued.

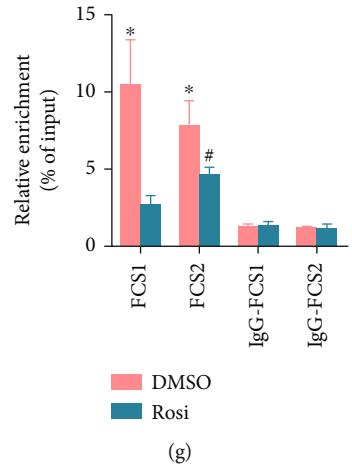

Figure 6: Identification of the core sequences on transcription regulation in the PINK1 gene. (a) Dual-luciferase reporter gene assay results showing region of interest in PINK1 gene increased luciferase activity. The whole region (−2300 bp accounting from the translation site and the first intron) was used. (b) The schematic illustrated three reporters divided from the whole region of interest in PINK1 gene (upper). Dual-luciferase reporter gene assay results showing the effects of the respective reporter in luciferase activity (lower). (c) The schematic illustrating FOXO1 binding sites in the first intron of PINK1 gene predicted by GenomatrixMatInspector. Putative core promoter elements around FOXO1 binding sites were proposed by GPMiner. (d) Dual-luciferase reporter gene assay showing promoter deletion analysis of reporter 3, which contains three FOXO1 binding sites. (e) Effects of FOXO1 binding site mutations on luciferase activity. Control: FOXO1 was induced to expression, and DMSO was added instead of Rosi. (f) The schematic illustrating regulatory elements for transcription in PINK1 gene (upper). Yellow, exons; Black, the first intron. The vertical line, FOXO1 binding site 1 (△); transverse line, FOXO1 binding sites 2 and 3 (▽); green with black blocks inside, TATA box (▷). (g) Results of CHIP analysis using a FOXO1 antibody. Data represent three independent experiments and are expressed as mean ± SEM (a, b, d–f). $^{*}P < 0.05$ versus basic vector (a, b), the 2371 segment (d), the control (e), or the DMSO treatment (f); $^{\#}P < 0.05$ versus basic vector (d) or Mu-1 (e). UTR: untranslated region; FCS: FOXO1 consensus sequences; Mu_1, Mu_2, Mu_3, Mu_23, and Mu_all denote mutations of FCS1, FCS2, FCS3, FCS2/3, and FCS 1/2/3, respectively.

However, unexpectedly, compared with the −1779 segment (FCS2, containing two FOXO1 consensus sequences), the −2523 segment (FCS1, containing one FOXO1 consensus sequence) showed even higher luciferase activity (Figure 6(d)). GPMiner identified distinct distributions of putative core promoter elements around FCS1 and FCS2. Two TATA boxes adjoining the FCS1 were identified, and they were located at 3 bp and 23 bp of the 3′-flank (Figure 6(c), Figure S5). In contrast, the core promoter elements closest to FCS2 were other TATA boxes, located at 381 bp of the 5′-flank (Figure 6(c), Figure S5). Besides the TATA box, no other core promoter element was found within the 500 bp region of both FCS1 and FCS2 (Figure S5).

Site-directed mutagenesis was used to validate the predicted binding sites. All of the predicted binding sites in FCS1 and FCS2 were mutated (FCS1: cagcagtt*AACA*agcaa→cagcagtt*GGTA*agcaa; FCS2: ggcaagtg*AACA*cccat→ggcaagtg-*GGTA*ccat and ctgtatta*AACA*gttag→ctgtatta*GGTA* gttag), and then their transcription activities were compared with those of the wild types. As shown in Figure 6(e), the mutation in FCS1 significantly reduced the luciferase activity, while a mutation in each of the two sites in FCS2 did not significantly affect the transcriptional activity. However, a mutation in both sites in FCS2 resulted in a moderate reduction of the luciferase activity (Figure 6(e)). Notably, the luciferase activity of the mutated FCS1 was lower than that of the mutated FCS2 (Figure 6(e)). Taken together, these data indicated that both FCS1 and FCS2 were involved in the increased PINK1 transcription by FOXO1, but FCS1 was more important.

To confirm that FOXO1 directly binds to the consensus sequences and assess the influence of Rosi, we performed CHIP analysis. FOXO1 expression was induced, and Rosi was administered as previously described. Coimmunoprecipitation with anti-FOXO1 antibody resulted in a positive PCR result using the primer around FOXO1 consensus DNA sequences, while the other primer sets did not yield a positive amplicon. Compared with the DMSO control, Rosi decreased DNA enrichment by anti-FOXO1 protein antibody to approximately 30% (Figure 6(f)). Enrichment of DNA sequences around FCS1 or FCS2 was similar without Rosi, while FCS1 decreased more significantly upon Rosi treatment (Figure 6(f)). The decreased binding capacity may either be because of suppressed FOXO1 expression or due to defects in DNA binding. We used Rosi and DOX (1 μg/mL) together, inducing the constitutive expression of FOXO1 under Rosi treatment to exclude the influence of FOXO1 expression levels on the binding capacity. The CHIP data revealed that Rosi did not significantly affect FCS1 and FCS2 DNA enrichment in the presence of DOX (Figure 6(g)). These results demonstrated that FOXO1 was directly bound to both FCS1 and FCS2 in the first intron of the PINK1 gene. Rosi inhibited this process mainly by decreasing FOXO1 expression rather than by reducing the binding of FOXO1 to the DNA.

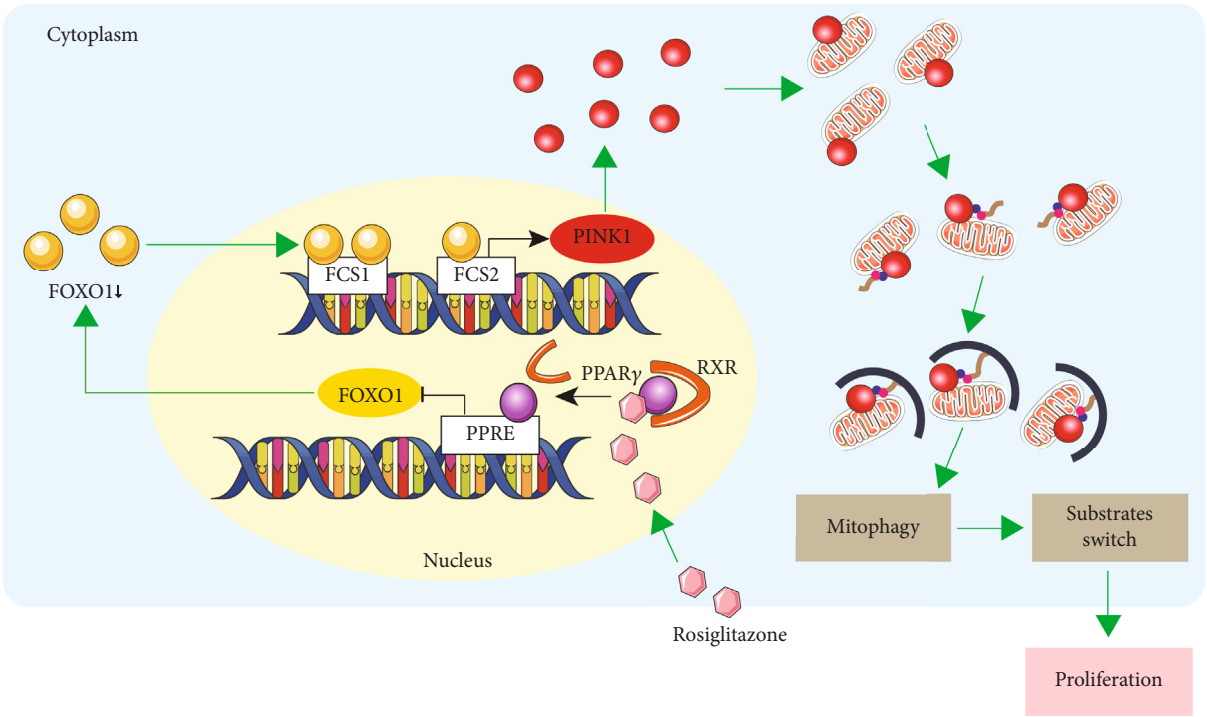

Figure 7: Graphic abstract. The present study showed that the inhibitions of FOXO1 and PINK1 were critically involved in the mechanisms of rosiglitazone-induced mitophagy suppression, which greatly contributed to the enhanced glycolysis and proliferations of NSCs. Besides, we identified that the reduced FOXO1 level, which directly binded to the transcriptional regulation region in PINK1 gene, is the main underlying mechanisms for the decreased PINK1 and mitophagy.

4. Discussion

Inflammation plays a crucial role in neurodegenerative diseases. For example, chronic flammation is implicated in the pathogenesis of Alzheimer's disease and SCI, and blocking inflammation can effectively alleviate the occurrence of the disease [29]. In the process of spinal cord injury, overactivated inflammatory cascade aggravated neuronal necrosis or apoptosis [30, 31]. So reducing the hyperactive inflammation could be beneficial for neural cell survival and SCI. In this study, we found that Rosi can alleviate the expression of inflammatory cytokines IL-1β and IL-6 under SCI, which is consistent with our previous result [32].

NSC proliferation is crucial for the repair of SCI. However, NSCs are the type of cells that proliferate slowly. Therefore, acceleration of the proliferation of NSCs is a matter of considerable importance, and it is also a great challenge in this field. We previously reported the beneficial effects of Rosi [12]. We further explored the underlined physiological mechanism related to mitophagy and NSC proliferation and the detailed molecular mechanism on mitophagy and PINK1 expression regulation in the present study.

In the field of medications for diabetes, metformin, other than TZDs, is the first-line therapy recommended in T2DM guidelines [33]. An *in vitro* study showed the association between metformin usage and neural stem cell proliferation and survival against insults [34–36]. Recent animal studies have also proposed the protective effects of metformin in SCI by inducing nonselective autophagy in neurons [37, 38]. However, there is no direct evidence for metformin *in vivo* proliferation of NSCs is available. In contrast, for TZDs, not only their effects on proliferation in normal rats have been demonstrated in the previous study [39], but they have also been found to be beneficial in recovery from SCI and promotion of proliferation of NSCs in SCI rats in the present study. Thus, our study may indicate the preference for using TZDs in diabetic SCI patients.

To our knowledge, this is the first study related to mitophagy in the biological function of NSCs. Unlike nonselective autophagy, mitophagy is triggered by specific mechanisms, such as PINK1/Parkin, BINP3, NIX, and FUNDC1 pathways. PINK1 expression is crucial for the PINK1/Parkin pathway, which is recognized as the classical trigger and the most important factor in mitophagy, and it plays a role in various disease conditions. Mitophagy serves as a compensatory mechanism upon loss of mitochondrial potential. It is believed to improve mitochondrial function and reduce apoptosis [40]. This seems to be contradictory to the proliferative effects of reduced mitophagy conferred by Rosi observed in our study. However, it should be noted that, in the absence of any other treatment, the membrane potential and ROS production were similar between Rosi- and DMSO-treated NSCs, but enhanced mitophagy was observed in DMSO-treated cells in this situation. This indicates that redundant mitophagy exists in NSCs. Excessive mitophagy leads to neuronal death, and internal environmental disturbance has been observed [41, 42]. Recently, inadequate activation of mitophagy has been reported to cause aberrant homeostasis in some stem cells [43, 44].

Moreover, mitophagy maturation has been recognized as the hallmark of a metabolic substrate switch from fatty acids to glucose [19]. Such a shift may cause a decrease in glucose bioavailability, resulting in a "glucose deprivation-like" effect and impairing proliferation because certain glucose utilization levels have been demonstrated to promote self-renewal of NSCs [45]. Indeed, as found in our work, Rosi resulted in a reduction in oxygen consumption in the presence of fatty acids and an increase in glycolysis, which supported the role of Rosi in maintaining glucose utilization in NSCs. Therefore, although mitophagy is considered a compensatory response, Rosi modulates substrate metabolism and ATP production methods through the regulation of mitophagy, which finally accelerates the proliferation of NSCs.

There has been limited research concerning Rosi and mitophagy. Their associations were presented in two studies, which reported a decrease in mitophagy but the promotion of mitochondrial biogenesis in both adipose and kidney proximal tubular epithelial cells [46, 47], which is in accordance with the findings of the present study. Currently, no research has directly evaluated the association between TZDs and mitophagy in the nervous system except for the present study. However, a previous study showed that Rosi prevented the loss of mitochondrial PINK1 in neuroblastoma [48], which implied decreased mitophagy. Some studies have focused on Rosi and nonselective autophagy. Rosi has been reported to inhibit autophagy in the spinal cord tissue, but no specific cell type was identified [49]. Other studies showed that Rosi induced autophagy in neurons [50]. Therefore, Rosi may contribute to both promotion and inhibition of autophagy depending on the pathological condition [50, 51]. Besides, previous studies on the association of mitochondrial markers supported the effects of Rosi on mitochondrial biogenesis observed in the present study. We observed the increase in red fluorescence and significantly enhanced green fluorescence by mitoTimer, which indicated an increased amount in mitochondria. These results are supported by the previous NSC studies consistently documenting an increased expression of PPAR coactivator-1α, a critical transcriptional factor in mitochondrial biogenesis [13–15]. Thus, the present study suggested that mitochondrial clearance and biogenesis could be regulated simultaneously.

In the present study, we characterized the core regulatory sequences involved in the regulation of PINK1 by Rosi. The promoter region of PINK1 in either humans or rodents has not yet been identified. FOXO1 has been reported to bind to the PINK1 promoter and induce transcription. Still, a specific binding site has not been investigated, and the primers used for CHIP resulted in a product exceeding 1600 bp [52]. Hou and colleagues identified the sequence of a 0.4 kbp segment of the DNA immediately 5′-flank to the PINK1 translation start site that bound to FOXO3a in a mouse model [53]. Other studies also identified a segment consisting of 3060 bp (−3061 bp to −1 bp counting from the translation start site) and a segment composed of 1825 bp (−1799 to +26 bp counting from the transcription start site) as the promoter regions of the human PINK1 gene [54, 55]. Currently, to our knowledge, this is the first study to report the sequences involved in the regulation of PINK1 transcription in rats, which could be recognized as a part of the promoter region. We confirmed that the binding site of FOXO1 is located inside the first intron, instead of the regular −2300 bp upstream of the translation start site. This is not surprising since the intron is widely known to participate in the regulation of gene transcription [56–59].

Some limitations of the current study should be acknowledged. First, Rosi has been reported to maintain the undifferentiated phenotypes of NSCs [60], but we did not investigate the differentiation capacity of NSCs, thus leading to a lack of clarity on the potency of NSCs to differentiate into mature neurons. Second, we did not further explore the effect of -directed mutagenesis in PINK1 promoter on NSC proliferation, leading to the unknown of potential NSC proliferation alteration conferred by mutagenesis in PINK1 promoter. Finally, the effects of FOXO1 and PINK1 in Rosi-induced NSCs proliferation were not examined *in vivo*.

In summary, the present study provided data showing the effects of SCI repairment, inflammation inhibition, NSC proliferation, and mitophagy suppression conferred by Rosi and confirming the causality between mitophagy suppression and NSC proliferation. Moreover, we demonstrated the role of FOXO1 targeting the first intron of PINK1 in Rosi-induced mitophagy inhibition, metabolic substrate shift, and proliferation of NSCs. Furthermore, the regulatory sequences inside the PINK1 promoter region that responded to Rosi and FOXO1 were identified in depth (Figure 7).

Data Availability

The authors declare that all data supporting the findings of this study are available within the paper and its supplementary information files.

Conflicts of Interest

All authors declare no potential conflict of interest.

Authors' Contributions

Qingqi Meng, Zhiteng Chen, and Qingyuan Gao contributed equally to this work and should be considered as co-first authors.

Acknowledgments

This work was supported by the National Natural Science Foundation of China (81870334, 81300279, 81741067, 31670742), the science and Technology Program of Guangdong (2020A1515011237), the Science and Technology Program of Guangzhou City (231804010050, 202102080344), and the Guangdong Natural Science Foundation (2020A0303135212, 2021A1515011109).

Supplementary Materials

Figure S1: effects of Rosi on oxidative phosphorylation and glycolysis. (A, B) Effects of rosiglitazone on state 2 and state 3 respiration at steady-state. Oxygen consumption was similar during basic state 2 and state 3 respiration between Rosi and DMSO treatments while it was slightly increased by treatments with higher doses of Rosi. (C) Rosi moderately or significantly reduced state 3 respiration under CCCP treatment dependent on the concentration of Rosi. (D) Rosi dramatically reduced state 3 respiration in fatty acid (FA) media, and it reduced approximately half of the oxygen consumption compared with that in the DMSO-treated cells. (E) Results of western blotting for the respiratory complexes showed that Rosi slightly increased the complex I content in the mitochondrion, and it did not affect complex IV expression. VDAC1 was served as the loading control. Data represented three independent experiments and were expressed as mean ± SEM (A–D). $^{*}P < 0.05$ versus DMSO treatment; $^{\#}P < 0.05$ versus 30 μg/mL Rosi (D). ADP: adenosine diphosphate. Figure S2: effects of different rosiglitazone concentrations on supernatant lactate contents. Only a slight increase in lactic acid was observed. Data represented three independent experiments and were expressed as mean ± SEM. Figure S3: effects of Rosi on the mRNA and protein contents of FUNDC1, BNIP3, and NIX in NSCs. The mRNA and protein contents were measured by RT-qPCR (A) and western blotting (B), respectively. β-Actin was used as internal reference. Data represented three independent experiments and were expressed as mean ± SEM. Figure S4: effects of the forced FOXO1 expression on Rosi-induced mitophagy suppression. FOXO1 expression was induced by doxycycline (DOX, 1 μg/mL), and the same volume of PBS was used as control. (A) Confocal immunofluorescence images showing LC3B (red) and Tomm20 (green) in NSCs. (B) Confocal images showing the fluorescence of mitoTimer. Rosi was applied in all the groups additionally to the indicated treatments. Scale bar represents 10 μm. Figure S5: results for putative core regulatory element prediction of the first intron in PINK1 gene by the GPMiner method. Table S1: primers for promoter deletion analysis for reporter 3. Table S2: primers for site mutations. Table S3: primers for real-time PCR. *(Supplementary Materials)*

References

[1] A. R. Sas, K. S. Carbajal, A. D. Jerome et al., "A new neutrophil subset promotes CNS neuron survival and axon regeneration," *Nature Immunology*, vol. 21, no. 12, pp. 1496–1505, 2020.

[2] I. Paterniti, E. Esposito, and S. Cuzzocrea, "Phosphodiesterase as a new therapeutic target for the treatment of spinal cord injury and neurodegenerative diseases," *Current Medicinal Chemistry*, vol. 21, no. 24, pp. 2830–2838, 2014.

[3] T. Kuboyama, C. Tohda, and K. Komatsu, "Effects of Ashwagandha (roots of Withania somnifera) on neurodegenerative diseases," *Biological & Pharmaceutical Bulletin*, vol. 37, no. 6, pp. 892–897, 2014.

[4] N. A. Silva, N. Sousa, R. L. Reis, and A. J. Salgado, "From basics to clinical: a comprehensive review on spinal cord injury," *Progress in Neurobiology*, vol. 114, pp. 25–57, 2014.

[5] K. Karova, J. V. Wainwright, L. Machova-Urdzikova et al., "Transplantation of neural precursors generated from spinal progenitor cells reduces inflammation in spinal cord injury via NF-κB pathway inhibition," *Journal of Neuroinflammation*, vol. 16, no. 1, p. 12, 2019.

[6] L. Noori, S. Arabzadeh, Y. Mohamadi et al., "Intrathecal administration of the extracellular vesicles derived from human Wharton's jelly stem cells inhibit inflammation and attenuate the activity of inflammasome complexes after spinal cord injury in rats," *Neuroscience research*, vol. 170, pp. 87–98, 2021.

[7] A. Younsi, G. Zheng, M. Scherer et al., "Three growth factors induce proliferation and differentiation of neural precursor cells *in vitro* and support cell-transplantation after spinal cord injury *in vivo*," *Stem Cells International*, vol. 2020, 15 pages, 2020.

[8] L. D. Hachem, A. J. Mothe, and C. H. Tator, "Positive modulation of AMPA receptors promotes survival and proliferation of neural stem/progenitor cells from the adult rat spinal cord," *Stem Cells and Development*, vol. 26, no. 23, pp. 1675–1681, 2017.

[9] D. Wang, K. Wang, Z. Liu, Z. Wang, and H. Wu, "Valproic acid labeled chitosan nanoparticles promote the proliferation and differentiation of neural stem cells after spinal cord injury," *Neurotoxicity Research*, vol. 39, no. 2, pp. 456–466, 2021.

[10] M. Cusimano, E. Brambilla, A. Capotondo et al., "Selective killing of spinal cord neural stem cells impairs locomotor recovery in a mouse model of spinal cord injury," *Journal of Neuroinflammation*, vol. 15, no. 1, p. 58, 2018.

[11] J. E. Shin, K. Jung, M. Kim et al., "Brain and spinal cord injury repair by implantation of human neural progenitor cells seeded onto polymer scaffolds," *Experimental & molecular medicine*, vol. 50, no. 4, pp. 1–18, 2018.

[12] Q.-Q. Meng, W. Lei, H. Chen et al., "Combined rosiglitazone and Forskolin have neuroprotective effects in SD rats after spinal cord injury," *PPAR Research*, vol. 2018, Article ID 3897478, 11 pages, 2018.

[13] M.-C. Chiang, C. J. Nicol, Y.-C. Cheng, K. H. Lin, C. H. Yen, and C. H. Lin, "Rosiglitazone activation of PPARγ-dependent pathways is neuroprotective in human neural stem cells against amyloid-beta-induced mitochondrial dysfunction and oxidative stress," *Neurobiology of Aging*, vol. 40, pp. 181–190, 2016.

[14] M. C. Chiang, Y. C. Cheng, K. H. Lin, and C. H. Yen, "PPARγ regulates the mitochondrial dysfunction in human neural stem cells with tumor necrosis factor alpha," *Neuroscience*, vol. 229, pp. 118–129, 2013.

[15] M.-C. Chiang, Y.-C. Cheng, C. J. Nicol, and C. H. Lin, "The neuroprotective role of rosiglitazone in advanced glycation end product treated human neural stem cells is PPAR-gamma-dependent," *The International Journal of Biochemistry & Cell Biology*, vol. 92, pp. 121–133, 2017.

[16] M. Vara-Perez, B. Felipe-Abrio, and P. Agostinis, "Mitophagy in cancer: a tale of adaptation," *Cells*, vol. 8, no. 5, p. 493, 2019.

[17] Y. Zhao, S. Huang, J. Liu et al., "Mitophagy contributes to the pathogenesis of inflammatory diseases," *Inflammation*, vol. 41, no. 5, pp. 1590–1600, 2018.

[18] J. Harris, N. Deen, S. Zamani, and M. A. Hasnat, "Mitophagy and the release of inflammatory cytokines," *Mitochondrion*, vol. 41, pp. 2–8, 2018.

[19] G. Gong, M. Song, G. Csordas, D. P. Kelly, S. J. Matkovich, and G. W. Dorn II, "Parkin-mediated mitophagy directs perinatal cardiac metabolic maturation in mice," *Science (New York, N.Y.)*, vol. 350, no. 6265, 2015.

[20] H. Zhang, K. J. Menzies, and J. Auwerx, "The role of mitochondria in stem cell fate and aging," *Development (Cambridge, England)*, vol. 145, no. 8, 2018.

[21] C. Lange, M. Turrero Garcia, I. Decimo et al., "Relief of hypoxia by angiogenesis promotes neural stem cell differentiation by targeting glycolysis," *The EMBO Journal*, vol. 35, no. 9, pp. 924–941, 2016.

[22] J. Zhang, L. Liu, Y. Xue et al., "Endothelial monocyte-activating polypeptide-II induces BNIP3-mediated mitophagy to enhance temozolomide cytotoxicity of glioma stem cells via down-regulating MiR-24-3p," *Frontiers in Molecular Neuroscience*, vol. 11, p. 92, 2018.

[23] C. L. Koehler, G. A. Perkins, M. H. Ellisman, and D. L. Jones, "Pink1 and Parkin regulate drosophila intestinal stem cell proliferation during stress and aging," *The Journal of Cell Biology*, vol. 216, no. 8, pp. 2315–2327, 2017.

[24] G. Hernandez, C. Thornton, A. Stotland et al., "MitoTimer: a novel tool for monitoring mitochondrial turnover," *Autophagy*, vol. 9, no. 11, pp. 1852–1861, 2013.

[25] A. Mazzone, S. J. Gibbons, C. E. Bernard et al., "Identification and characterization of a novel promoter for the human *ANO1* gene regulated by the transcription factor signal transducer and activator of transcription 6 (STAT6)," *FASEB Journal : Official Publication of the Federation of American Societies for Experimental Biology*, vol. 29, no. 1, pp. 152–163, 2015.

[26] H.-F. Zhang, M.-X. Wu, Y.-Q. Lin et al., "IL-33 promotes IL-10 production in macrophages: a role for IL-33 in macrophage foam cell formation," *Experimental & Molecular Medicine*, vol. 49, no. 11, article e388, 2017.

[27] T. B. Silva, C. Z. Oliveira, E. F. Faria, E. C. Mauad, K. J. Syrjänen, and A. L. Carvalho, "Development and validation of a nomogram to estimate the risk of prostate cancer in Brazil," *Anticancer Research*, vol. 35, no. 5, pp. 2881–2886, 2015.

[28] F. Hadji, M.-C. Boulanger, S.-P. Guay et al., "Altered DNA methylation of long noncoding RNA H19 in calcific aortic valve disease promotes mineralization by silencing NOTCH1," *Circulation*, vol. 134, no. 23, pp. 1848–1862, 2016.

[29] C. Holmes, "Review: systemic inflammation and Alzheimer's disease," *Neuropathology and Applied Neurobiology*, vol. 39, no. 1, pp. 51–68, 2013.

[30] C. S. Ahuja and M. Fehlings, "Concise review: bridging the gap: novel neuroregenerative and neuroprotective strategies in spinal cord injury," *Stem Cells Translational Medicine*, vol. 5, no. 7, pp. 914–924, 2016.

[31] B. Zhang and J. C. Gensel, "Is neuroinflammation in the injured spinal cord different than in the brain? Examining intrinsic differences between the brain and spinal cord," *Experimental Neurology*, vol. 258, pp. 112–120, 2014.

[32] Q.-Q. Meng, Z.-C. Feng, X.-L. Zhang et al., "PPAR-γ Activation Exerts an Anti-inflammatory Effect by Suppressing the NLRP3 Inflammasome in Spinal Cord-Derived Neurons," *Mediators of Inflammation*, vol. 2019, Article ID 6386729, 12 pages, 2019.

[33] R. R. Kalyani, C. P. Cannon, A. L. Cherrington et al., "Professional Practice Committee: *Standards of Medical Care in Diabetes-2018*," *Diabetes Care*, vol. 41, Supplement 1, pp. S3–S3, 2018.

[34] M. Fatt, K. Hsu, L. He et al., "Metformin acts on two different molecular pathways to enhance adult neural precursor proliferation/self-renewal and differentiation," *Stem Cell Reports*, vol. 5, no. 6, pp. 988–995, 2015.

[35] M.-M. Chung, C. J. Nicol, Y.-C. Cheng et al., "Metformin activation of AMPK suppresses AGE-induced inflammatory response in hNSCs," *Experimental Cell Research*, vol. 352, no. 1, pp. 75–83, 2017.

[36] C.-H. Lin, Y.-C. Cheng, C. J. Nicol, K. H. Lin, C. H. Yen, and M. C. Chiang, "Activation of AMPK is neuroprotective in the oxidative stress by advanced glycosylation end products in human neural stem cells," *Experimental Cell Research*, vol. 359, no. 2, pp. 367–373, 2017.

[37] Y. Guo, F. Wang, H. Li et al., "Metformin protects against spinal cord injury by regulating autophagy via the mTOR signaling pathway," *Neurochemical Research*, vol. 43, no. 5, pp. 1111–1117, 2018.

[38] P. Wang, Z.-D. Xie, C.-N. Xie et al., "AMP-activated protein kinase-dependent induction of autophagy by erythropoietin protects against spinal cord injury in rats," *CNS Neuroscience & Therapeutics*, vol. 24, no. 12, pp. 1185–1195, 2018.

[39] J. A. Morales-Garcia, R. Luna-Medina, C. Alfaro-Cervello et al., "Peroxisome proliferator-activated receptor γ ligands regulate neural stem cell proliferation and differentiation in vitro and in vivo," *Glia*, vol. 59, no. 2, pp. 293–307, 2011.

[40] S. Pickles, P. Vigié, and R. J. Youle, "Mitophagy and quality control mechanisms in mitochondrial maintenance," *Current biology : CB*, vol. 28, no. 4, pp. R170–R185, 2018.

[41] R. Shi, J. Weng, L. Zhao, X. M. Li, T. M. Gao, and J. Kong, "Excessive autophagy contributes to neuron death in cerebral ischemia," *CNS Neuroscience & Therapeutics*, vol. 18, no. 3, pp. 250–260, 2012.

[42] E. P. K. Yu, J. Reinhold, H. Yu et al., "Mitochondrial respiration is reduced in atherosclerosis, promoting necrotic core formation and reducing relative fibrous cap thickness," *Arteriosclerosis, Thrombosis, and Vascular Biology*, vol. 37, no. 12, pp. 2322–2332, 2017.

[43] G. Jin, C. Xu, X. Zhang et al., "Atad3a suppresses Pink1-dependent mitophagy to maintain homeostasis of hematopoietic progenitor cells," *Nature Immunology*, vol. 19, no. 1, pp. 29–40, 2018.

[44] C. Yang and T. Suda, "Hyperactivated mitophagy in hematopoietic stem cells," *Nature Immunology*, vol. 19, no. 1, pp. 2-3, 2018.

[45] S. Fusco, L. Leone, S. A. Barbati et al., "A CREB-Sirt1-Hes1 circuitry mediates neural stem cell response to glucose availability," *Cell Reports*, vol. 14, no. 5, pp. 1195–1205, 2016.

[46] D. M. Small, C. Morais, J. S. Coombes, N. C. Bennett, D. W. Johnson, and G. C. Gobe, "Oxidative stress-induced alterations in PPAR-γ and associated mitochondrial destabilization contribute to kidney cell apoptosis," *American journal of physiology Renal physiology*, vol. 307, no. 7, pp. F814–F822, 2014.

[47] D. Taylor and R. A. Gottlieb, "Parkin-mediated mitophagy is downregulated in browning of white adipose tissue," *Obesity (Silver Spring, Md)*, vol. 25, no. 4, pp. 704–712, 2017.

[48] J. C. Corona, S. C. de Souza, and M. R. Duchen, "PPARγ activation rescues mitochondrial function from inhibition of complex I and loss of PINK1," *Experimental Neurology*, vol. 253, pp. 16–27, 2014.

[49] H. Li, Q. Zhang, X. Yang, and L. Wang, "PPAR-γ agonist rosiglitazone reduces autophagy and promotes functional recovery

in experimental traumaticspinal cord injury," *Neuroscience Letters*, vol. 650, pp. 89–96, 2017.

[50] Z. Zhao, L. Zhang, X.-D. Guo et al., "Rosiglitazone exerts an anti-depressive effect in unpredictable chronic mild-stress-induced depressive mice by maintaining essential neuron autophagy and inhibiting excessive astrocytic apoptosis," *Frontiers in Molecular Neuroscience*, vol. 10, p. 293, 2017.

[51] Z.-Q. Shao and Z.-J. Liu, "Neuroinflammation and neuronal autophagic death were suppressed via rosiglitazone treatment: new evidence on neuroprotection in a rat model of global cerebral ischemia," *Journal of the Neurological Sciences*, vol. 349, no. 1-2, pp. 65–71, 2015.

[52] W. Li, M. du, Q. Wang et al., "FoxO1 promotes mitophagy in the podocytes of diabetic male mice via the PINK1/Parkin pathway," *Endocrinology*, vol. 158, no. 7, pp. 2155–2167, 2017.

[53] Y. Mei, Y. Zhang, K. Yamamoto, W. Xie, T. W. Mak, and H. You, "FOXO3a-dependent regulation of Pink1 (Park6) mediates survival signaling in response to cytokine deprivation," *Proceedings of the National Academy of Sciences of the United States of America*, vol. 106, no. 13, pp. 5153–5158, 2009.

[54] X. Duan, J. Tong, Q. Xu et al., "Upregulation of human PINK1 gene expression by NFκB signalling," *Molecular Brain*, vol. 7, no. 1, p. 57, 2014.

[55] H. Murata, H. Takamatsu, S. Liu, K. Kataoka, N. H. Huh, and M. Sakaguchi, "NRF2 regulates *PINK1* expression under oxidative stress conditions," *PLoS One*, vol. 10, no. 11, article e0142438, 2015.

[56] G. D. Tomaras, D. A. Foster, C. M. Burrer, and S. M. Taffet, "ETS transcription factors regulate an enhancer activity in the third intron of TNF-alpha," *Journal of Leukocyte Biology*, vol. 66, no. 1, pp. 183–193, 1999.

[57] H. Jin, R. J. van't Hof, O. M. E. Albagha, and S. H. Ralston, "Promoter and intron 1 polymorphisms of COL1A1 interact to regulate transcription and susceptibility to osteoporosis," *Human Molecular Genetics*, vol. 18, no. 15, pp. 2729–2738, 2009.

[58] P. Heyn, A. T. Kalinka, P. Tomancak, and K. M. Neugebauer, "Introns and gene expression: cellular constraints, transcriptional regulation, and evolutionary consequences," *BioEssays : news and reviews in molecular, cellular and developmental biology*, vol. 37, no. 2, pp. 148–154, 2015.

[59] M. Laxa, K. Müller, N. Lange, L. Doering, J. T. Pruscha, and C. Peterhänsel, "The 5'UTR intron of Arabidopsis GGT1 aminotransferase enhances promoter activity by recruiting RNA polymerase II," *Plant Physiology*, vol. 172, no. 1, pp. 313–327, 2016.

[60] C. Bernal, C. Araya, V. Palma, and M. Bronfman, "PPARÎ²/Î´ and PPARÎ³ maintain undifferentiated phenotypes of mouse adult neural precursor cells from the subventricular zone," *Frontiers in Cellular Neuroscience*, vol. 9, p. 78, 2015.

Hindawi
Oxidative Medicine and Cellular Longevity
Volume 2021, Article ID 7716201, 16 pages
https://doi.org/10.1155/2021/7716201

Research Article

Botanical Drug Puerarin Ameliorates Liposaccharide-Induced Depressive Behaviors in Mice via Inhibiting RagA/mTOR/p70S6K Pathways

Jia Zhao,[1,2,3,4] **Yizhen Jia**,[1] **Wei Zhao**,[2] **Huixin Chen**,[2] **Xiuying Zhang**,[2] **Fung Yin Ngo**,[2] **Dan Luo**,[2] **Youqiang Song**,[5] **Lixing Lao**,[2] **and Jianhui Rong**[2,6]

[1]*Department of Chinese Medicine, The University of Hong Kong Shenzhen Hospital, Shenzhen, China*
[2]*School of Chinese Medicine, The University of Hong Kong, 10 Sassoon Road, Pokfulam, Hong Kong, China*
[3]*Zhu Nansun's Workstation, School of Chinese Medicine, The University of Hong Kong, 10 Sassoon Road, Pokfulam, Hong Kong, China*
[4]*Yu Jin's Workstation, School of Chinese Medicine, The University of Hong Kong, 10 Sassoon Road, Pokfulam, Hong Kong, China*
[5]*School of Biomedical Science, The University of Hong Kong, 21 Sassoon Road, Pokfulam, Hong Kong, China*
[6]*The University of Hong Kong Shenzhen Institute of Research and Innovation (HKU-SIRI), Shenzhen, China*

Correspondence should be addressed to Jianhui Rong; jrong@hkucc.hku.hk

Received 10 May 2021; Revised 27 September 2021; Accepted 29 September 2021; Published 18 October 2021

Academic Editor: Xiaolei Shi

Background. The depressive symptom hallmarks the progression of the neurodegenerative diseases, especially Alzheimer's disease. Bacterial infection is related to inflammation and depression. The present project thereby examined whether botanical drug puerarin could attenuate liposaccharide- (LPS-) induced depressive behaviors in mice. *Methods*. Adult male C57BL/6N mice were sequentially treated with LPS and puerarin and evaluated for the depressive behaviors by tail suspension test and forced swim test. The brain tissues were profiled for the molecular targets of puerarin by next-generation RNA sequencing technique. Candidate targets were further verified in LPS-treated mice, neural stem cells, and highly differentiated PC12 cell line. *Results*. Puerarin ameliorated LPS-induced depression in the mice. RNA sequencing profiles revealed that puerarin altered the expression of 16 genes while markedly downregulated Ras-related GTP-binding protein A (RagA) in LPS-treated mice. The effect of puerarin on RagA expression was confirmed by immunostaining, Western blot, and quantitative real-time PCR (qRT-PCR). Biochemical studies showed that puerarin inhibited RagA/mTOR/p70S6K pathway, attenuated the accumulation of mTORC1 in close proximity to lysosome, and reduced the production of proinflammatory cytokines. *Conclusions*. Botanical drug puerarin attenuated inflammation and depressive behaviors in LPS-challenged mice by inhibiting RagA/mTOR/p70S6K pathways. Puerarin may be a lead compound for the new antidepressant drugs.

1. Introduction

Alzheimer's disease (AD) is characterized by memory loss and cognitive deficit due to progressive neurodegeneration [1]. Most of AD patients suffer from depression while severe depression affects over 264 million people (https://www.who.int/). Infection and social stress dramatically increase the prevalence of depression worldwide [2]. The etiology of the depression remains elusive. Among several risk factors, neuroinflammation is recently identified to be highly related to depression [3]. The proinflammatory cytokines including interleukin- (IL-) 1β and IL-6 were increased whereas the anti-inflammatory cytokines including IL-10 and IL-4 were decreased in depression [4]. Moreover, bacterial lipopolysaccharide (LPS) induces inflammation and depression in mice [5–7]. Our previous study showed that LPS induced

depression in mice by upregulating small guanosine triphosphatases (GTPases) RagA expression and subsequently activating mammalian target of rapamycin (mTOR)/p70S6K pathway [8]. Therefore, the RagA/mTOR/p70S6K pathway may be a therapeutic target for the treatment of depression.

The mTOR pathway is a key mechanism in the regulation of protein synthesis, cellular metabolism, and autophagy while mTOR is also implicated in the proliferation of neural stem cells and circadian rhythms [9]. Two different mTOR complexes (e.g., mTORC1 and mTORC2) execute the biological functions in response to specific stimuli [10]. The complex mTORC1 facilitates the cell growth by inhibiting autophagy and the expression of lysosomal genes whereas mTORC2 phosphorylates and activates PKB/Akt and PKC kinase, thereby promoting cell survival [11]. The mTORC1 pathway is dysregulated in the neurodegenerative diseases [12]. Nutrients promote mTORC1 translocation to the lysosomal membrane and activate the mTORC1 pathway via Rag GTPases [13]. On the other hand, Rag GTPases exist in four isoforms, namely, RagA, RagB, RagC, and RagD, and often form heterodimers (e.g., RagA/B, RagC/D). Upon stimulation by the nutrients, the complex RagA/B binds guanosine triphosphate (GTP) whereas the complex RagC/D binds guanosine diphosphate (GDP). The activation of Rag GTPases promotes the lysosomal localization of mTORC1 to facilitate the interaction of mTORC1 with the kinase activator Rheb [14, 15]. The active mTORC1 colocalizes with the lysosomal biomarker lysosome-associated membrane protein (LAMP2) and regulates the lysosomal biogenesis [16, 17]. Moreover, the activation of mTORC1 induces the phosphorylation of the downstream targets including p70 S6 kinase (p70S6K) and eukaryotic translation initiation factor 4E-binding protein 1 (4E-BP1), thereby driving the onset of depression [18, 19].

The conventional antidepressant drugs have been found to have various side effects in the past couple of decades [20]. As an example, ketamine exhibits rapid antidepressant effects via regulating 4E-BPs [19]. However, ketamine causes various side effects and even toxicity because its abuse harms people and society [21]. On the other hand, natural products could effectively attenuate LPS-induced depression in mice [22]. Along this line, our group recently demonstrated that C-glucosylated isoflavone puerarin (Figure 1(a)), as the main active compound from the herbal medicine Radix puerariae, attenuated pain and depression in mice with spared nerve injury [23]. Consistently, other studies also showed that puerarin attenuated depressive-like behaviors by upregulating FGF_2 expression or via estrogen and BDNF signaling pathways [24, 25]. Thus, it would be of importance to further dissect the mechanism by which puerarin exhibits antidepressant activity.

In the present study, we hypothesized that puerarin could attenuate the depressive-like behaviors in LPS-challenged mice. Following puerarin treatment, depressive-like behaviors were assessed in the LPS-challenged mice. The brain tissues were subjected to the transcriptome profiling for the molecular targets of puerarin. The candidate targets of puerarin were further verified in LPS-treated mice, neural stem cells, and highly differentiated PC12 cell line.

2. Materials and Methods

2.1. Antibodies and Biochemical Reagents. The antibodies against RagA, phospho-mTOR, mTOR, phospho-p70S6K, p70S6K, and GAPDH were obtained from Cell Signaling Technology (Boston, MA, USA). HRP-conjugated anti-rabbit IgG was purchased from Sigma–Aldrich (St. Louis, MO, USA). NeuN and LAMP2 antibodies were purchased from Abcam (Cambridge, MA, USA). Alexa Fluor 488-conjugated goat anti-mouse IgG and Alexa Fluor 594-conjugated goat anti-rabbit IgG were obtained from Invitrogen (Carlsbad, CA, USA). ChamQ SYBR qPCR master mix was obtained from Vazyme (Nanjing, China). QuantiNova SYBR green PCR kit was obtained from QIAGEN (Valencia, CA, USA). Dulbecco's modified Eagle's medium (DMEM), DMEM/F12, fetal bovine serum (FBS), horse serum (HS), N2, B27, penicillin, streptomycin, basic fibroblast growth factor (bFGF), and epidermal growth factor (EGF) were obtained from Thermo Fisher Scientific (Waltham, MA, USA). The mammalian expression vector pcDNA3.1 was obtained from Invitrogen (Carlsbad, CA, USA). Puerarin was obtained from Yick-Vic Chemicals & Pharmaceuticals (Hong Kong, China). LPS, Accumax solution, RIPA buffer, and other reagents were obtained from Sigma–Aldrich (St. Louis, MO, USA) unless otherwise indicated.

2.2. Animals and Drug Administration. Animal experiments were approved by the Committee on the Use of Live Animals in Teaching and Research of the University of Hong Kong (CULATR 4284-17). Male C57BL/6N mice (7-8 weeks, 18–25 g) were provided by the Centre for Comparative Medicine Research, the University of Hong Kong. Animals were housed on a 12 h light–dark cycle and allowed to freely access food and water at the animal facility, the University of Hong Kong. For the behavioral experiments, puerarin was dissolved in saline containing 50% 1,2-propylene glycol. LPS was dissolved in the saline. Mice were randomly separated into 5 groups ($n = 5$): control, LPS, LPS+puerarin (30 mg/kg), LPS+puerarin (60 mg/kg), and LPS+puerarin (120 mg/kg). As outlined in Figure 1(b), following intragastric administration of puerarin for 24 h, mice sequentially received oral gavage of puerarin and intraperitoneal injection of LPS (0.083 mg/kg) with 1 h interval for another 24 h, and the mice in the control group were given the same volume of saline with or without 1,2-propylene glycol. The behavioral tests were performed after LPS treatment.

2.3. Behavioral Tests. Following drug treatment, mice were assessed for depressive behaviors by tail suspension test (TST) and forced swim test (FST) as previously described [23, 26].

For TST, adult mice were immobilized to the suspension bar by attaching the tail with adhesive tape. The distance of 20-25 cm was kept between apparatus floor and mouse nose. During the test over 6 min, a blinded observer recorded the immobility time of the mice.

For FST, adult mice were transferred into a plastic cylinder (30 cm high, 20 cm diameter) filling water at 22 ± 2°C to

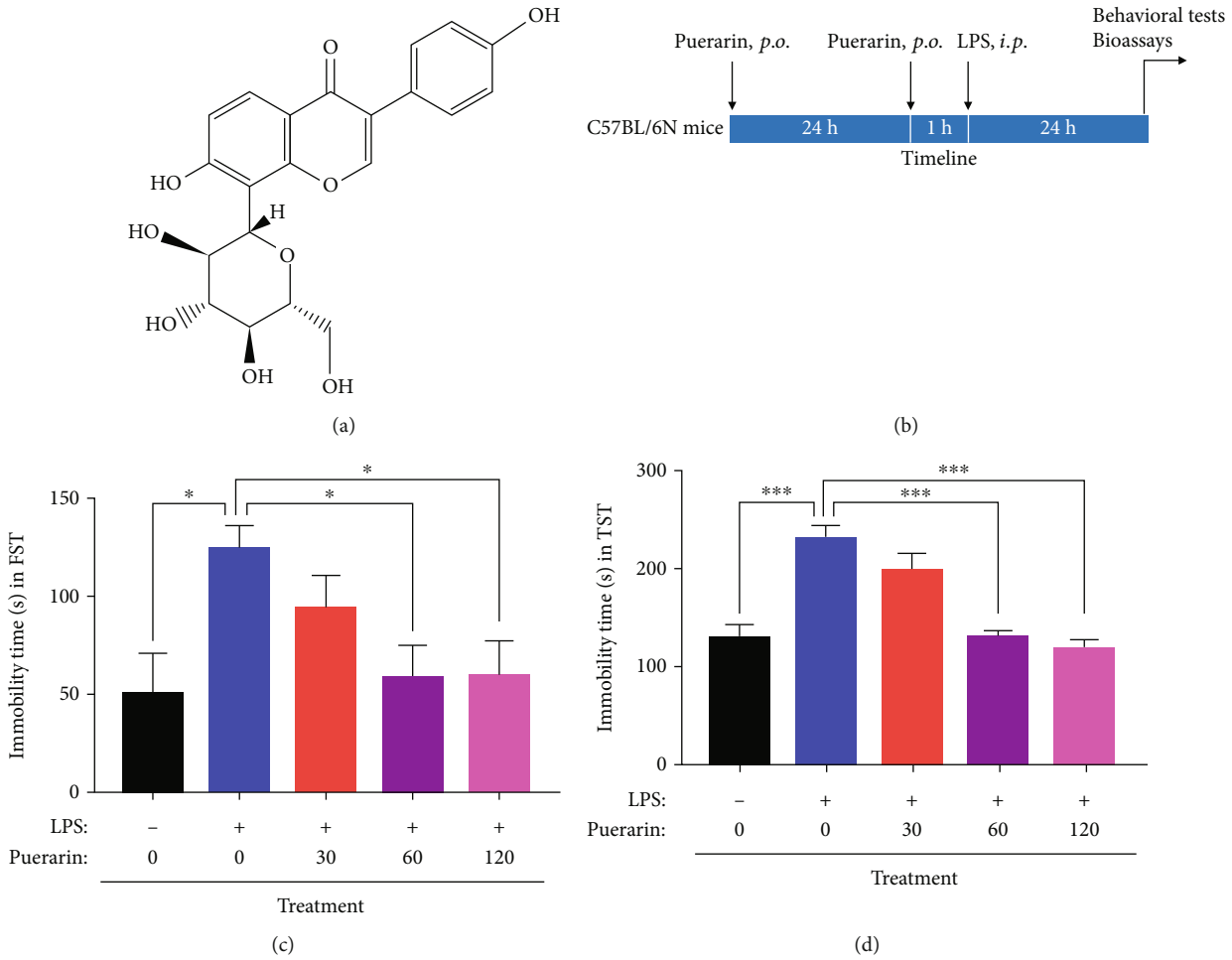

Figure 1: Puerarin ameliorated depressive-like behaviors in the LPS-challenged mice. (a) The chemical structure of puerarin was shown. (b) The design of the animal experiments. Mice were separated into 5 groups: control, LPS, and LPS+puerarin (30, 60, or 120 mg/kg). After drug treatment, mice were assessed for depressive-like behaviours, and brain tissue was collected for the bioassays. (c) Forced swim test (FST). The depressive-like behaviors of mice were evaluated by measuring immobility time during 4 min. (d) Tail suspension test (TST). The depressive-like behaviors of mice were evaluated by measuring immobility time during 6 min. The data were presented as means ± SEM ($n = 6$). $^{*}p < 0.05$; $^{**}p < 0.01$; $^{***}p < 0.001$.

the height of 15 cm. Following 2 min habituation sessions, the immobility time was recorded by a blinded observer during the last 4 min.

2.4. Transcriptome Profiling by Next-Generation RNA Sequencing. Following the behavioral tests, the 3 mm frontal cortex was collected from the mouse brains ($n = 3$). The RNAs were extracted with TRIzol reagent from Thermo Fisher Scientific (Waltham, MA, USA) and purified with RNeasy plus mini kit from QIAGEN (Valencia, CA, USA). Following reverse transcription, the cDNA libraries were sequenced on the Illumina HiSeq 4000 System in BGI (Shenzhen, China). The bioinformatic analyses were performed essentially as previously described [27, 28]. Briefly, the sequence reads were mapped to the mouse grcm38_snp_tran reference sequence with HTSAT2 [29]. Ballgown was applied for the differential gene expressions [30]. The differential genes were selected based on p value of <0.05 and fold change (FC) of ≥2. R was used to make the heatmap. The network of the differential genes was established by Cytoscape (https://cytoscape.org/). The differential genes were analyzed with the Kyoto Encyclopedia of Genes and Genomes (KEGG) pathway and the enriched Gene Ontology (GO) by DAVID 6.8 (http://david.ncifcrf.gov). The p values less than 0.05 indicated that the differential genes were significantly enriched [31].

2.5. Molecular Cloning. RagA cDNA was prepared by polymerase chain reaction (PCR) amplification by using the forward primer (5′-GTACAAGCTTCAGGTGATGCCCAA TACA-3′) and the reverse primer (5′-GTACGATATCG GCATTATTTCAACGCATGA-3′). PCR amplification was conducted in 50 μl reaction mixture containing 10 μl of 5X HF buffer, 2 μl of 50 mM MgCl2, 1 μl of 25 mM dNTPs mix, 2.5 μl each of 20 μM reverse and forward primers, 100 ng of template DNA, and 0.5 μl of Phusion DNA polymerase (5 U/μl, NEB, USA) in a programmable Eppendorf Thermocycler (Hong Kong, China). PCR reaction was programmed as follows: an initial denaturation of 30 seconds

at 98°C, 35 cycles of 98°C for 10 seconds, 57°C for 30 seconds, and 72°C for 1 min, with a final extension at 72°C for 10 min. PCR product was purified from gel by the gel extraction kit (QIAGEN, USA). After the cleavage with HindIII and EcoRV, RagA PCR product was purified and ligated into mammalian expression vector pcDNA 3.1(+) from Invitrogen (Carlsbad, CA, USA). Following transformation and selection, pcDNA 3.1-RagA plasmid DNA was prepared in DH5α *E. coli* cells and purified with QIAGEN Plasmid Miniprep kit (Valencia, CA, USA). The clones were sequenced through Sanger DNA Sequencing Facility at BGI, Shenzhen, China.

2.6. Neural Stem Cell (NSC) Culture. Cortical NSCs were produced from C57BL/6N mouse embryos on embryonic day 14 as previously described [32, 33]. The NSCs were plated in a 90 mm dish at the density of 1×10^5 cells/ml and cultured in DMEM/F12 medium supplemented with 2% B27, 1% N2, 20 ng/ml bFGF, 20 ng/ml EGF, and 1% streptomycin and penicillin at 37°C for 5-7 days. The single cell suspension of NSCs was seeded in the 6-well plates coated with poly-D-lysine for 24 h and treated with 200 ng/ml LPS with or without puerarin at the doses of 10, 25, and 50 μM for 24 h.

2.7. Highly Differentiated PC12 Cell Culture and Transfection. Highly differentiated PC12 cell line was obtained from National Collection of Authenticated Cell Cultures (Shanghai, China). The cells were cultured in DMEM supplemented with 10% HS, 5% FBS, 1% penicillin and streptomycin at 37°C, and 5% CO_2. For the transfection, the cells were seeded in the 6-well plates at the density of 1.5×10^5 cells/ml for 24 h. The pcDNA3.1(+) vector or pcDNA3.1(+)-RagA plasmid was transfected into the cells by using Effectene Transfection Reagent from QIAGEN (Valencia, CA, USA) for 24 h.

2.8. Western Blot Analysis. The frontal cortex tissues or primary mouse neural stem cells were lysed in RIPA buffer for 30 min. The cellular proteins (30 μg) or brain tissue proteins (70 μg) were separated by 10% SDS-polyacrylamide gels. The PVDF membranes were blocked in the 5% BSA in Tris-buffered saline and 0.1% Tween-20 buffer overnight at 4°C. Blots were incubated with primary antibodies overnight and secondary antibodies for 3 h. Subsequently, blots were detected with Amersham™ ECL™ Select Western blotting detection reagents from GE Healthcare (Uppsala, Sweden) [34].

2.9. Immunostaining. After the behavioral tests, a mixture solution of ketamine/xylazine was used for the mice anesthesia, and 4% paraformaldehyde (PFA) in 0.01 M phosphate-buffered saline (PBS) was used for the perfusion. 4% PFA was used to fix the mouse brains overnight at 4°C. The thickness of the coronal sections of the 3 mm frontal cortex was 40 μm. NeuN and RagA primary antibodies were used to probe the tissues overnight at 4°C. The tissues were then incubated with secondary antibodies including Alexa Fluor 488-conjugated goat anti-mouse IgG and Alexa Fluor 594-conjugated goat anti-rabbit IgG for 2 h at room temperature (RT). 4′-6-Diamidino-2-phenylindole (DAPI) was used to stain the cell nucleus. The slides were examined under a Zeiss LSM 700 confocal microscopy (Jena, Germany). The images were analysed by NIH ImageJ software (http://imagej.net/ImageJ2) [23].

For cell culture, the NSCs were treated with 200 ng/ml LPS with or without puerarin at the doses of 10, 25, and 50 μM for 24 h and fixed with 4% PFA. Blocking was performed in 5% normal goat serum for 2 h at RT. The NSCs were sequentially incubated with primary antibodies against mTOR and LAMP2 (FITC) overnight at 4°C and Alexa Fluor 594 goat anti-rabbit IgG secondary antibody for 2 h at RT. DAPI was used to stain the cell nucleus. The slides were examined under a Carl Zeiss fluorescence microscopy (Jena, Germany) [8].

2.10. Quantitative Real-Time PCR (qRT-PCR). The mouse frontal cortex tissues and highly differentiated PC12 cells were analysed for gene expression by qRT-PCR technique as previously described [35]. Briefly, total RNAs were extracted from the frontal cortex tissues and highly differentiated PC12 cells with TRIzol reagent from Thermo Fisher Scientific (Waltham, MA, USA). The cDNAs were prepared from total RNAs with RevertAid RT Reverse Transcription kit from Thermo Fisher Scientific (Waltham, MA, USA). PCR detection was performed with a SYBR Green PCR kit from QIAGEN (Valencia, CA, USA) and Vazyme (Nanjing, China). The primers for various mouse genes were obtained from QIAGEN as follows: RagA (Mm_Rraga_1_SG; QT00257880), FZD1 (Mm_Fzd1_1_SG; QT00290542), Fitm2 (Mm_Fitm2_1_SG; QT00147903), Camkk2 (Mm_Camkk2_1_SG; QT00162449), Ap3S2 (Mm_Ap3s2_1_SG; QT00148428), Mesdc1(Mm_Mesdc1_1_SG; QT00292187), GAPDH (Mm_Gapdh_3_SG; QT01658692), and β-actin (Mm_Actb_1_SG; QT 00095242). The primers for rat genes were as follows: RagA (NM_053973), F: 5′-GGAACCTGG TGCTGAACCTGTG-3′, R: 5′-GGATGGCTTCCAGACA CGACTG-3′; IL-6 (NM_012589), F: 5′-GCCCACCAGGA ACGAAAGTCAA-3′, R: 5′-GGAAGGCAGTGGCTGT CAACAA-3′; IL-1β (NM_031512), F: 5′-AATGCCTCGTG CTGTCTGACC-3′, R: 5′-GTGGGTGTGCCGTCTTTCA TCA-3′; β-actin (NM_031144), F: 5′-GTATGCCTCTGGTC GTACCA-3′, R: 5-CTCTCAGCTGTGGTGGTGAA-3′. The data were normalized to β-actin or GAPDH. The relative expression level of genes was indicated by $2 - \Delta\Delta Ct$.

2.11. Statistical Analysis. The data were presented as mean ± SEM for body weight, behavioral experiments, and qRT-PCR in the animal experiments and mean ± SD for other experiments. The comparisons of multiple groups were performed using one-way analysis of variance (ANOVA) followed by Dunnett's test. GraphPad Prism 7 (La Jolla, CA, USA) was used to analyze the data. The p values of less than 0.05 were regarded as statistically significant.

3. Results

3.1. Puerarin Attenuated the Depressive-like Behaviors in LPS-Challenged Mice. FST and TST were used to assess the

effect of puerarin on the depressive behaviors in LPS-challenged mice as previously described [23]. As outlined in Figure 1(b), C57BL/6N mice were administered with LPS or in combination with puerarin. The results of FST and TST were shown in Figures 1(c) and 1(d), respectively. Indeed, compared with the control group, LPS markedly prolonged the immobility time of mice in the FST and TST. Puerarin (60 and 120 mg/kg) significantly reduced the immobility time in LPS-treated mice in FST and TST compared with LPS alone group while such drug (30 mg/kg) did not exhibit evident activities.

3.2. Puerarin Affected RagA and Other 15 Genes in LPS-Treated Mice. To discover the antidepressant mechanisms for puerarin, the mouse frontal cortex tissues were collected from control, LPS, and LPS+P groups and profiled by next-generation RNA sequencing technology. As shown in Figures 2(a) and 2(b), a total of 16 differentiated genes with $p < 0.05$ and FC ≥ 2 were identified based on the comparison groups: LPS vs. control and LPS+P vs. LPS. In particular, 10 genes were upregulated while 6 genes were downregulated in the comparison of LPS+P group vs. LPS group. Puerarin downregulated the level of RagA expression to the largest extent (FC = 0.02) based on RagA expression in LPS+P group and LPS group. The interaction network was created by including 16 differentiated genes and 7 closely related genes although no significant change was detected. The selected genes were enriched by GO and KEGG pathways. As shown in Figure 2(c), activate transcription factor (GO:0051091), Wnt-activated receptor (GO:0042813), and frizzled binding (GO:0005109) were the most significantly enriched in the GO terms "biological process" and "molecular function." Wnt-signaling pathway was the most significantly enriched KEGG pathway (KEGG: mmu04310).

3.3. Puerarin Effectively Downregulated RagA in LPS-Challenged Mice. To verify the results of RNA sequencing, six representative genes (i.e., RagA, FZD1, Fitm2, Camkk2, Ap3S2, and Mesdc1) were validated by qPCR technique. As shown in Figure 3(a), the brain tissues from LPS group resulted in higher mRNA levels of RagA, FZD1, and Fitm2. Puerarin (60 mg/kg) significantly decreased the mRNA levels of these genes against LPS stimulation. RagA was further verified by Western blotting and immunostaining. As shown in Figures 3(b) and 3(c), LPS significantly enhanced the protein levels of RagA whereas puerarin (60 mg/kg) significantly reduced RagA expression in LPS-treated mice. Puerarin group showed the lower level of RagA expression compared with control group. As shown in Figures 3(d) and 3(e), LPS significantly enhanced the immunofluorescence staining of RagA expression whereas puerarin (60 mg/kg) significantly decreased the immunofluorescence intensity for RagA staining against LPS stimulation. Moreover, after LPS treatment, RagA and NeuN appeared to be colocalized in the frontal cortex of mice.

3.4. Puerarin Inhibited the Activation of RagA/mTOR/p70S6K Pathway and the Lysosomal Translocation of mTORC1 in Neural Stem Cells. To determine the mechanisms by which RagA mediates the activity of puerarin, we focused on RagA-associated mTOR signaling pathway. For the effects of puerarin on the RagA/mTOR/p70S6K pathway, as shown in Figures 4(a) and 4(b), LPS treatment enhanced the protein expression of RagA, phospho-mTOR and phospho-p70S6K in neural stem cells. Puerarin (50 μM) significantly decreased RagA expression against LPS stimulation. Moreover, puerarin (25 and 50 μM) significantly decreased the expression of phospho-mTOR and phospho-p70S6K against LPS stimulation. For the effects of puerarin on the lysosomal translocation of mTORC1, as shown in Figures 4(c) and 4(d), LPS enhanced the expression of lysosomal biomarker LAMP2 and promoted the colocalization of mTOR and LAMP2 in the nucleus. Puerarin reduced LPS-induced LAMP2 expression and disturbed the colocalization of mTOR and LAMP2 in a concentration-dependent manner. Puerarin (50 μM) spread the distribution of LAMP2 in the cytosol of neural stem cells against LPS stimulation.

3.5. Puerarin Inhibited LPS-Induced Expression of Proinflammatory Cytokines. To study the role of RagA in the anti-inflammatory activity of puerarin, the effects of puerarin were evaluated on LPS-induced inflammatory responses in mice. Firstly, we clarified whether LPS-induced sickness in mice. After 24 h treatment, we measured the body weight of mice. As shown in Figure 5(a), LPS and puerarin did not obviously change the body weight of mice, suggesting that LPS did not cause sickness in mice. Secondly, we determined whether puerarin could suppress LPS-induced production of proinflammatory cytokines in mice. As shown in Figure 5(b), qRT-PCR analysis validated that LPS markedly induced the mRNA levels of proinflammatory genes including IL-6, IL-1β, and TNF-α. Puerarin effectively reduced the mRNA levels of IL-6 and IL-1β and affected TNF-α to a lesser extent. Thirdly, we examined the effect of ectopic RagA overexpression on cytokine synthesis. The full-length RagA cDNA was cloned in pcDNA3.1 (+) vector and subsequently introduced into highly differentiated PC12 cells. As shown in Figure 5(c), RagA transfection resulted profound increase in the expression of RagA mRNA. The mRNA level of IL-6 but not IL-1β was obviously elevated in RagA-transfected PC12 cells compared with that in pcDNA3.1 vector transfected cells.

4. Discussion

Depressive symptom may be one of the predictive signs for the onset of AD in the elderly population. Inflammation is known to increase the risk of depression in AD patients [36]. Thus, LPS was used to induce acute inflammation and depressive-like behaviors in mice [37]. Indeed, we recently found that LPS could cause the depressive-like behaviors in mice via activating RagA/mTOR/p70S6K pathway [8]. As for the therapy of depression, the conventional antidepressant drugs are challenged by gastrointestinal and sexual side effects [38, 39]. Interestingly, we recently discovered that botanical drug puerarin could effectively attenuate depression and pain in mice with SNI [23]. Based on the side-by-side comparison with the clinical drugs, puerarin

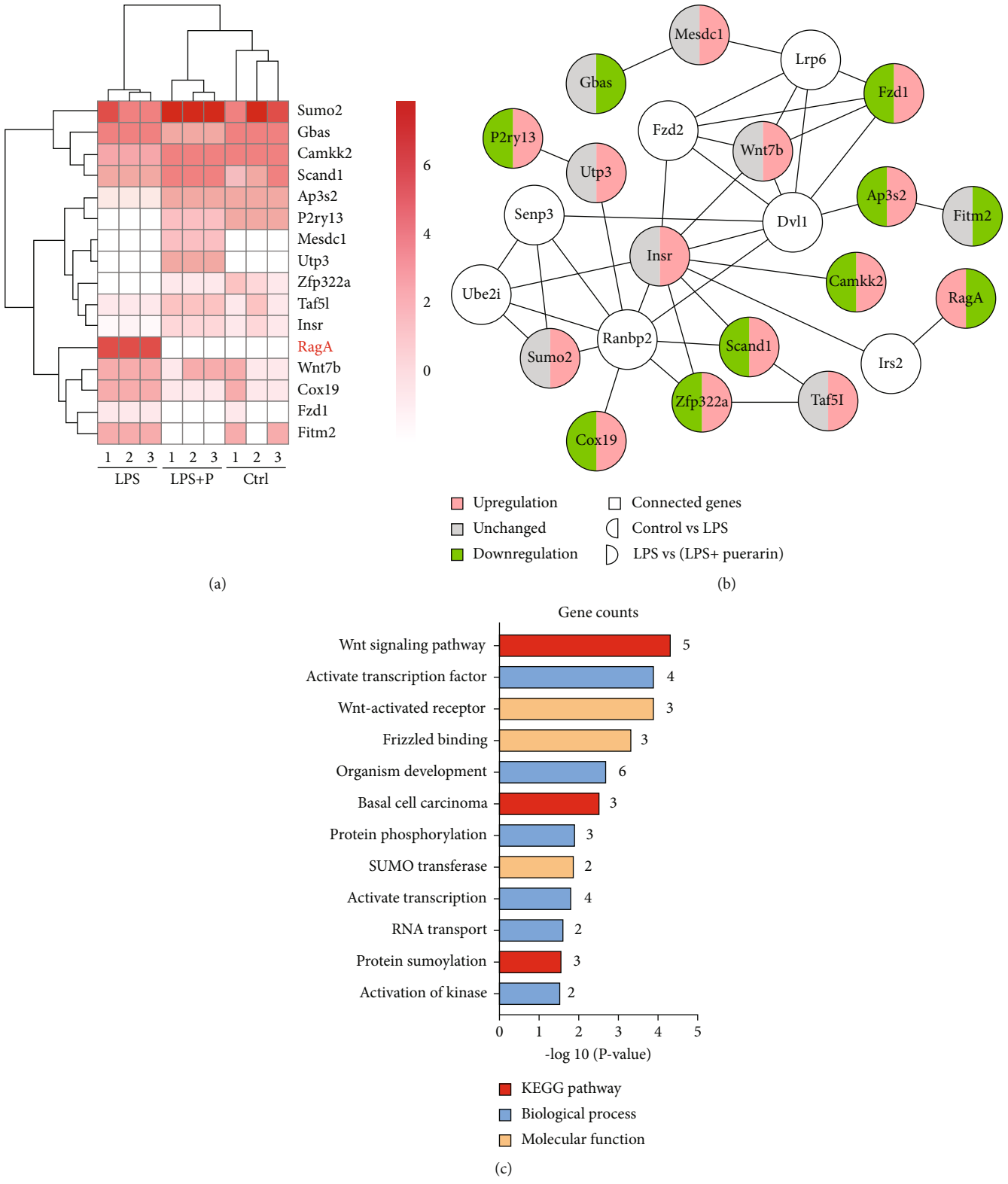

Figure 2: Puerarin significantly affected 16 differentiated genes in LPS-challenged mice. (a) Heatmap of differentially expressed genes. The frontal cortex tissues were collected from 3 groups of mice (i.e., control, LPS, and LPS+puerarin (60 mg/kg), $n = 3$) and profiled by next-generation RNA sequencing technology. The differentially expressed genes were identified by RNA sequencing and bioinformatics analysis. The heatmap of 16 differentially expressed genes was visualized with R language. (b) Interaction network of differentially expressed genes. The interaction network of 16 differentially expressed genes and 7 unchanged genes was generated by Cytoscape. The downregulated genes were described as green whereas the upregulated genes were described as red. (c) GO and KEGG pathway analysis of differentially expressed genes. Sixteen differentially expressed genes were analysed for GO and KEGG pathway by DAVID 6.8.

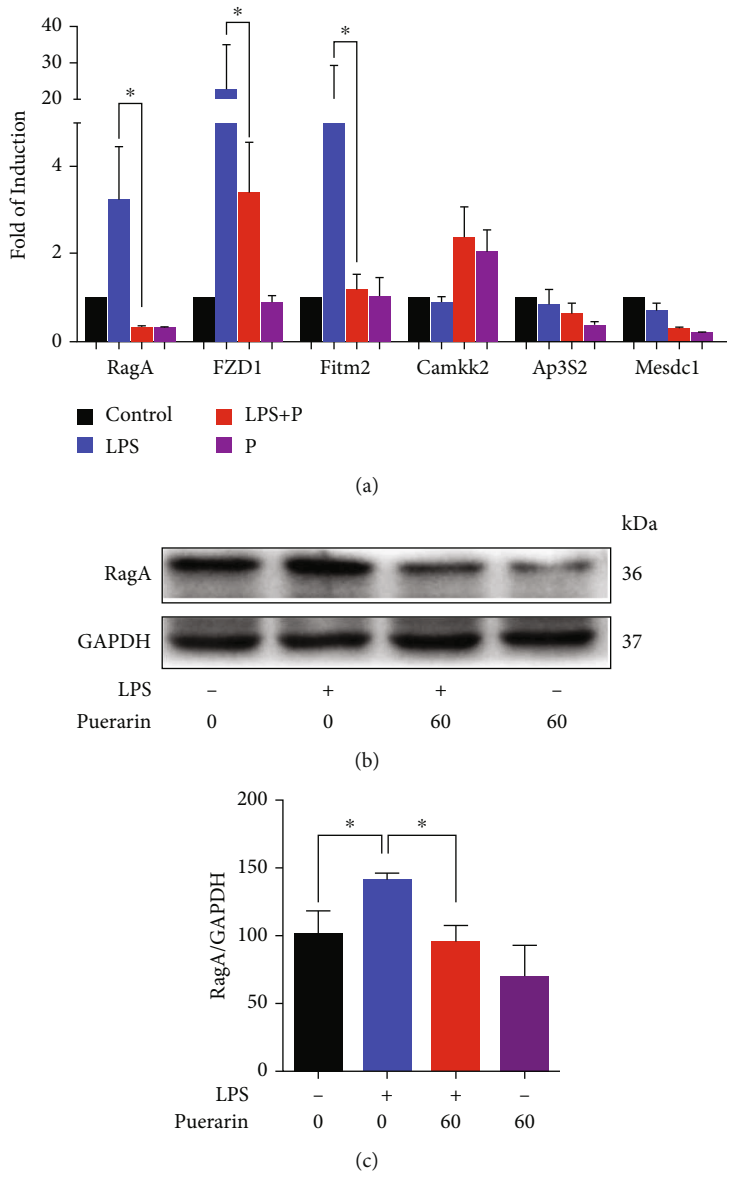

Figure 3: Continued.

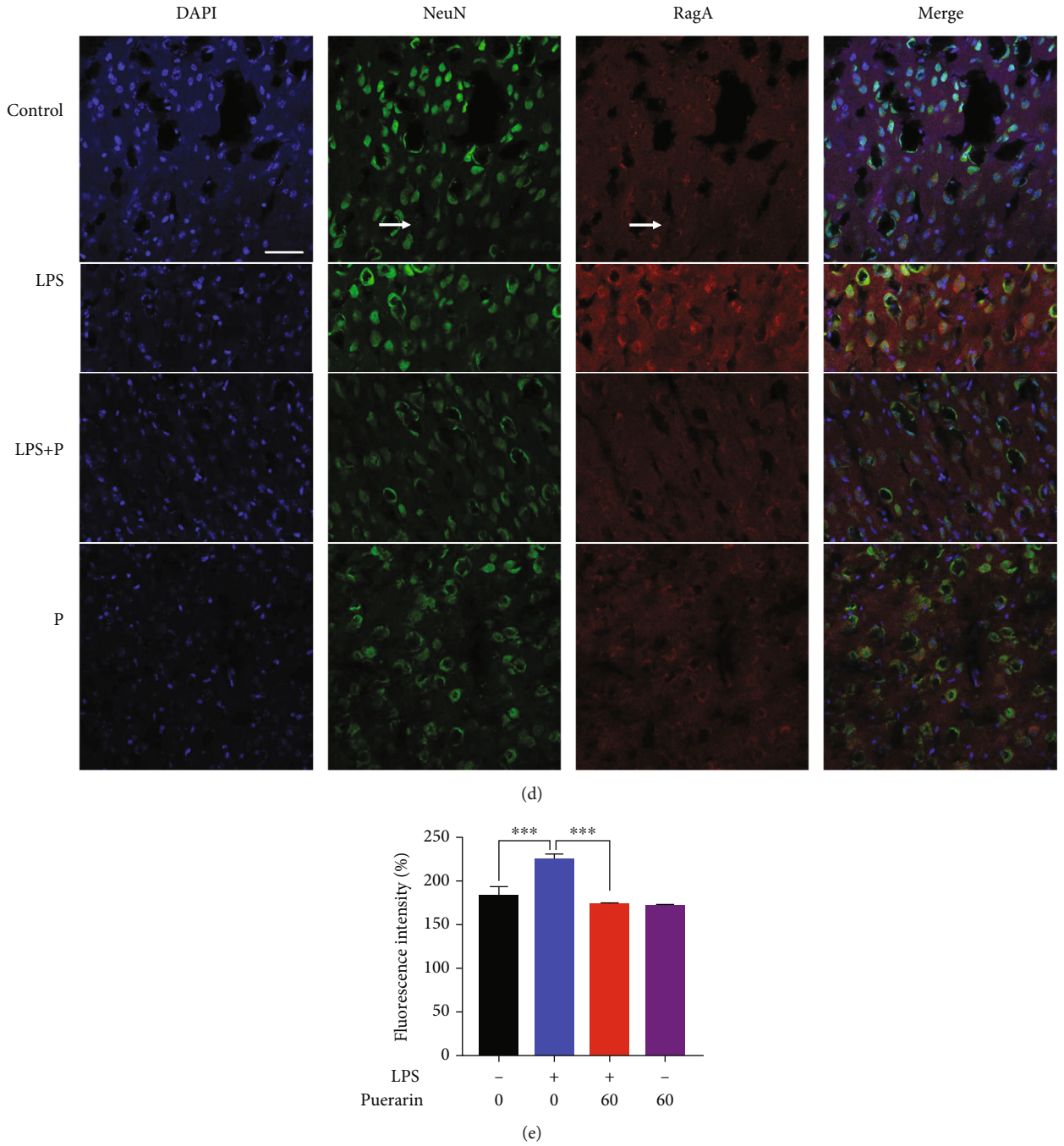

Figure 3: Puerarin downregulated RagA expression in LPS-challenged mice. (a) qRT-PCR quantification of 6 representative differentially expressed genes. The frontal cortex tissues were collected from 4 groups of mice (i.e., control, LPS, LPS+puerarin (60 mg/kg), and puerarin (60 mg/kg), $n = 3$) and analysed by qPCR for selected genes. The data were presented as means ± SEM ($n = 3$). $^{*}p < 0.05$. (b) Western blot analysis of the protein expression of RagA. The frontal cortex tissues were collected from the experimental mice ($n = 3$) for Western blot analysis of RagA. (c) Quantification of RagA expression. The blots were detected by a densitometric method ($n = 3$). $^{*}p < 0.05$. (d) Immunofluorescence detection of RagA expression in the frontal cortex. The frontal cortex tissues were collected from the experimental mice ($n = 3$) for immunohistochemical analysis for RagA expression, whereas DAPI was used to stain nuclear. NeuN was detected as the biomarker for the mature neurons. The images were captured with a Carl Zeiss 700 confocal fluorescence microscope (Jena, Germany). Scale bar, 50 μm. (e) Quantification of RagA expression. Fluorescence intensity of RagA in (d) was evaluated through the densitometric method ($n = 3$). $^{***}p < 0.001$.

and citalopram achieved similar effects on the depressive behaviors and pain in mice whereas ibuprofen appeared to be less effective. In fact, others also evaluated the antidepressant effects of puerarin in the other animal models [40]. In this study, we firstly validated that puerarin could attenuate the LPS-induced depressive-like behaviors in mice

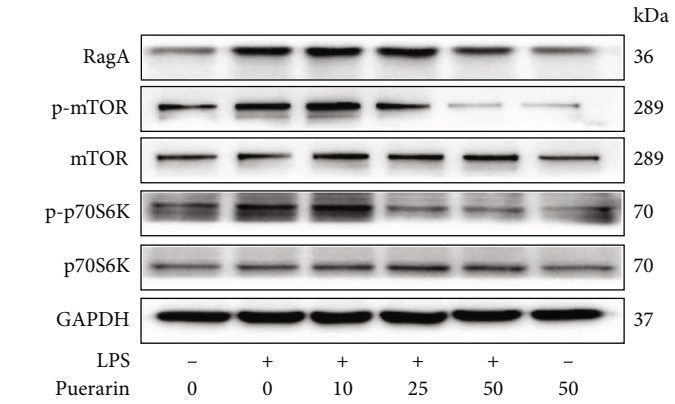

(a)

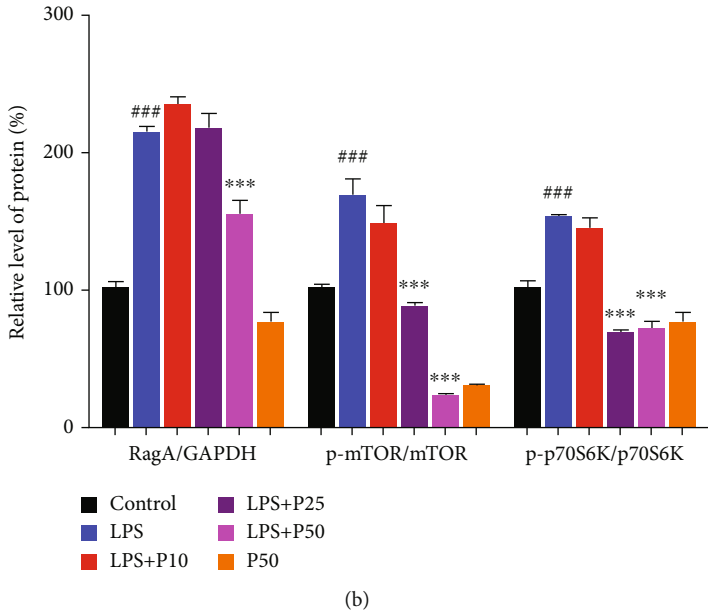

(b)

Figure 4: Continued.

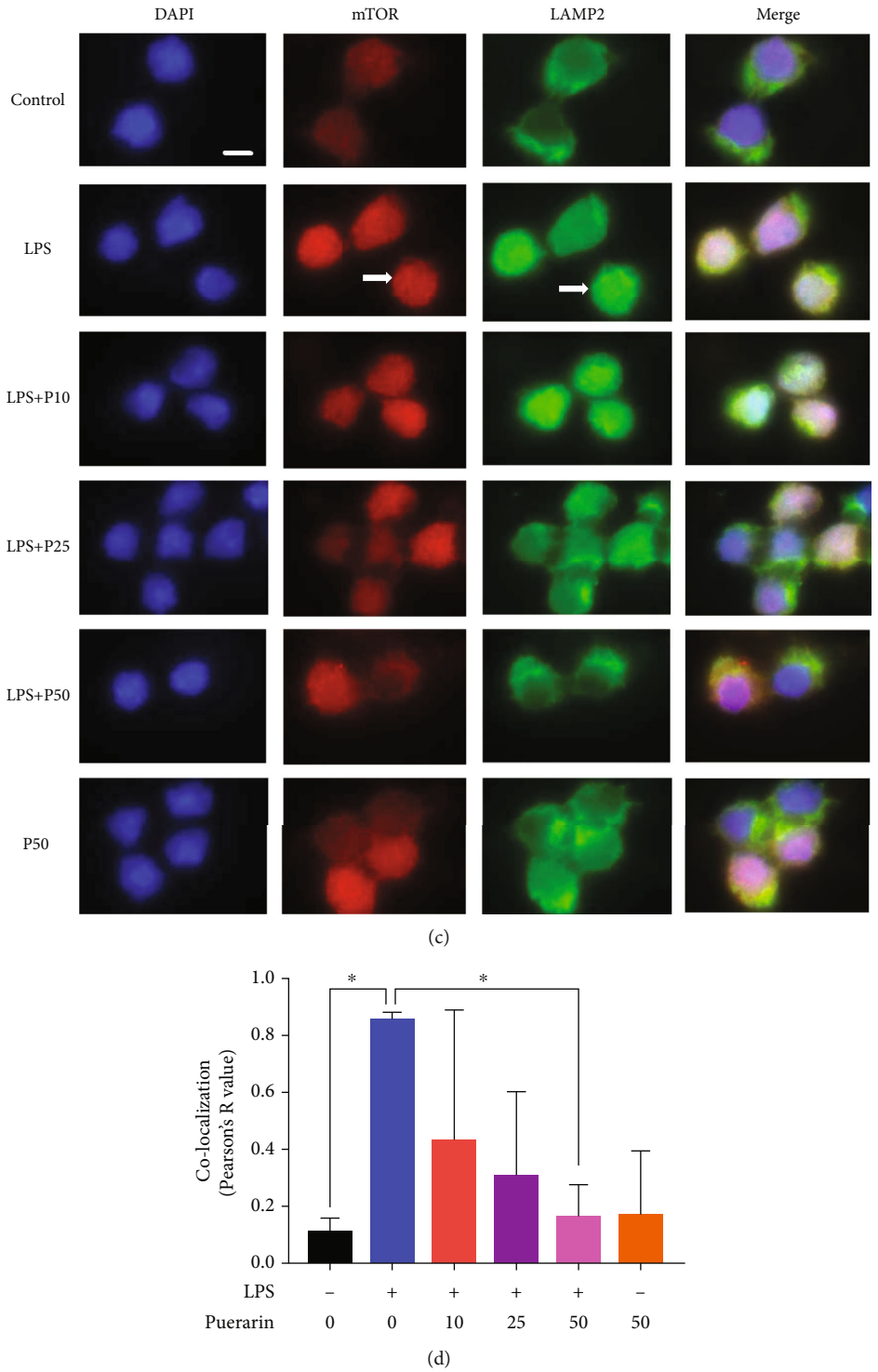

Figure 4: Puerarin inhibited the RagA/mTOR/p70S6K pathway and the lysosomal localization of mTORC1 in the NSCs. (a) Detection of RagA, mTOR, and p70S6K. The protein expression of RagA, mTOR, and p70S6K were analyzed by Western blot in LPS-challenged neural stem cells. After 24 h treatment with 200 ng/ml LPS alone or in combination with puerarin (P) (10, 25, and 50 μM), NSCs were analyzed by Western blot for the protein expression of RagA, phospho-mTOR (p-mTOR), mTOR, phospho-p70S6K (p-p70S6K), and p70S6K. (b) Quantitation of the blots in (a). The blots in (a) were quantified by the densitometric method. The protein value was shown as means ± SD ($n = 3$). $^{\#\#\#}$ $p < 0.001$ (LPS vs. control); $^{***}p < 0.001$ (LPS+P vs. LPS). (c) Immunofluorescence staining of mTORC1 in LPS-stimulated neural stem cells. After 24 h treatment with 200 ng/ml LPS or in combination with P (10, 25, and 50 μM), NSCs were incubated with mTOR and lysosomal biomarker LAMP2 antibodies, and DAPI was used to stain nuclear. The images were captured with a Zeiss fluorescence microscope (Jena, Germany). Scale bar, 20 μm. (d) Quantification of mTOR and LAMP2. Colocalization of mTOR and LAMP2 was quantified by Pearson's R value. The results were shown as means ± SD ($n = 3$). $^{*}p < 0.05$.

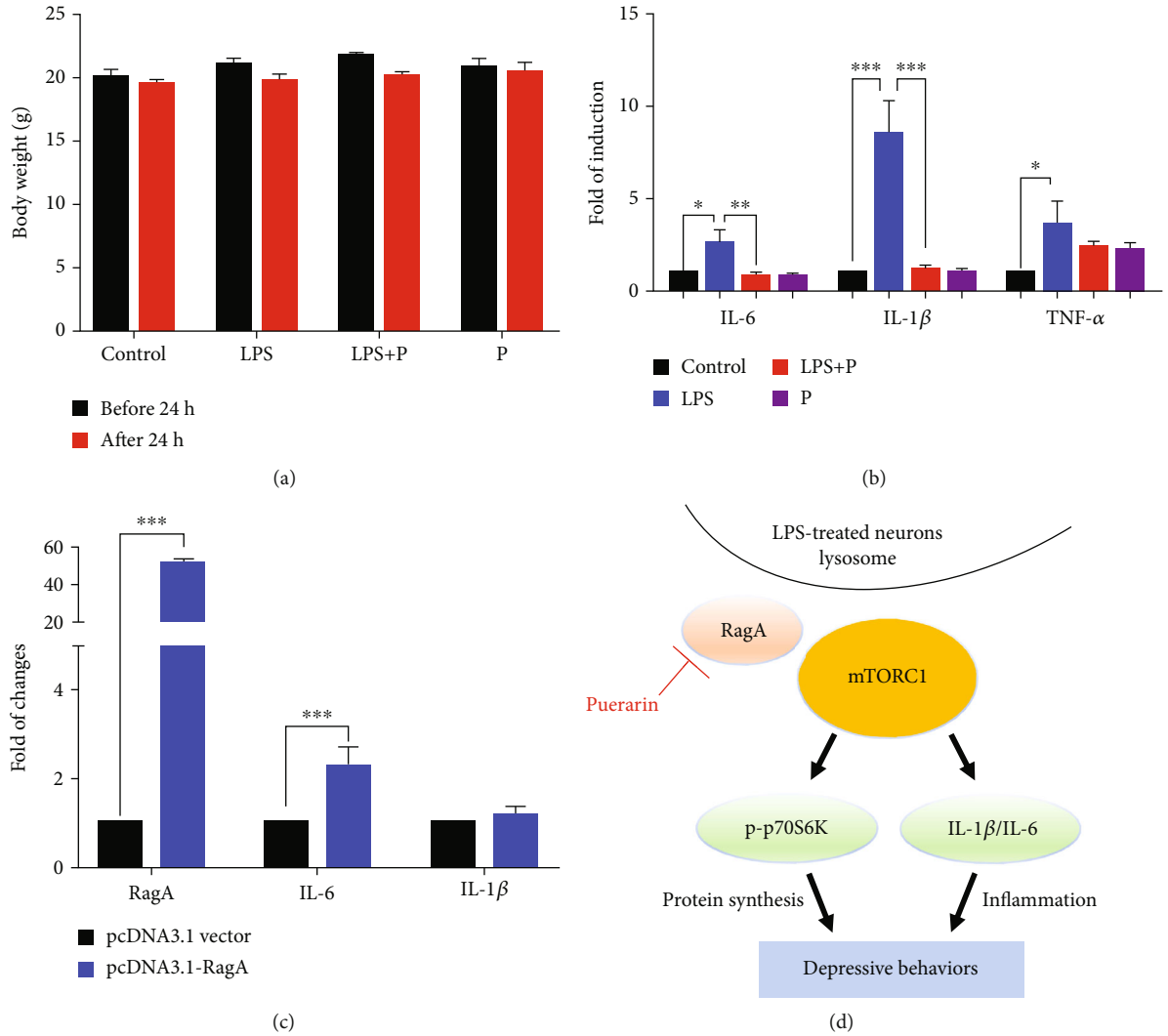

FIGURE 5: Puerarin attenuated the expression of inflammatory cytokines against LPS stimulation. (a) Body weight of experimental mice. The body weight of the mice in the indicated groups was measured before and after LPS treatment. (b) qRT-PCR quantification of representative inflammatory cytokines. The frontal cortex tissues were collected from 4 groups of mice (i.e., control, LPS, and LPS+puerarin (60 mg/kg), puerarin (60 mg/kg), $n = 3$) and analysed by qPCR analysis. The results were shown as means ± SEM ($n = 3$). $^{*}p < 0.05$; $^{**}p < 0.01$; $^{***}p < 0.001$. (c) qRT-PCR quantification of RagA, IL-6, and IL-1β. Highly differentiated PC12 cells were transfected with pcDNA3.1 vector or pcDNA3.1-RagA plasmid for 24 h. The cells were collected for qPCR analysis. The data were shown as means ± SD ($n = 3$). $^{***}p < 0.001$. (d) The diagram illustrating the potential mechanism. Puerarin targeted RagA and thereby inhibited the mTOR/p70S6K pathway and suppressed the mRNA levels of proinflammatory cytokines (e.g., IL-6 and IL-1β) towards the amelioration of depressive behaviors.

(Figures 1(c) and 1(d)). Subsequently, we focused on the molecular mechanisms underlying the antidepressant activity of puerarin. Our strategy was to identify differentially expressed genes in mice after treatment with LPS and puerarin, alone or in combination, by next-generation RNA sequencing technology. Indeed, we found that puerarin downregulated the expression of RagA mRNA by 60 folds compared with LPS-stimulated group. We further investigated the effects of puerarin on RagA/mTOR/p70S6K pathway, the accumulation of mTORC1 at the lysosomal membrane, and the production of proinflammatory cytokines.

Next-generation RNA sequencing technology is widely used to profile the transcriptomes of cultured cells and animal models for differentially expressed genes [41]. In our study, adult male mice were randomly divided into four groups: control, LPS, LPS+Puearin, and puearin. RNA sequencing profiles revealed that puerarin affected RagA and other 15 genes against LPS stimulation (Figures 2(a) and 2(b)). The functional annotation classified these genes into multicellular organism development, small ubiquitin-like modifier (SUMO) transferase activity, activation of protein kinase activity, DNA-binding transcription factor activity, protein heterodimerization activity, and other activities (Figure 2(c)). As for multicellular organism development, puerarin upregulated small subunit processome component (Utp3) and downregulated Wnt family member 7B (Wnt7b) and frizzled class receptor 1 (Fzd1). Utp3 is involved in the

development of the osteosarcoma through regulating the ribosome biogenesis [42]. Wnt7b is a key ligand for the Wnt signaling pathway and mainly regulates the angiogenesis in the brain and spinal cord [43]. Fzd1 is a receptor for the Wnt signaling and regulates the adult hippocampal neurogenesis [44]. For SUMO transferase activity, puerarin upregulated the isoform Sumo2. Sumo2 is directly involved in the protein sumoylation for controlling the cognitive process in mice [45]. For the activation of protein kinase activity, puerarin upregulated insulin receptor (Insr) and calcium/calmodulin-dependent protein kinase kinase 2 (Camkk2). Insr refers to a tyrosine kinase receptor and transmitted the ligands of insulin to bind to the intracellular signaling [46]. Insr manifested as isoform A and isoform B. Insr-A was mainly expressed in the brain and uniquely expressed in the neuron. Insr-B was mainly expressed in the peripheral tissue [47]. Insr is upregulated in the entorhinal cortex and hippocampus in patients with Alzheimer's disease compared with elderly control group [48]. Camkk2 is characterized as a protein kinase for regulating cell survival and proliferation [49]. Camkk2 could decrease the expression of proinflammatory cytokines and promote LPS-treated primary microglial cells to undergo M2 polarization [50]. For protein transporter activity, puerarin upregulated adaptor-related protein complex 3 subunit sigma 2 (AP3S2). Previous study identified that some AP3S2 genetic variants are related to the onset of type-2 diabetes [51]. For DNA-binding transcription factor activity, puerarin upregulated SCAN domain containing 1 (Scand1), TATA-box-binding protein-associated factor 5 like (Taf5l), and zinc finger protein 322 (Zfp322a). Scand1 is suggested to be a potential druggable target in the treatment of anxiety disorder [52]. Scand1 is upregulated by carbon monoxide in the cortical astrocytes [53]. Taf5l is a component of the P300/CBP-associated factor (PCAF) complex with the activity to acetylate the histones [54]. Another study showed that Taf5l is an epigenetic regulator for mediating the mouse embryonic stem cell state [55]. Zfp322a regulates the pluripotency of the mouse embryonic stem cells and increases the reprogramming efficiency [56]. For protein heterodimerization activity, puerarin downregulated small GTPase RagA. RagA senses amino acids for the mTORC1 signaling pathway involving in cell growth and metabolism [14]. For other activities, puerarin downregulated cytochrome c oxidase 19 (Cox19), fat storage-inducing transmembrane protein 2 (Fitm2), and glioblastoma amplified sequence (Gbas). Cox19 is involved in the copper efflux to the mitochondria [57]. Fitm2 regulates in the normal fat storage in adipose tissues in mice and plays critical role in the cell homeostasis and the locomotor functions [58]. Gbas was expressed in the brain and heart to regulate the CREB signaling pathway, Ca^{2+} influx, and vesicular transport [59]. On the other hand, puerarin upregulated mesoderm development candidate 1 (Mesdc1) and purinergic receptor P2Y13 (P2ry13). Mesdc1 is an actin-binding protein and has an oncogenicity in the bladder cancer and hepatocellular carcinoma [60]. P2ry13 is mainly expressed in the microglia, not neuron or astrocyte. Interestingly, P2ry13 disruption enhances the proliferation of progenitor cells and the formation of new neurons [61]. Based on the gene abundance, fold changes and biological relevance, RagA was selected for further study in current study.

Our group recently revealed that LPS markedly upregulated RagA expression and activated mTORC1 pathway [8]. RagA forms heterodimers with other isoforms for different functions, for example, RagA/RagB heterodimer for binding GTP and RagC/RagD heterodimer for binding GDP [62]. Importantly, RagA senses the cellular sufficiency of amino acids for the mTOR signaling pathway [63]. When amino acids are deficient, the inactive heterodimer (RagA/B) recruits the trimeric tuberous sclerosis complex (TSC) to the lysosome, thereby preventing the association with mTORC1 activator Ras-homolog accumulated in brain (Rheb) [64]. When the amino acids are sufficient, however, heterodimer RagA/B is loaded with GTP to bind the regulatory-associated protein of mammalian target of rapamycin (Raptor), recruit mTORC1 to the lysosome surface to form complex with Rheb and activate mTORC1 [65]. The effect of mTORC1 signaling pathway is the regulation of cell growth and metabolism while dysregulation of mTORC1 is implicated in the neurodegenerative diseases, cancer, and diabetes [66]. The phosphorylation of the downstream targets including p70S6K and 4EBP1 exhibit the activity of mTORC1 [67]. Phosphorylated p70S6K promotes the protein synthesis. Phosphorylated 4EBP1 does not bind to the eukaryotic translation initiation factor 4E (EIF4E), which promotes the cap-dependent mRNA translation [68]. The p70S6K signaling pathway is a potential mechanism mediating the major depressive disorder [69]. High-fat diet caused the anxiety and anhedonia via reducing the expression of phospho-P70S6K in the frontal cortex of rats [70]. In the present study, RagA, FZD1, Fitm2, Camkk2, Ap3S2, and Mesdc1 were selected for qPCR validation. LPS increased the mRNA levels of RagA, FZD1, and Fitm2 compared with the control group. Puerarin at the dosage of 60 mg/kg significantly reduced the expression of mRNA levels of RagA, FZD1, and Fitm2 against LPS stimulation although the mRNA levels of Camkk2, Ap3S2, and Mesdc1 remained unchanged (Figure 3(a)). Puerarin effectively reduced RagA in LPS-challenged mice (Figures 3(b)–3(e)). Such results appeared to be consistent with the results of RNA-seq profiling. Neurogenesis is implicated in the depression [71]. Our previous study demonstrated that LPS activated the RagA/mTOR/p70S6K pathway and caused the lysosomal accumulation of mTORC1 in the NSCs [8]. In our study, we validated that puerarin inhibited the RagA/mTOR/p70S6K pathway and reduced the accumulation of mTORC1 lysosomal in neural stem cells (Figures 4(a)–4(d)). Moreover, LPS is well known to induce inflammation in mice [37]. In this study, we firstly confirmed that LPS and puerarin could not cause significant sickness in mice (Figure 5(a)). Such results clarified that depressive behaviors were not resulted from LPS-induced sickness. Secondly, we examined the effects of puerarin on proinflammatory cytokines. Indeed, puerarin effectively reduced corresponding mRNA level of IL-6 and IL-1β and affected TNF-α to a lesser extent in LPS-challenged mice (Figure 5(b)). As for the potential role of RagA in LPS-induced inflammatory response, we examined whether

ectopic expression of RagA could influence the expression of proinflammatory cytokines (e.g., IL-6 and IL-1β). As result, the overexpression of RagA led to the significant increase in IL-6 mRNA levels, but not IL-1β mRNA in highly differentiated PC12 cells (Figure 5(c)). Interestingly, mTORC1 often cross-talks with mTORC2 to regulate the production of different cytokines [72]. Combining mTORC1/mTORC2 with pp242 or high-dose rapamycin upregulated IL-1β and TNF-α but downregulated IL-6 [73]. In addition, the mTORC1 pathway regulated IL-1β by dendritic cells [74]. Presumably, RagA links the mTORC1 signaling pathway to the expression of different proinflammatory cytokines in a cell context specific manner. Taken together, puerarin inhibited the RagA/mTOR/p70S6K pathway and reduced the production of proinflammatory cytokines (e.g., IL-6, IL-1β) against LPS stimulation. Ultimately, puerarin could effectively ameliorate LPS-induced depressive behaviors (Figure 5(d)).

5. Conclusions

The results from the present study not only validated that botanical drug puerarin could attenuate LPS-stimulated depressive-like behaviors in mice but also revealed that the inhibition of RagA/mTOR/p70S6K pathways could be a potential antidepressant mechanism. At the molecular level, puerarin downregulated RagA expression, reduced the lysosomal translocation of mTORC1, and inhibited the activation of mTOR/p70S6K pathway. Consequently, puerarin markedly reduced the expression of proinflammatory cytokines, especially, IL-6, in LPS-challenged mice. Thus, puerarin may be a promising antidepressant and anti-inflammatory candidate drug for the alleviation of depression in AD and other diseases.

Abbreviations

LPS: Liposaccharide
RagA: Ras-related GTP binding protein A
qRT-PCR: Quantitative real-time PCR
AD: Alzheimer's disease
IL: Interleukin
GTPases: Guanosine triphosphatases
mTOR: Mammalian target of rapamycin
GTP: Guanosine triphosphate
GDP: Guanosine diphosphate
LAMP2: Lysosome-associated membrane protein 2
p70S6K: p70 S6 kinase
4E-BP1: 4E-binding protein 1
CUMS: Chronic unpredictable mild stress
DMEM: Dulbecco's modified Eagle's medium
FBS: Fetal bovine serum
HS: Horse serum
bFGF: Basic fibroblast growth factor
EGF: Epidermal growth factor
TST: Tail suspension test
FST: Forced swim test
FC: Fold change
KEGG: Kyoto Encyclopedia of Genes and Genomes
GO: Gene Ontology
PCR: Polymerase chain reaction
NSC: Neural stem cell
PFA: Paraformaldehyde
PBS: Phosphate-buffered saline
RT: Room temperature
DAPI: 4′-6-diamidino-2-phenylindole
ANOVA: One-way analysis of variance
Utp3: Small subunit processome component
Wnt7b: Wnt family member 7B
Fzd1: Frizzled class receptor 1
Sumo2: Small ubiquitin-like modifier 2
Insr: Insulin receptor
Camkk2: Calcium/calmodulin-dependent protein kinase kinase 2
AP3S2: Adaptor-related protein complex 3 subunit sigma 2
Scand1: SCAN domain containing 1
Taf5l: TATA-box-binding protein-associated factor 5 like
Zfp322a: Zinc finger protein 322
PCAF: P300/CBP-associated factor
Cox19: Cytochrome c oxidase 19
Fitm2: Fat storage-inducing transmembrane protein 2
Gbas: Glioblastoma amplified sequence
Mesdc1: Mesoderm development candidate 1
P2ry13: Purinergic receptor P2Y13
TSC: Tuberous sclerosis complex
Rheb: Ras-homolog enriched in brain
Raptor: Regulatory-associated protein of mammalian target of rapamycin
EIF4E: Eukaryotic translation initiation factor 4E.

Data Availability

The data that support the findings of this study were available from the corresponding author upon reasonable request.

Ethical Approval

Animal experiments were approved by the Committee on the Use of Live Animals in Teaching and Research of the University of Hong Kong (CULATR 4284-17).

Conflicts of Interest

The authors demonstrate that there is no conflict of interest.

Authors' Contributions

Jia Zhao, Wei Zhao, Huixin Chen, Xiuying Zhang, and Dan Luo performed the experiments; Yizhen Jia, Fung Yin Ngo, and Youqiang Song analyzed the data of RNA sequencing. Lixing Lao supervised the data analysis; Jianhui Rong designed the research and revised the article.

Acknowledgments

Sincere thanks to Mr. Wong Hei Kiu, Ms. Lee Wai Sin, and Mr. Shek Chun Shum for their professional technical assistance. The computing operation were carried out using research computing facilities offered by Information Technology Services, the University of Hong Kong. This work was supported by National Natural Science Foundation of China (Nos. 21778046 and 81703726), the Health and Medical Research Fund (HMRF 15161731, 16171751, and 17181231), General Research Fund (GRF) grants (17120915, 17146216, 17100317, and 17119619), Research and Cultivation Plan of High-Level Hospital Construction (HKUSZH201902040), Science, Technology and Innovation Commission of Shenzhen Municipality (JCYJ20180306173835901), and Midstream Research Programme for Universities (MRP) 053/18X.

References

[1] V. Orgeta, N. Tabet, R. Nilforooshan, and R. Howard, "Efficacy of antidepressants for depression in Alzheimer's disease: systematic review and meta-analysis," *Journal of Alzheimer's Disease*, vol. 58, no. 3, pp. 725–733, 2017.

[2] M. E. Fox and M. K. Lobo, "The molecular and cellular mechanisms of depression: a focus on reward circuitry," *Molecular Psychiatry*, vol. 24, no. 12, pp. 1798–1815, 2019.

[3] L. Leng, K. Zhuang, Z. Liu et al., "Menin deficiency leads to depressive-like behaviors in mice by modulating astrocyte-mediated neuroinflammation," *Neuron*, vol. 100, no. 3, pp. 551–563.e7, 2018, e7.

[4] M. L. Wong, A. Inserra, M. D. Lewis et al., "Inflammasome signaling affects anxiety- and depressive-like behavior and gut microbiome composition," *Molecular Psychiatry*, vol. 21, no. 6, pp. 797–805, 2016.

[5] E. G. Vichaya, G. Laumet, D. L. Christian et al., "Motivational changes that develop in a mouse model of inflammation-induced depression are independent of indoleamine 2,3 dioxygenase," *Neuropsychopharmacology*, vol. 44, no. 2, pp. 364–371, 2019.

[6] C. Barua, B. Saikia, X. Ren et al., "Zanthoxylum alatum attenuates lipopolysaccharide-induced depressive-like behavior in mice hippocampus," *Pharmacognosy Magazine*, vol. 14, no. 59, p. 673, 2018.

[7] C. C. S. K. Barua, P. Haloi, L. Buragohain et al., "Erigeron linifolius attenuates lipopolysachharide-induced depressive-like behavior in mice by impeding neuroinflammation, oxido-nitrosative stress, and upregulation of tropomyosin receptor kinase B-derived neurotrophic factor and monoaminergic pathway in the hippocampus," *Pharmacognosy Magazine*, vol. 15, no. 62, p. 12, 2019.

[8] J. Zhao, L. X. Lao, W. Cui, and J. H. Rong, "Potential link between the RagA-mTOR-p70S6K axis and depressive-behaviors during bacterial liposaccharide challenge," *Journal of Neuroinflammation*, vol. 16, no. 1, 2019.

[9] J. O. Lipton and M. Sahin, "The neurology of mTOR," *Neuron*, vol. 84, no. 2, pp. 275–291, 2014.

[10] D. W. Lamming, L. Ye, P. Katajisto et al., "Rapamycin-induced insulin resistance is mediated by mTORC2 loss and uncoupled from longevity," *Science*, vol. 335, no. 6076, pp. 1638–1643, 2012.

[11] J. Kim and K. L. Guan, "mTOR as a central hub of nutrient signalling and cell growth," *Nature Cell Biology*, vol. 21, no. 1, pp. 63–71, 2019.

[12] A. Ardestani, B. Lupse, Y. Kido, G. Leibowitz, and K. Maedler, "mTORC1 Signaling: A Double-Edged Sword in Diabetic β Cells," *Cell Metabolism*, vol. 27, no. 2, pp. 314–331, 2018.

[13] X. Gu, J. M. Orozco, R. A. Saxton et al., "SAMTOR is anS-adenosylmethionine sensor for the mTORC1 pathway," *Science*, vol. 358, no. 6364, pp. 813–818, 2017.

[14] R. L. Wolfson and D. M. Sabatini, "The dawn of the age of amino acid sensors for the mTORC1 pathway," *Cell Metabolism*, vol. 26, no. 2, pp. 301–309, 2017.

[15] R. L. Wolfson, L. Chantranupong, G. A. Wyant et al., "KICSTOR recruits GATOR1 to the lysosome and is necessary for nutrients to regulate mTORC1," *Nature*, vol. 543, no. 7645, pp. 438–442, 2017.

[16] C. M. Hale, Q. Cheng, D. Ortuno et al., "Identification of modulators of autophagic flux in an image-based high content siRNA screen," *Autophagy*, vol. 12, no. 4, pp. 713–726, 2016.

[17] S. Notomi, K. Ishihara, N. E. Efstathiou et al., "Genetic LAMP2 deficiency accelerates the age-associated formation of basal laminar deposits in the retina," *Proceedings of the National Academy of Sciences of the United States of America*, vol. 116, no. 47, pp. 23724–23734, 2019.

[18] K. Fukumoto, M. V. Fogaça, R. J. Liu et al., "Activity-dependent brain-derived neurotrophic factor signaling is required for the antidepressant actions of (2R,6R)-hydroxynorketamine," *Proceedings of the National Academy of Sciences of the United States of America*, vol. 116, no. 1, pp. 297–302, 2019.

[19] A. Aguilar-Valles, D. de Gregorio, E. Matta-Camacho et al., "Antidepressant actions of ketamine engage cell-specific translation via eIF4E," *Nature*, vol. 590, no. 7845, pp. 315–319, 2021.

[20] L. M. Monteggia, R. C. Malenka, and K. Deisseroth, "The best way forward," *Nature*, vol. 515, no. 7526, pp. 200-201, 2014.

[21] Y. Liu, D. Lin, B. Wu, and W. Zhou, "Ketamine abuse potential and use disorder," *Brain Research Bulletin*, vol. 126, Part 1, pp. 68–73, 2016.

[22] X. Sun, T. Zhang, Y. Zhao, E. Cai, H. Zhu, and S. Liu, "The protective effect of 5-O-methylvisammioside on LPS-induced depression in mice by inhibiting the over activation of BV-2 microglia through Nf-κB/IκB-α pathway," *Phytomedicine*, vol. 79, article 153348, 2020.

[23] J. Zhao, D. Luo, Z. Liang, L. Lao, and J. Rong, "Plant natural product puerarin ameliorates depressive behaviors and chronic pain in mice with spared nerve injury (SNI)," *Molecular Neurobiology*, vol. 54, no. 4, pp. 2801–2812, 2017.

[24] X. Song, W. Wang, S. Ding, X. Liu, Y. Wang, and H. Ma, "Puerarin ameliorates depression-like behaviors of with chronic unpredictable mild stress mice by remodeling their gut microbiota," *Journal of Affective Disorders*, vol. 290, pp. 353–363, 2021.

[25] A. Tantipongpiradet, O. Monthakantirat, O. Vipatpakpaiboon et al., "Effects of puerarin on the ovariectomy-induced depressive-like behavior in ICR mice and its possible mechanism of action," *Molecules*, vol. 24, no. 24, p. 4569, 2019.

[26] J. L. Warner-Schmidt, K. E. Vanover, E. Y. Chen, J. J. Marshall, and P. Greengard, "Antidepressant effects of selective serotonin reuptake inhibitors (SSRIs) are attenuated by antiinflammatory drugs in mice and humans," *Proceedings of the*

National Academy of Sciences of the United States of America, vol. 108, no. 22, pp. 9262–9267, 2011.

[27] K. F. Hansen, K. Sakamoto, C. Pelz, S. Impey, and K. Obrietan, "Profiling status epilepticus-induced changes in hippocampal RNA expression using high-throughput RNA sequencing," *Scientific Reports*, vol. 4, no. 1, 2015.

[28] R. C. Bagot, H. M. Cates, I. Purushothaman et al., "Circuit-wide transcriptional profiling reveals brain region-specific gene networks regulating depression susceptibility," *Neuron*, vol. 90, no. 5, pp. 969–983, 2016.

[29] M. Pertea, D. Kim, G. M. Pertea, J. T. Leek, and S. L. Salzberg, "Transcript-level expression analysis of RNA-seq experiments with HISAT, StringTie and Ballgown," *Nature Protocols*, vol. 11, no. 9, pp. 1650–1667, 2016.

[30] A. C. Frazee, G. Pertea, A. E. Jaffe, B. Langmead, S. L. Salzberg, and J. T. Leek, "Ballgown bridges the gap between transcriptome assembly and expression analysis," *Nature Biotechnology*, vol. 33, no. 3, pp. 243–246, 2015.

[31] F. Y. Ngo, W. Wang, Q. Chen et al., "Network Pharmacology Analysis and Molecular Characterization of the Herbal Medicine Formulation Qi-Fu-Yin for the Inhibition of the Neuroinflammatory Biomarker iNOS in Microglial BV-2 Cells: Implication for the Treatment of Alzheimer's Disease," *Oxidative Medicine and Cellular Longevity*, vol. 2020, Article ID 5780703, 15 pages, 2020.

[32] W. Zhu, J. Li, Y. Liu, K. Xie, L. Wang, and J. Fang, "Mesencephalic astrocyte-derived neurotrophic factor attenuates inflammatory responses in lipopolysaccharide-induced neural stem cells by regulating NF-κB and phosphorylation of p38-MAPKs pathways," *Immunopharmacology and Immunotoxicology*, vol. 38, no. 3, pp. 205–213, 2016.

[33] H. Azari, S. Sharififar, M. Rahman, S. Ansari, and B. A. Reynolds, "Establishing embryonic mouse neural stem cell culture using the neurosphere assay," *Journal of Visualized Experiments*, vol. 47, no. 47, 2011.

[34] J. Zhao, Y. Cheng, C. Yang et al., "Botanical drug puerarin attenuates 6-hydroxydopamine (6-OHDA)-induced neurotoxicity via upregulating mitochondrial enzyme arginase-2," *Molecular Neurobiology*, vol. 53, no. 4, pp. 2200–2211, 2016.

[35] D. Luo, Y. Guo, Y. Cheng, J. Zhao, Y. Wang, and J. Rong, "Natural product celastrol suppressed macrophage M1 polarization against inflammation in diet-induced obese mice via regulating Nrf2/HO-1, MAP kinase and NF-κB pathways," *Aging (Albany NY)*, vol. 9, no. 10, pp. 2069–2082, 2017.

[36] R. J. Elsworthy and S. Aldred, "Depression in Alzheimer's disease: an alternative role for selective serotonin reuptake inhibitors?," *Journal of Alzheimer's Disease*, vol. 69, no. 3, pp. 651–661, 2019.

[37] A. K. Walker, E. E. Wing, W. A. Banks, and R. Dantzer, "Leucine competes with kynurenine for blood-to-brain transport and prevents lipopolysaccharide-induced depression-like behavior in mice," *Molecular Psychiatry*, vol. 24, no. 10, pp. 1523–1532, 2019.

[38] J. Rothmore, "Antidepressant-induced sexual dysfunction," *The Medical Journal of Australia*, vol. 212, no. 7, pp. 329–334, 2020.

[39] L. T. Park and C. A. Zarate Jr., "Depression in the primary care setting," *The New England Journal of Medicine*, vol. 380, no. 6, pp. 559–568, 2019.

[40] J. Cheng, M. Chen, J. X. Zhu et al., "FGF-2 signaling activation in the hippocampus contributes to the behavioral and cellular responses to puerarin," *Biochemical Pharmacology*, vol. 168, pp. 91–99, 2019.

[41] M. J. Girgenti and R. S. Duman, "Transcriptome alterations in posttraumatic stress disorder," *Biological Psychiatry*, vol. 83, no. 10, pp. 840–848, 2018.

[42] B. Liu, Z. Zhang, E. N. Dai, J. X. Tian, J. Z. Xin, and L. Xu, "Modeling osteosarcoma progression by measuring the connectivity dynamics using an inference of multiple differential modules algorithm," *Molecular Medicine Reports*, vol. 16, no. 2, pp. 1047–1054, 2017.

[43] C. Cho, P. M. Smallwood, and J. Nathans, "Reck and Gpr124 are essential receptor cofactors for Wnt7a/Wnt7b-specific signaling in mammalian CNS angiogenesis and blood-brain barrier regulation," *Neuron*, vol. 95, no. 5, pp. 1056–1073.e5, 2017.

[44] M. D. Mardones, G. A. Andaur, M. Varas-Godoy et al., "Frizzled-1 receptor regulates adult hippocampal neurogenesis," *Molecular Brain*, vol. 9, no. 1, p. 29, 2016.

[45] S. Yu, F. Galeffi, R. M. Rodriguiz et al., "Small ubiquitin-like modifier 2 (SUMO2) is critical for memory processes in mice," *The FASEB Journal*, vol. 34, no. 11, pp. 14750–14767, 2020.

[46] M. Gralle, "The neuronal insulin receptor in its environment," *Journal of Neurochemistry*, vol. 140, no. 3, pp. 359–367, 2017.

[47] I. Pomytkin, J. P. Costa-Nunes, V. Kasatkin et al., "Insulin receptor in the brain: mechanisms of activation and the role in the CNS pathology and treatment," *CNS Neuroscience & Therapeutics*, vol. 24, no. 9, pp. 763–774, 2018.

[48] I. B. da Costa, R. W. de Labio, L. T. Rasmussen et al., "Change in INSR, APBA2 and IDE gene expressions in brains of Alzheimer's disease patients," *Current Alzheimer Research*, vol. 14, no. 7, pp. 760–765, 2017.

[49] L. Racioppi, E. R. Nelson, W. Huang et al., "CaMKK2 in myeloid cells is a key regulator of the immune-suppressive microenvironment in breast cancer," *Nature Communications*, vol. 10, no. 1, p. 2450, 2019.

[50] X. Wang, G. C. Wang, J. Rong et al., "Identification of steroidogenic components derived from Gardenia jasminoides ellis potentially useful for treating postmenopausal syndrome," *Frontiers in Pharmacology*, vol. 9, p. 390, 2018.

[51] DIAGRAM, MuTHER, J. S. Kooner et al., "Genome-wide association study in individuals of South Asian ancestry identifies six new type 2 diabetes susceptibility loci," *Nature Genetics*, vol. 43, no. 10, pp. 984–989, 2011.

[52] A. Goldman, J. L. Smalley, M. Mistry et al., "A computationally inspired in-vivo approach identifies a link between amygdalar transcriptional heterogeneity, socialization and anxiety," *Translational Psychiatry*, vol. 9, no. 1, p. 336, 2019.

[53] S. R. Oliveira, C. Figueiredo-Pereira, C. B. Duarte, and H. L. A. Vieira, "P2X7 receptors mediate CO-induced alterations in gene expression in cultured cortical astrocytes-transcriptomic study," *Molecular Neurobiology*, vol. 56, no. 5, pp. 3159–3174, 2019.

[54] D. Wang, S. Zhang, and B. Liu, "TAF5L functions as transcriptional coactivator of MITF involved in the immune response of the clam *Meretrix petechialis*," *Fish & Shellfish Immunology*, vol. 98, pp. 1017–1023, 2020.

[55] D. Seruggia, M. Oti, P. Tripathi et al., "TAF5L and TAF6L maintain self-renewal of embryonic stem cells via the MYC regulatory network," *Molecular Cell*, vol. 74, no. 6, pp. 1148–1163.e7, 2019, e7.

[56] H. Ma, H. M. Ng, X. Teh et al., "Zfp322a regulates mouse ES cell pluripotency and enhances reprogramming efficiency," *PLoS Genetics*, vol. 10, no. 2, article e1004038, 2014.

[57] H. Fraga, J. J. Bech-Serra, F. Canals, G. Ortega, O. Millet, and S. Ventura, "The Mitochondrial Intermembrane Space Oxireductase Mia40 Funnels the Oxidative Folding Pathway of the Cytochrome *c* Oxidase Assembly Protein Cox19," *The Journal of Biological Chemistry*, vol. 289, no. 14, pp. 9852–9864, 2014.

[58] K. A. Lawson, C. M. Sousa, X. Zhang et al., "Functional genomic landscape of cancer-intrinsic evasion of killing by T cells," *Nature*, vol. 586, no. 7827, pp. 120–126, 2020.

[59] X. Wang, Y. Bai, Y. Han, J. Meng, and H. Liu, " Downregulation of GBAS regulates oral squamous cell carcinoma proliferation and apoptosis via the p53 signaling pathway ," *Oncotargets and Therapy*, vol. Volume 12, pp. 3729–3742, 2019.

[60] S. G. Wu, Y. J. Huang, B. Bao et al., "miR-508-5p acts as an anti-oncogene by targeting MESDC1 in hepatocellular carcinoma," *Neoplasma*, vol. 64, no. 1, pp. 40–47, 2017.

[61] J. Stefani, O. Tschesnokowa, M. Parrilla et al., "Disruption of the microglial ADP receptor P2Y13 enhances adult hippocampal neurogenesis," *Frontiers in Cellular Neuroscience*, vol. 12, p. 134, 2018.

[62] G. Jin, S. W. Lee, X. Zhang et al., "Skp2-mediated RagA ubiquitination elicits a negative feedback to prevent amino-acid-dependent mTORC1 hyperactivation by recruiting GATOR1," *Molecular Cell*, vol. 58, no. 6, pp. 989–1000, 2015.

[63] L. Gan, A. Seki, K. Shen et al., "The lysosomal GPCR-like protein GPR137B regulates Rag and mTORC1 localization and activity," *Nature Cell Biology*, vol. 21, no. 5, pp. 614–626, 2019.

[64] J. Kim and E. Kim, "Rag GTPase in amino acid signaling," *Amino Acids*, vol. 48, no. 4, pp. 915–928, 2016.

[65] J. L. Jewell, Y. C. Kim, R. C. Russell et al., "Differential regulation of mTORC1 by leucine and glutamine," *Science*, vol. 347, no. 6218, pp. 194–198, 2015.

[66] S. M. Son, S. J. Park, H. Lee et al., "Leucine signals to mTORC1 via its metabolite acetyl-coenzyme A," *Cell Metabolism*, vol. 29, no. 1, pp. 192–201.e7, 2019, e7.

[67] H. Yang, X. Jiang, B. Li et al., "Mechanisms of mTORC1 activation by RHEB and inhibition by PRAS40," *Nature*, vol. 552, no. 7685, pp. 368–373, 2017.

[68] P. T. Newton, K. K. Vuppalapati, T. Bouderlique, and A. S. Chagin, "Pharmacological inhibition of lysosomes activates the MTORC1 signaling pathway in chondrocytes in an autophagy-independent manner," *Autophagy*, vol. 11, no. 9, pp. 1594–1607, 2015.

[69] J. M. Dwyer, J. G. Maldonado-Avilés, A. E. Lepack, R. J. DiLeone, and R. S. Duman, "Ribosomal protein S6 kinase 1 signaling in prefrontal cortex controls depressive behavior," *Proceedings of the National Academy of Sciences of the United States of America*, vol. 112, no. 19, pp. 6188–6193, 2015.

[70] S. Dutheil, K. T. Ota, E. S. Wohleb, K. Rasmussen, and R. S. Duman, "High-fat diet induced anxiety and anhedonia: impact on brain homeostasis and inflammation," *Neuropsychopharmacology*, vol. 41, no. 7, pp. 1874–1887, 2016.

[71] S. Jung, S. Choe, H. Woo et al., "Autophagic death of neural stem cells mediates chronic stress-induced decline of adult hippocampal neurogenesis and cognitive deficits," *Autophagy*, vol. 16, no. 3, pp. 512–530, 2020.

[72] Y. Hasegawa, X. L. Zhu, and A. Kamiya, "NV-5138 as a fast-acting antidepressant via direct activation of mTORC1 signaling," *The Journal of Clinical Investigation*, vol. 129, no. 6, pp. 2207–2209, 2019.

[73] W. Fan, K. Cheng, X. Qin et al., "mTORC1 and mTORC2 play different roles in the functional survival of transplanted adipose-derived stromal cells in hind limb ischemic mice via regulating inflammation in vivo," *Stem Cells*, vol. 31, no. 1, pp. 203–214, 2013.

[74] B. R. Rosborough, D. Raïch-Regué, B. M. Matta et al., "Murine dendritic cell rapamycin-resistant and rictor-independent mTOR controls IL-10, B7-H1, and regulatory T-cell induction," *Blood*, vol. 121, no. 18, pp. 3619–3630, 2013.

Hindawi
Oxidative Medicine and Cellular Longevity
Volume 2021, Article ID 5531048, 16 pages
https://doi.org/10.1155/2021/5531048

Research Article

Adiponectin Treatment Attenuates Cerebral Ischemia-Reperfusion Injury through HIF-1α-Mediated Antioxidation in Mice

Chan Zhang,[1] Luming Zhen,[2] Zongping Fang,[3] Liang Yu,[4] Yuanyuan Zhang,[2] Haidong Wei,[2] Junfeng Jia,[5] and Shiquan Wang[3]

[1]*Outpatient Department, Xijing Hospital, The Fourth Military Medical University, Xi'an, Shaanxi 710032, China*
[2]*Department of Anesthesiology, The Second Affiliated Hospital of Xi'an Jiaotong University, Xi'an, Shaanxi 710032, China*
[3]*Department of Anesthesiology and Perioperative Medicine, Xijing Hospital, The Fourth Military Medical University, Xi'an, Shaanxi 710032, China*
[4]*Department of Information, The Fourth Military Medical University, Xi'an, Shaanxi 710032, China*
[5]*Department of Immunology, The Fourth Military Medical University, Xi'an, Shaanxi 710032, China*

Correspondence should be addressed to Junfeng Jia; jjfmmu@163.com and Shiquan Wang; wangshiquan-301@163.com

Received 19 February 2021; Revised 1 May 2021; Accepted 10 May 2021; Published 15 July 2021

Academic Editor: Fabiana Morroni

Adiponectin (ADPN) plays an important role in cerebral ischemia-reperfusion injury. Although previous studies have confirmed that ADPN pretreatment has a protective effect on ischemic stroke, the therapeutic effect of ADPN on ischemic stroke and the underlying mechanism are still unclear. In order to clarify these questions, focal transient cerebral ischemia was induced by middle cerebral artery occlusion (MCAO) in mice and ADPN was administered for three times at 6 h, 24 h, and 48 h after reperfusion. Meanwhile, a virus-delivered HIF-1α siRNA was used before ADPN administration. The infarct volume, neurological score, cellular apoptosis, and oxidative stress were assessed at 72 h after reperfusion. The long-term outcome of mice after stroke was recorded as well. The results indicated that ADPN treatment reduced the infarct volume ($P = 0.032$), neurological deficits ($P = 0.047$), cellular apoptosis ($P = 0.041$), and oxidative responses ($P = 0.031$) at 72 h after MCAO. Moreover, ADPN increased both the protein level and transcriptional activity of HIF-1α as evidenced by the transcription levels of VEGF ($P = 0.046$) and EPO ($P = 0.043$) at 72 h after MCAO. However, knockdown of HIF-1α partially reversed the antioxidant and treatment effect of ADPN after cerebral ischemia. In the observation of long-term outcome after ADPN treatment, it demonstrated that ADPN not only prevented the cerebral atrophy ($P = 0.031$) and the neurological function decline ($P = 0.048$), but also promoted angiogenesis ($P = 0.028$) after stroke. In conclusion, our findings suggest that ADPN is effective in treatment of ischemic stroke which could be attributed to the increased antioxidant capacity regulated by HIF-1α.

1. Introduction

Cerebrovascular disease, especially ischemic stroke, is still one of the leading causes of death and disabilities [1]. Although great progresses have been made in the treatment of ischemic stroke as thrombolysis by tissue-type plasminogen activator (t-PA) and endovascular treatment can rescue a few patients, more effective drugs and methods are still urgently needed for the rest of those unfortunate large populations who exceeded the very narrow therapeutic time window [2]. Therefore, more effective treatment methods have always been the goal of stroke study [3]. The adipocyte-secreted protein hormone adiponectin (ADPN) may have a potential therapeutic effect on stroke, as ADPN deficiency aggravates cerebral ischemia injury [4], while overexpression or supplementation of ADPN before stroke

onset is protective [5, 6]. Human studies also indicate the important role of ADPN in stroke: the circulating ADPN was temporarily decreased in the acute phase of ischemic stroke in patients [7], and ADPN was negatively correlated with brain infarct volume and the severity of cerebral NIHSS score [8, 9]. Under physiological conditions, the amount of ADPN in the brain was very low, while in the process of cerebral ischemia injury, the circulating ADPN can enter the brain due to the destruction of the blood-brain barrier. ADPN plays multiple roles through ADPN receptors which are expressed in peripheral tissues and central nervous system. The main functions of ADPN include anti-inflammatory [10], antioxidant [11], and antiatherogenic properties [12]. A recent study confirmed the protective effect of exogenous ADPN pretreatment on ischemic stroke injury and found out that it was mediated through cAMP/PKA signaling [6]. However, the treatment effect of exogenous ADPN after stroke was undetermined, and the underlying mechanisms remain poorly understood.

The oxidative stress and inflammatory reaction are important pathological mechanisms of ischemic stroke. It is suggested that the antioxidant and anti-inflammatory strategy is one of the important methods for the treatment of ischemic stroke [13], such as 3-n butylphthalide, which is currently used in the treatment of stroke in China [14, 15]. A recent study interestingly revealed that ADPN also had antioxidant and anti-inflammatory functions when administrated before ischemic stroke, suggesting its clinical therapeutic potential for stroke [16]. However, the specific mechanism by which ADPN alleviates oxidative stress and inflammation was unclear. Hypoxia inducible factor-1 alpha (HIF-1α) is an important regulatory node in reducing oxidative stress and inflammation in stroke [17]. As we found its expression rapidly rises in the penumbra after ischemic stroke [18], we wonder whether HIF-1α was also involved in the treatment effect of ADPN after ischemic stroke.

Therefore, the present study is aimed at determining whether treatment with ADPN would attenuate cerebral ischemia-reperfusion injury through the increased antioxidant capacity dependent on HIF-1α.

2. Materials and Methods

2.1. Animals. Male C57 mice, 8-10 weeks old, weighing 20-25 g, were purchased from the Experimental Animal Center of Fourth Military Medical University (Xi'an, China). All the animals were housed in an environment with temperature of 22 ± 1°C, relative humidity of 50 ± 1%, and a light/-dark cycle of 12/12 h. All animal studies (including the mice euthanasia procedure) were done in compliance with the regulations and guidelines of Fourth Military Medical University institutional animal care and according to the AAALAC and the IACUC guidelines.

2.2. Experimental Design. The study was divided into three main parts: the first part was to investigate the effectiveness of ADPN treatment on experimental stroke produced by middle cerebral artery occlusion (MCAO). Briefly, 80 mice were randomly allocated into four groups: sham group (mice subjected to sham operation), control group (mice subjected to MCAO), vehicle group (mice subjected to MCAO and treated with vehicle at 6 h, 24 h, and 48 h after reperfusion), and ADPN group (mice subjected to MCAO and treated with ADPN at 6 h, 24 h, and 48 h after reperfusion). The dose of ADPN was 5 mg/kg via tail vein injection according to a previous study [6]. Each group was composed of 20 mice: 8 mice were used for evaluation of neurological score and infarct volume, 4 for terminal deoxynucleotidyl transferase-mediated 2′-deoxyuridine 5′-triphosphate nick-end labeling (TUNEL) and immunofluorescence staining, and 4 for biochemical tests and 4 for western blotting analysis. The neurological score, infarct volume, TUNEL-positive neurons, cleaved caspase-3, HIF-1α, erythropoietin (EPO), and vascular endothelial growth factor (VEGF) protein levels were analyzed at 72 h after reperfusion. In addition, the cellular localization of HIF-1α was examined by immunofluorescence staining.

The second part of the experiment was to explore the role of HIF-1α in ADPN treatment after cerebral ischemia-reperfusion by using a virus-delivered HIF-1α siRNA. In this part, 60 mice were randomized into three groups: ADPN, control siRNA, and HIF-1α siRNA groups. ADPN group was the same as the first part. For control siRNA group, mice were treated with stereotactic injection of virus recombined with control siRNA 3 weeks before MCAO, and then, ADPN was injected via tail vein at 6 h, 24 h, and 48 h after reperfusion, and for HIF-1α siRNA group, mice were treated with stereotactic injection of virus recombined with HIF-1α siRNA 3 weeks before MCAO, and then, ADPN was injected via tail vein at 6 h, 24 h, and 48 h after reperfusion. Each group was composed of 20 mice: 8 were used for neurological scoring and infarct volume evaluation, 4 for biochemical tests and 4 for western blotting, and 4 for TUNEL staining. The neurological score, brain infarct volume, cellular apoptosis by TUNEL staining and cleaved caspase-3, and oxidation products were assessed at 72 h after reperfusion.

The third part was to assess the long-term outcome and angiogenesis of mice treated with ADPN after cerebral ischemia. All 32 mice were randomized into two groups: ADPN and vehicle groups. The treatment was the same as the first part. Each group had 16 mice: 8 were used for neurological scoring and brain atrophy evaluation, 4 for immunofluorescence staining, and 4 for western blotting analysis of von Willebrand factor (vWF) 28 days after MCAO.

2.3. Focal Cerebral Ischemia and Reperfusion. Mice were allowed for free access to food and tap water before surgery. Cerebral ischemia was induced by MCAO as previously described [19]. Briefly, the mice were anesthetized with 1.5% isoflurane. A silicon-coated suture (RWD Life Science) was then inserted into the right external carotid artery and advanced through the internal carotid artery to obstruct the MCA. The suture remained in position for 1 h during the arterial occlusion and was then removed to allow subsequent reperfusion. The body temperature of the mice was monitored by a rectal probe and maintained at 37 ± 0.5°C by using a heating pad. A laser Doppler sensor for blood flow

monitoring was placed on the surface of the skull (2 mm caudal and 4 mm lateral to the bregma). A procedure with 80% decrease and 70% recovery of the regional cerebral blood flow was considered to be a successful ischemic injury.

2.4. Assessment of the Neurological Deficit. Based on the scoring system of Garcia et al. [20], the neurological behavior of the mice was assessed 72 h and 28 d postreperfusion by an observer blind to the animal grouping. This system consisted of the following six tests: spontaneous activity, symmetrical movements of the upper and lower limbs, forepaw outstretching, climbing, body proprioception, and response to vibrissal touch. The final score was the sum of all six individual test scores. The minimum neurological score was 3, while the maximum was 18.

The grid-walking test was used to assess the walking performance of the mice. The grid apparatus ($40 \times 20\,cm^2$, each grid cell $2 \times 2\,cm^2$, and height 50 cm) was located in a sound attenuated room. Performance was recorded for 60 s using a video camera located beside the apparatus at an angle of approximately 20 to 40 degrees. A foot slip was recorded when one paw completely missed a bar with the limb falling between the bars or when the paw was correctly placed on the bar but slipped off during weight bearing. The total steps of the left forelimb and hind limb were counted, and the percentage of foot fault was measured by dividing the number of foot slips of the left forelimb and left hind limb by the total number of left steps taken with 60 s [21].

2.5. Measurement of Infarct Size. After mice were euthanized, the brains were removed and the ones with clot formation and/or subarachnoid hemorrhage were eliminated. The brains were first sectioned into 1 mm slices, incubated in a 2% solution of 2,3,5-triphenyltetrazolium chloride (MP Biomedicals) at 37°C for 15 min, and then fixed in 4% formalin. The stained sections were photographed using a digital camera and measured in a blinded manner with an image analysis software. The total volumes of both contralateral (vc) and ipsilateral hemisphere (vl) were measured, and the infarct percentage (%I) was calculated using the following formula: $\%I = 100 * (vc - vl)/vc$, to avoid mismeasurement secondary to edema.

2.6. Brain Atrophy Measurement. Mice were anesthetized and then perfused with ice-cold saline, followed by fixation with 4% paraformaldehyde. The brains were then cut into 12 μm thick coronal sections. Nissl staining was carried out according to manufacturer instructions. Briefly, the sections were washed with PBS for 3 times. All sections were stained with 1% methylviolet for 10 min. The sections were rinsed with double distilled water several times. Graded ethanol and xylenes were then used to treat the sections. Finally, the sections were imaged under a light microscope. The atrophy volumes were counted by investigators who were blinded to the grouping in our study. The formula was contralateral hemisphere brain area minus infarct hemisphere area to contralateral hemisphere brain area.

2.7. Microvessel Counts. Six 12 μm thick coronal sections were stained with vWF from 0.5 mm anterior to 0.5 mm posterior in bregma. The number of microvessels was carried out using a 10x objective lens. The microvessels with a well-defined linear vessel shape were counted. The number of microvessels was obtained from the averaged number of six sections.

2.8. Transfection of HIF-1α siRNA. The recombinant adeno-associated virus 9 (AAV) containing HIF-1α siRNA-mCherry or control siRNA-mCherry was purchased from Genechem Co., Ltd. (Shanghai, China). The target sequence was 5′-CACCAU GAU UUU ACU ATT-3′, and the control sequence was 5′-UUC UCC GAA CGU GUC ACG-3′. Transfection was processed by stereotactic injection. The injection coordinates were 0.4 mm anterior to bregma, 1.0 mm lateral to the midsagittal line, and 1.5 mm deep from the cranial surface. Three weeks after injection, the reliability of siRNA was determined by immunofluorescence labeling and western blotting, as shown in Supplementary Figure S1.

2.9. Terminal Deoxynucleotidyl Transferase dUTP Nick-End Labeling (TUNEL) Staining. Cellular apoptosis was evaluated at 72 h after reperfusion. TUNEL staining was performed using an in situ cell death detection kit (Roche Diagnostics, Mannheim, Germany) according to the manufacturer's instructions. Mice brains were fixed with 4% paraformaldehyde. The tissue was then cut into 12 μm thick coronal sections from 0.5 mm prior to bregma. Three slices from each mouse were used for TUNEL staining. Three fields from the penumbra zone for each slice were observed using a 40x objective lens. The ratio of TUNEL-positive cells to the number of total cells was considered as the apoptosis index and obtained by an observer blinded to the grouping. The ischemic penumbra area was defined as previously described [19].

2.10. Immunofluorescence Staining. Mice were perfused and fixed with 4% paraformaldehyde at 72 h after reperfusion. After dehydration with 30% sucrose, the brain was frozen and then cut into 12 μm sections (approximately 1.33 mm from the rostral to the bregma). The slices were then washed with PBS, incubated with 0.3% Triton X-100 for 5 min at room temperature, and consequently blocked with 5% fetal bovine serum (BSA) for additional 30 min. Slices were incubated with rabbit anti-HIF-1α antibody (1 : 200, Abcam, Cambridge, London, UK) and rabbit anti-vWF antibody (1 : 100, Abcam, Cambridge, London, UK) at 4°C overnight, consequently probed with Alexa Fluor 488-conjugated donkey anti-rabbit antibody (1 : 400, Abcam, Cambridge, London, UK) and NeuroTrace red (1 : 2000, Molecular Probes; a dye for labeling of neurons based on Nissl stain), and finally visualized under a microscope (OLYMPUS, BX51) using the DP2-BSW software. Three fields from the penumbra zone for each slice were observed using a 40x objective lens.

2.11. Western Blot Analysis. The brain tissue of the ischemic penumbra was dissected at 72 h after reperfusion. All samples were homogenized in a RIPA lysis buffer (Beyotime, Nantong, China) containing whole proteinase inhibitor cocktail on ice. A BCA protein assay kit (Beyotime, Nantong, China) was used to determine the protein concentration. An equivalent amount of protein (30 μg per lane) was loaded and

separated by a 12% SDS-PAGE gel. After electrophoresis, the protein was transferred to a polyvinylidene difluoride membrane. The membrane was blocked using 2% BSA in TBST. After overnight incubation at 4°C with the primary antibodies HIF-1α (1 : 1000, Abcam, Cambridge, London, UK), EPO (1 : 1000, Abcam, Cambridge, London, UK), VEGF (1 : 1000, Abcam, Cambridge, London, UK), vWF (1 : 1000, Abcam, Cambridge, London, UK), and β-actin (1 : 1000. Abcam, Cambridge, London, UK), the membrane was incubated with horseradish peroxidase-conjugated secondary goat anti-rabbit antibody (1 : 5000, Pierce, Rockford, IL) for 1 h at room temperature. Optical density of each band was quantified using the ImageJ software. The dissection of ischemic penumbra was as previously described [22]. Briefly, the brain was coronally cut into three slices: the first cutting was 2 mm from the anterior tip of the frontal lobe, and the second cutting was 4 mm from the first cutting. The middle part that corresponded to the ischemic core and penumbra was dissected. The midline between the two hemispheres was identified, and a longitudinal cut (from top to bottom) approximately 1 mm from the midline through infarct hemisphere was made. We then made a transverse diagonal cut at approximately the 2-o'clock position to separate the core (i.e., striatum and overlying cortex) from the penumbra (adjacent cortex).

2.12. Biochemical Estimations. At 72 h after reperfusion, the penumbra was dissected and homogenized in cold sodium chloride after it has been weighted. The homogenate was then centrifuged at 10000 × g for 15 min, and the supernatant was collected and consequently frozen at -80°C for further analysis. The protein content was measured using BCA protein assay kit (Beyotime, Nantong, China).

Assay kits were used to measure the content of oxidation products (MDA, 8-OHdG, protein carbonyl, and protein nitrotyrosine). The carbonyl kit and the nitrotyrosine kit were purchased from CHEMICON. Others were purchased from Nanjing Jiancheng Bioengineering Institute. The assays were done according the manufacturer's instructions.

2.13. Quantitative Reverse Transcription Polymerase Chain Reaction (qRT-PCR) Measurement. Total RNA was extracted from the penumbra of the cerebral cortex with Trizol reagent (Life Technologies, USA) according to the manufacturer's instructions. The cDNA was subsequently synthesized with a standard cDNA synthesis kit (Life Technologies, USA). The mRNA level of β-actin was used as an internal control. The sequences of primers were as follows: VEGF, forward: 5′-GCACTGGACCCTGGCTTTACT-3′ and reverse: 5′-ACTTCACCACTTCATGGGTCTTGTG-3′; HIF-1α, forward: 5′-GTTACAGGATTCCAGCAGACC-3′ and reverse: 5′-TGGGTAGAAGGTGGAGATGC-3′; EPO, forward: 5′-AATGGAGGTGGAAGAACAGG-3′ and reverse: 5′-ACCCGAAGCAGTGAAGTGA-3′.

The reverse transcription reaction was carried out in a 20 μl volume with 500 ng of total RNA, 16°C for 30 min, 42°C for 42 min, and 85°C for 5 min. The PCR cycling began with template denaturing at 95°C for 5 min, followed by 40 cycles of 95°C for 10 s, 60°C for 20 s, 72°C for 20 s, and 78°C for 20 s.

2.14. Statistical Analysis. Data were presented as mean ± standard error. Statistical analysis was performed using the Statistical Package for the Social Sciences (SPSS) version 16.0 for Windows, except for neurological scores which were expressed as median with interquartile range and consequently analyzed by Kruskal-Wallis tests. The Bonferroni test was used as a correction method. Other values were analyzed by one-way ANOVA, followed by post hoc Tukey test. A P value less than 0.05 was considered statistically significant.

3. Results

3.1. ADPN Treatment Reduced Cerebral Ischemia-Reperfusion Injury. The effect of ADPN administration on infarct volume and neurological deficit in mice were observed at 72 h after cerebral ischemia. The infarct volumes were notably decreased in ADPN group when compared to vehicle group (44.3% ± 5.1% vs. 26.2% ± 4.5%, $P < 0.05$, Figures 1(a) and 1(b)). The neurological score was increased in the ADPN group when compared to vehicle group [12 (2) vs. 8.5 (1.5), $P < 0.05$, Figure 1(c)]. The grid-walking test showed that ADPN increased the total steps (21 ± 5.2 vs. 58 ± 6.3, $P < 0.05$, Figure 1(d)) and reduced the error ratio (12.7% ± 3.2% vs. 28.7% ± 5.6%, $P < 0.05$, Figure 1(e)). There is no statistical difference between the control group and vehicle group in infarct volume, neurological score, and step error.

3.2. ADPN Treatment Inhibited Apoptosis in Cerebral Ischemic Penumbra. Cellular apoptosis was analyzed to confirm the neuroprotective effect of ADPN. Representative photomicrographs of TUNEL staining in the ischemic penumbra area are shown in Figure 2(a). Compared to vehicle groups, ADPN induced a reduction in TUNEL-positive cells (18.9 ± 4.9% vs. 35.4 ± 4.6%, $P < 0.05$), while no significant difference in the number of TUNEL-positive neurons was observed between the control and vehicle groups at 72 h post-reperfusion ($P > 0.05$), as shown in Figure 2(b). Furthermore, levels of cleaved caspase-3 were analyzed by western blotting at 72 h after reperfusion. Compared to vehicle group, ADPN treatment decreased the levels of cleaved caspase-3 (1.7 ± 0.3 vs. 3.1 ± 0.4, $P < 0.05$); in addition, no difference was observed between the control group (2.9 ± 0.4 vs. 3.1 ± 0.4, $P > 0.05$) and vehicle group, as shown in Figure 2(c).

3.3. ADPN Treatment Mitigated Oxidative Stress after Reperfusion. To further determine whether exogenous ADPN could reduce the oxidative stress injury, indicators of protein oxidation (carbonyl protein and nitrotyrosine protein contents) and indicators of DNA injury 8-OHdG and lipid peroxidation MDA were analyzed, respectively, in ischemic penumbra at 72 h postreperfusion (Figure 3). Compared with the vehicle group, ADPN treatment reduced all these factors: the carbonyl protein content (14.8 ± 2.8 μmol/mg vs. 23.0 ± 3.1 μmol/mg, $P < 0.05$, Figure 3(a)), the nitrotyrosine protein content (9.4 ± 1.3 μg/mg vs. 15.9 ± 1.9 μg/mg, $P < 0.05$, Figure 3(b)), the 8-OHdG content (41.7 ± 9.1 pg/mg DNA

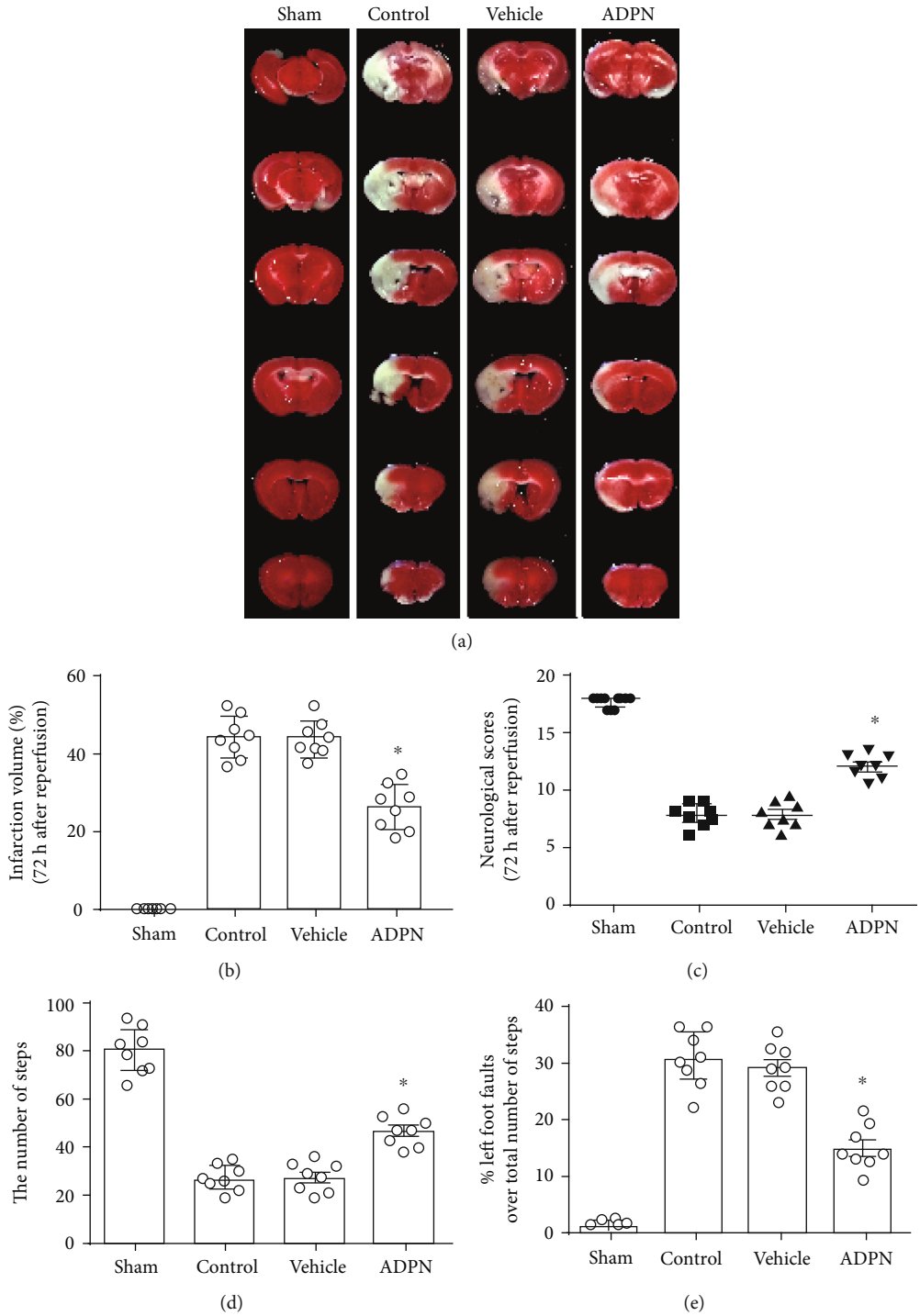

Figure 1: ADPN treatment exerted neuroprotective effect against cerebral ischemia injury in mice. (a) Representative photographs of brain slices showing infract volume assessed 72 h after reperfusion in mice. (b) The infarct volumes as percentages of the contralateral hemisphere are presented as the mean ± SD and analyzed by one-way ANOVA with Tukey's posttest. (c) The scoring system of Garcia et al. was evaluated 72 h after reperfusion. The data are presented as the median with range and analyzed by the Kruskal-Wallis test followed by Dunn's test. (d) The total steps were assessed at 72 h after reperfusion. (e) The error ratio was assessed at 72 h after reperfusion. $^*P < 0.05$ compared to the vehicle group. $n = 8$ per group.

vs. 84.2 ± 11.7 pg/mg DNA, $P < 0.05$, Figure 3(c)), and the MDA content (2.2 ± 0.5 μg/mg protein vs. 4.7 ± 0.5 μg/mg protein, $P < 0.05$, Figure 3(d)). There was no significant difference between the vehicle group and control group: the carbonyl protein content (23.0 ± 3.1 μmol/mg vs. 23.7 ± 4.5 μmol/mg, $P > 0.05$, Figure 3(a)), the nitrotyrosine protein content (15.9 ± 1.9 μg/mg vs. 15.3 ± 1.2 μg/mg, $P > 0.05$, Figure 3(b)), the 8-OHdG content (84.2 ± 11.7 pg/mg DNA

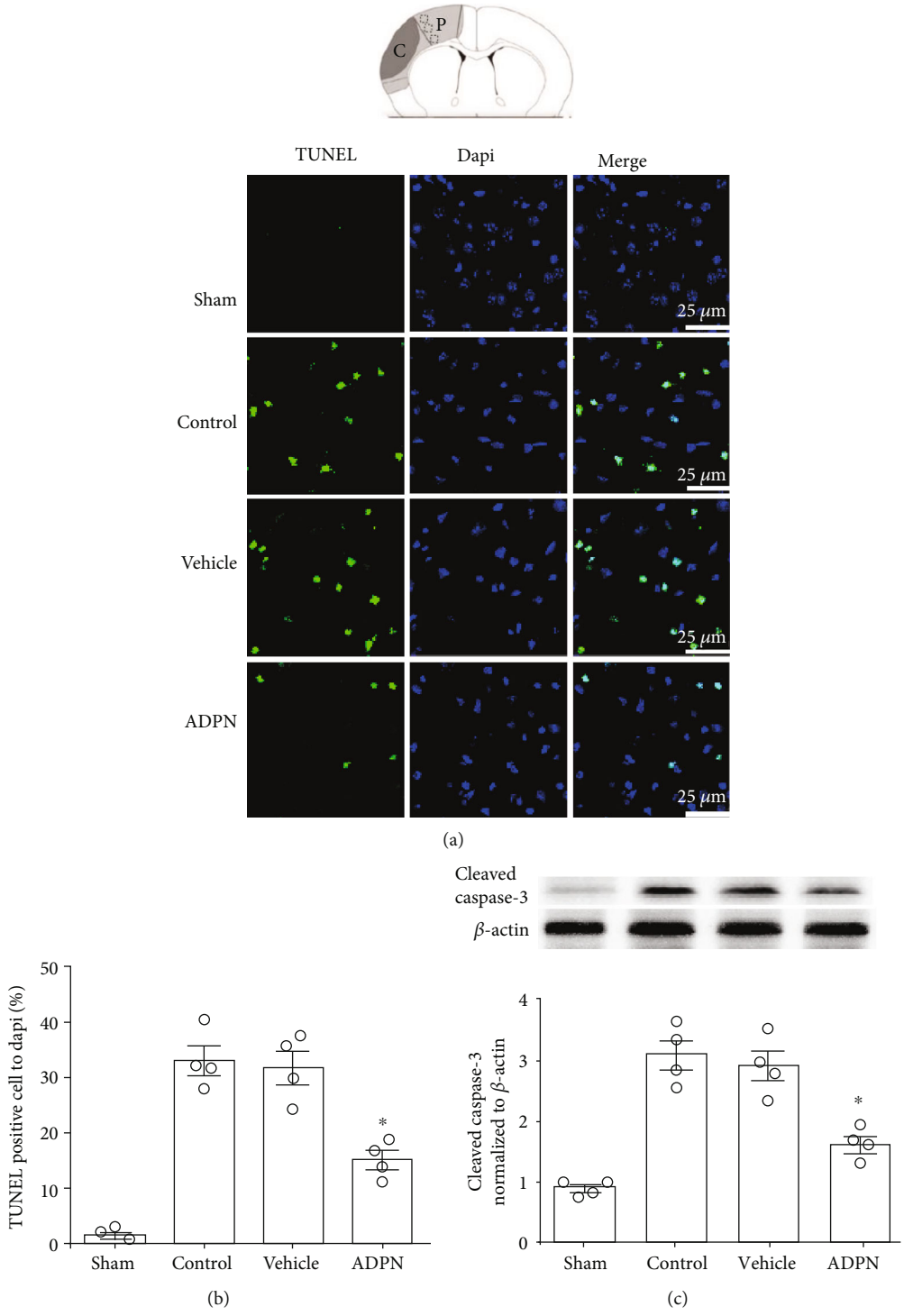

Figure 2: ADPN treatment alleviated apoptosis in the ischemic penumbra. (a) Representative photomicrographs showing TUNEL staining in the ischemic penumbra of mice at 72 h after reperfusion. (b) The percentages of TUNEL-positive cells in the ischemic penumbra. (c) Cleaved caspase-3 level in the ischemia penumbra. Data are presented as the mean ± SD and analyzed by the *Kruskal-Wallis* test followed by *Dunn's* test. $^*P < 0.05$ compared to vehicle group, $n = 4$.

vs. 94.9 ± 14.3 pg/mg DNA, $P > 0.05$, Figure 3(c)), and the MDA content (4.7 ± 0.5 μg/mg protein vs. 4.9 ± 0.7 μg/mg protein, $P > 0.05$, Figure 3(d)).

3.4. ADPN Increased the Neuronal Expression of HIF-1α after Reperfusion. Spatial localization of HIF-1α was determined using immunofluorescence staining. Furthermore, the protein level of HIF-1α was measured by western blotting, and the mRNA level of HIF-1α was tested by qRT-PCR (Figure 4). As shown in Figure 4(a), HIF-1α was mainly expressed in neurons among different groups. Higher HIF-1α protein level was observed after administration of ADPN compared to vehicle

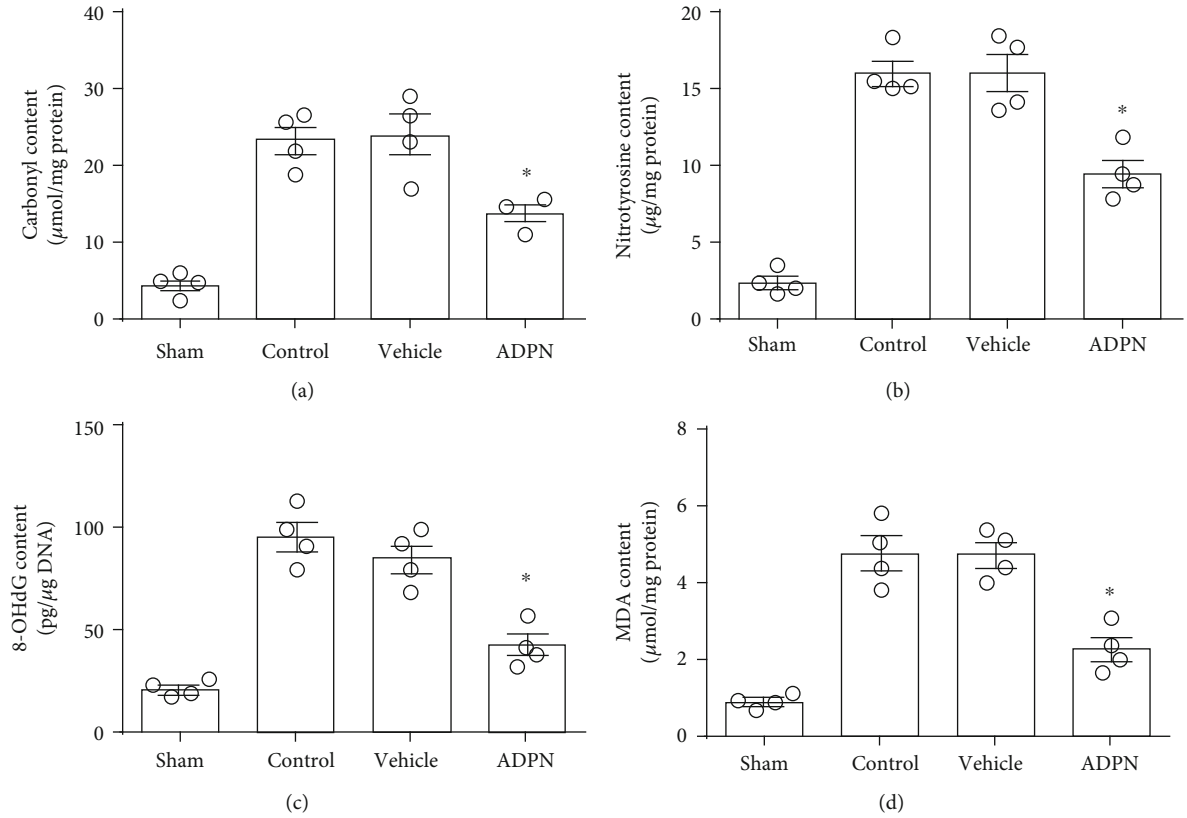

Figure 3: The effect of ADPN on oxidative products. (a) The content of carbonyl protein in the ischemic penumbra. (b) The content of nitrotyrosine protein in the ischemic penumbra. (c) The content of 8-OHdG in the ischemic penumbra. (d) The content of MDA in the ischemic penumbra. Data are presented as the mean ± SD and analyzed by the *Kruskal-Wallis* test followed by *Dunn's* test. $^*P < 0.05$ compared to vehicle group, $n = 4$ per group.

group (5.4 ± 0.8 vs. 3.2 ± 0.7, $P < 0.05$), while no significant difference was found between the vehicle group and control group (3.2 ± 0.7 vs. 3.0 ± 0.5, $P > 0.1$) at 72 h postreperfusion (Figure 4(b)). Moreover, compared to vehicle group (3.8 ± 0.5), exogenous ADPN induced an increase of HIF-1α mRNA (5.4 ± 0.7, $P < 0.05$), while there was no difference between the control group and vehicle group ($P > 0.05$).

3.5. ADPN Increased the Expression of EPO and VEGF after Reperfusion. The expression of HIF-1α target genes EPO and VEGF, which represented the transcriptional activity of the HIF-1α, was analyzed as shown in Figure 5. Compared to vehicle group, ADPN not only increased VEGF protein level (4.6 ± 0.5 vs. 2.2 ± 0.4, $P < 0.05$, Figure 5(a)) and EPO protein level (5.1 ± 0.7 vs. 2.6 ± 0.4, $P < 0.05$, Figure 5(c)), but also increased the mRNA level of VEGF (4.4 ± 0.6 vs. 2.3 ± 0.5, $P < 0.05$, Figure 5(b)) and EPO (4.1 ± 0.4 vs. 2.5 ± 0.4, $P < 0.1$, Figure 5(d)). Both the protein level and mRNA level of EPO and VEGF had no difference between the control group and vehicle group.

3.6. Knockdown of HIF-1α Partly Reversed the Protective Effect of ADPN. In order to investigate the role of HIF-1α in exogenous ADPN-induced cerebral protection after experimental stroke, the recombinant AAV containing HIF-1α siRNA was applied. The neurological score, the infarct volume, TUNEL-positive cells, and the indicators of oxidative stress were measured. Compared to control virus, neurological score was lower in HIF-1α siRNA group [9 (1) vs. 12 (1.5), $P < 0.1$, Figure 6(c)]; the infarct volume was larger ($39.0\% \pm 5.5\%$ vs. $27.2\% \pm 6.7\%$, $P < 0.05$, Figure 6(b)); moreover, the total steps were decreased (52 ± 6.5 vs. $29.1\% \pm 4.3$, $P < 0.05$, Figure 6(d)), and the error ratio was increased ($23.0\% \pm 6.5\%$ vs. $13.1\% \pm 7.3\%$, $P < 0.05$, Figure 6(e)). Meanwhile, HIF-1α siRNA group had more apoptotic cells ($19.6\% \pm 6.5\%$ vs. $28.7\% \pm 5.2\%$, $P < 0.05$, Figure 7(b)) and higher levels of cleaved caspase-3 (2.8 ± 0.5 vs. 1.9 ± 0.3, $P < 0.1$, Figure 7(c)) and worsened oxidative stress injury: the carbonyl protein content ($20.1 \pm 1.8\,\mu$mol/mg vs. $15.0 \pm 2.4\,\mu$mol/mg, $P < 0.05$, Figure 8(a)), the nitrotyrosine protein content ($13.2 \pm 1.3\,\mu$g/mg vs. $8.9 \pm 1.3\,\mu$g/mg, $P < 0.05$, Figure 8(b)), the 8-OHdG content (63.8 ± 8.4 pg/mg DNA vs. 40.2 ± 5.1 pg/mg DNA, $P < 0.05$, Figure 8(c)), and the MDA content ($4.0 \pm 0.5\,\mu$g/mg protein vs. $2.3 \pm 0.4\,\mu$g/mg protein, $P < 0.05$, Figure 8(d)).

3.7. ADPN Improved Long-Term Neurological Behavioral and Promoted Angiogenesis. To investigate the effect of ADPN on long-term brain injury after MCAO, the brain atrophy volume and the behavioral deficits was assessed 28 days after

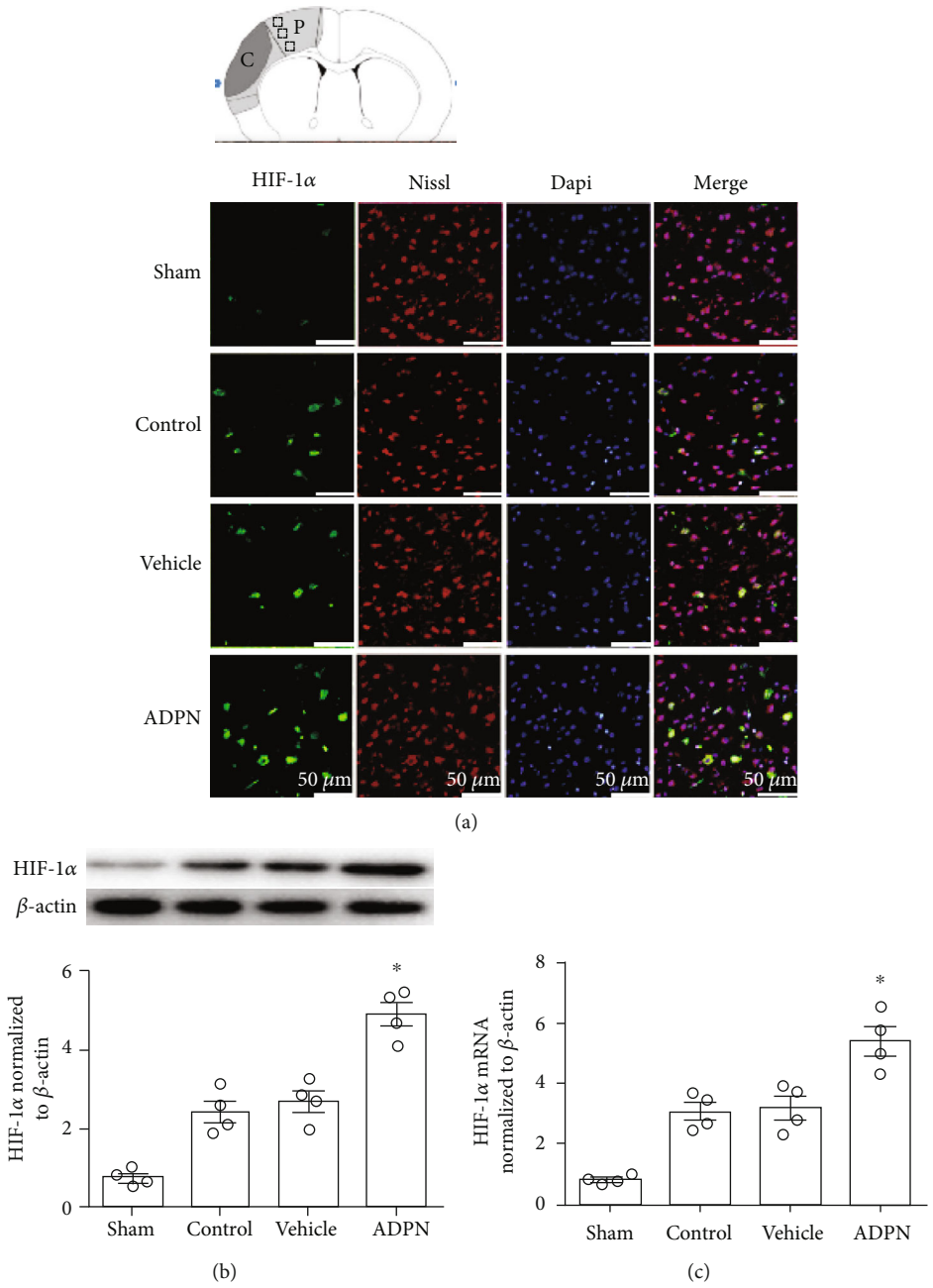

Figure 4: ADPN enhanced the proteins and mRNA expression of HIF-1α at 72 h after reperfusion. (a) Representative photomicrographs of HIF-1α staining in the ischemic penumbra. (b) Western blotting analysis of HIF-1α protein expression. (c) The RT-PCR analysis of HIF-1α mRNA. Data are presented as the mean ± SD and analyzed by the *Kruskal-Wallis* test followed by *Dunn's* test. $^*P < 0.05$ compared to vehicle group, $n = 4$ per group.

MCAO. Quantitative analysis revealed that brain atrophy was prevented in ADPN group compared with vehicle group (6.4 ± 1.1% vs. 15.1 ± 1.6%, $P < 0.05$, Figure 9(b)), and similar results were seen in scoring system of Garcia et al. [14 (2) vs. 11.5 (1.5), $P < 0.05$, Figure 1(c)]. Meanwhile, compared to the vehicle group, the ADPN group demonstrated significant improvement in performance of grid-walking test: the total steps were increased (72 ± 12 vs. 53 ± 9, $P < 0.05$, Figure 9(d)), and the error ratio was decreased (10.7% ± 2.2% vs. 5.8% ± 1.6%, $P < 0.05$, Figure 9(e)). To examine the effect of ADPN on angiogenesis after MCAO, the number of microvessels was counted. The number of vWF-stained microvessels in the ADPN group mice on the 28 day after MCAO was more than that in vehicle group (30 ± 5.6 vs. 50 ± 6.1, $P < 0.05$, Figure 9(g)). Similarly, the level of vWF protein in ADPN group was increased than that in vehicle group (1.4 ± 0.3 vs. 0.9 ± 0.3, $P < 0.05$, Figure 9(h)).

4. Discussion

The present study showed that ADPN treatment is effective in reducing cerebral ischemia-reperfusion injury in a mouse

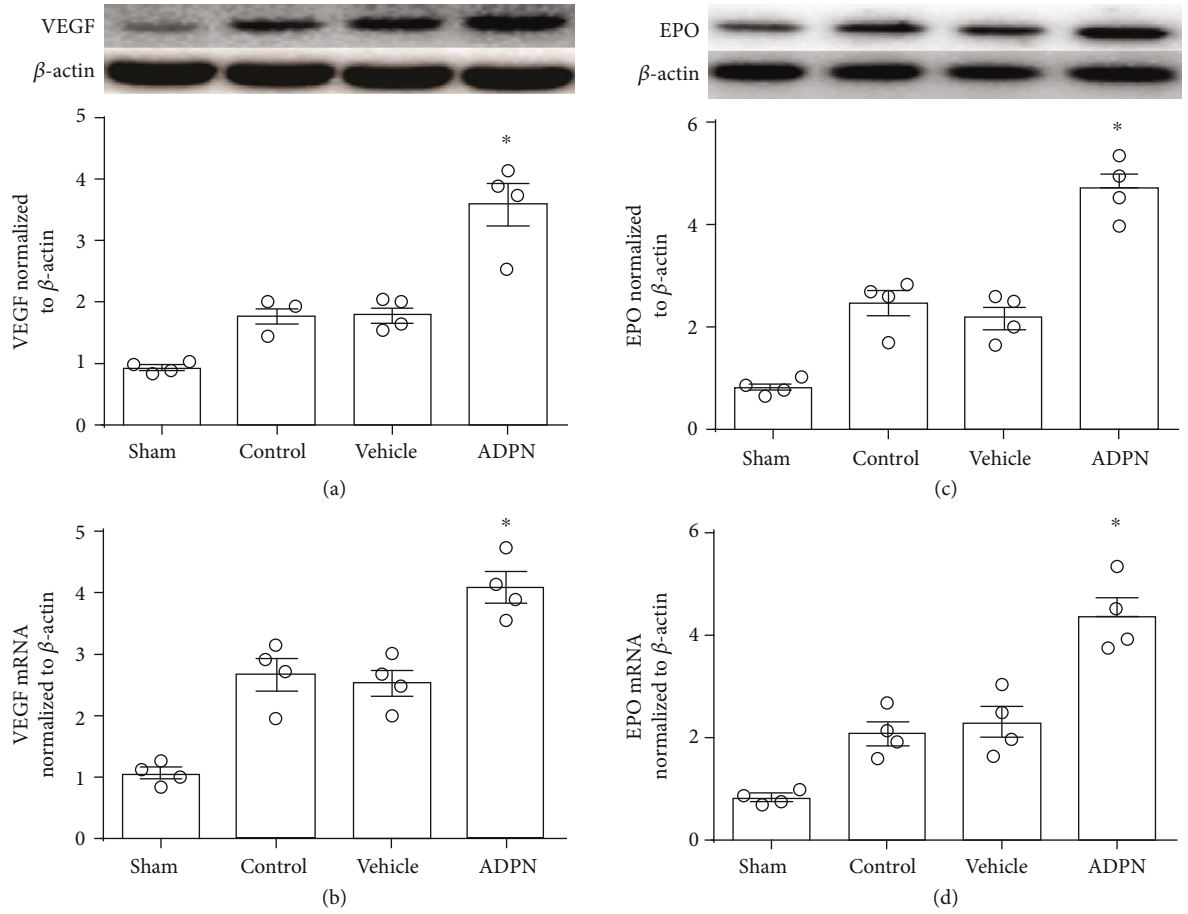

Figure 5: ADPN enhanced the proteins and mRNA expression of VEGF and EPO at 72 h after reperfusion. (a) Western blotting analysis of EPO protein expression. (b) The RT-PCR analysis of EPO mRNA. (c) Western blotting analysis of VEGF protein expression. (d) The RT-PCR analysis of VEGF mRNA. Data are presented as the mean ± SD and analyzed by the *Kruskal-Wallis* test followed by *Dunn's* test. $^*P < 0.05$ compared to vehicle group, $n = 4$ per group.

stroke model. Briefly, the administration of ADPN improved neurological scores, reduced infarct volume, ameliorated neuronal apoptosis, and decreased oxidative products. Such therapeutic effect of ADPN on stroke could be attributed to the boosting of antioxidant capacity by HIF-1α in neurons. Moreover, we also found that ADPN could improve the long-term neurobehavioral outcome and promote angiogenesis in the ischemic penumbra after stroke.

ADPN is mainly produced and secreted by adipose tissue. It can also be synthesized and secreted by nonadipose tissues such as murine cardiomyocytes and human liver. ADPN is known to have antioxidant, antidiabetic, and anti-inflammatory properties, which can confer protection for chronic diseases [11]. Recent studies have identified the association between hypoadiponectinemia and increased mortality following ischemia stroke, as well as the negative correlation between ADPN levels and primary infarct size [23], suggesting ADPN has an important role in stroke. However, under physiological conditions, the amount of APDN in the brain is very low [24]. Nevertheless, the content of ADPN increases in ischemic hemisphere after stroke, while no ADPN mRNA was found in the ischemic hemisphere and contralateral hemisphere [25]. This indicates that the circulating ADPN could enter the brain tissue through injured BBB after ischemia [26], highlighting the feasibility of exogenous ADPN in stroke treatment. Indeed, exogenous ADPN injected before MCAO had protective effect on infarct size and neurological deficit scores [5]. This was consistent with the results obtained by Bai et al., who for the first time demonstrated that ADPN knockout mice exhibited enlarged brain infarct size and worsened neurological deficits following ischemia-reperfusion compared with the wild-type littermates [6]. However, the therapeutic effect of ADPN on ischemic stroke was not examined. Therefore, we initiated ADPN treatment from 6 h after reperfusion and found that multiple doses of ADPN administration could markedly reduce the brain damage after experimental stroke. And the antiapoptotic effect of ADPN when treated after cerebral ischemia corroborated its therapeutic role. The long-term outcome of mice treated with ADPN after reperfusion in further strengthens its effectiveness in stroke treatment. Thus, we for the first time confirmed the therapeutic effect of ADPN after stroke, and the time window could be as long as 6 h after reperfusion.

As the injury secondary to reperfusion is not completely consistent with the primary ischemia injury, the molecular

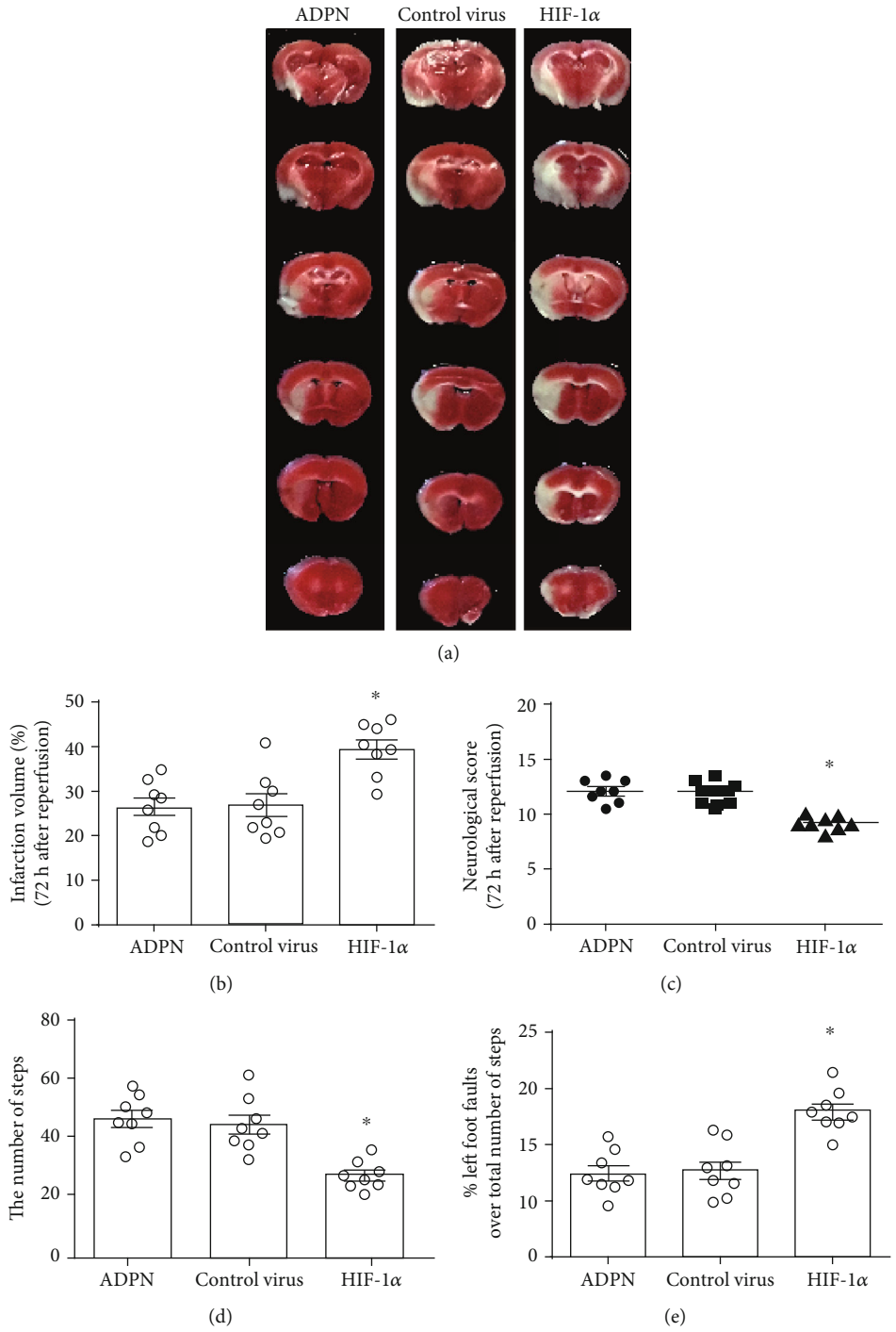

Figure 6: Downregulating HIF-1α with AAV-delivered siRNA can reduce the protective effect of ADPN. (a) Representative photographs of brain slices showing infract volume assessed 72 h after reperfusion in mice. (b) The infarct volumes as percentages of the contralateral hemisphere are presented as the mean ± SD and analyzed by one-way ANOVA with Tukey's posttest. (c) The scoring system of Garcia et al. was evaluated 72 h after reperfusion. The data are presented as the median with range and analyzed by the *Kruskal-Wallis* test followed by *Dunn's* test. (d) The total steps were assessed at 72 h after reperfusion. (e) The error ratio was assessed at 72 h after reperfusion. $^*P < 0.05$ compared to the ADPN group. $n = 8$ per group.

mechanism for ADPN treatment after stroke could be different from its pretreatment before ischemia. Therefore, we focused on the oxidative stress which plays an important role in brain damage [27] including stroke [28] since antioxidant effect is the very common property of ADPN. It has been demonstrated that the oxidative products MDA, 8-OHdG, the carbonyl content, and the nitrotyrosine protein content ould be used for indicators of oxidative stress level and were increased in the pathogenesis of cerebral ischemia-reperfusion injury [29, 30]. We then analyzed these products'

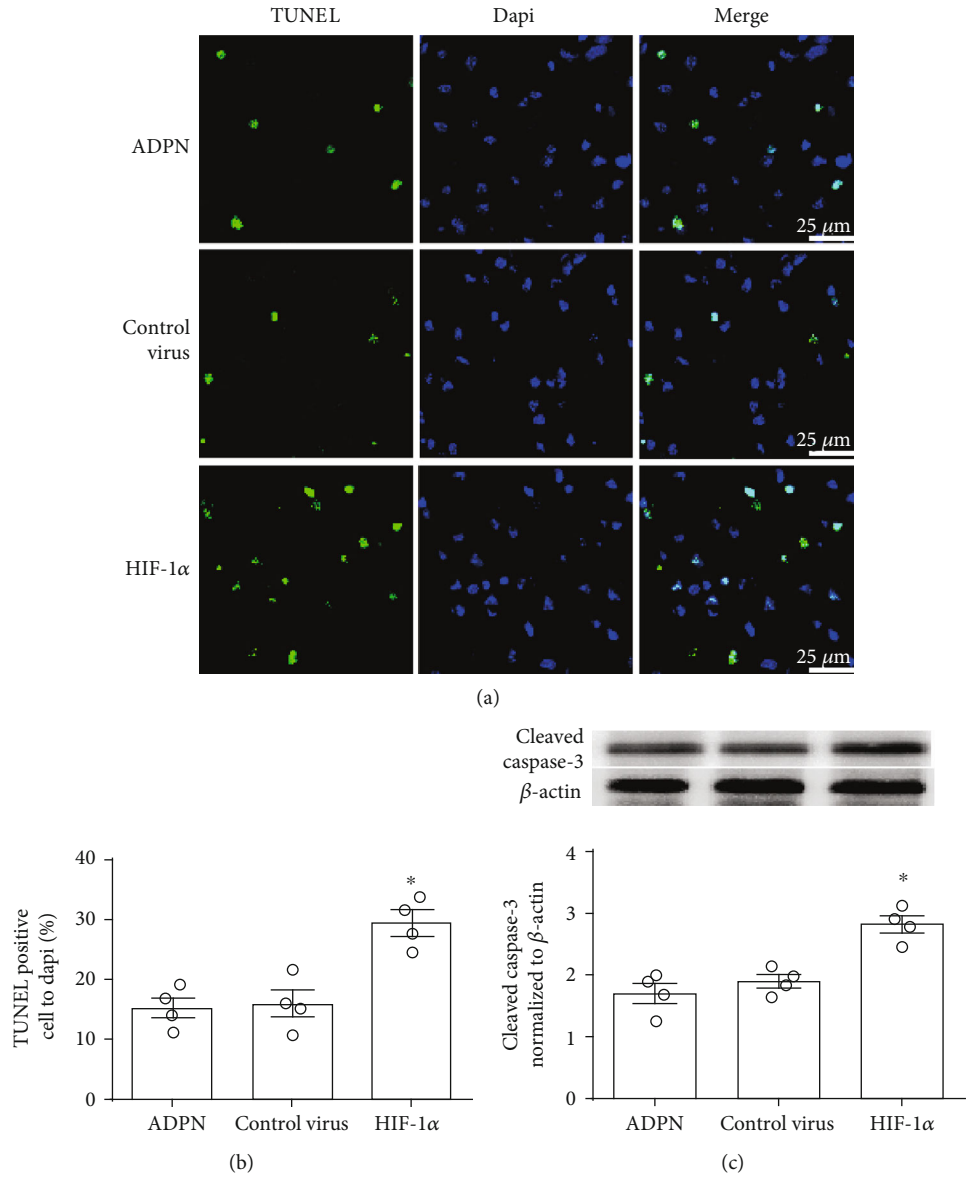

Figure 7: Downregulating HIF-1α with AAV-delivered siRNA reversed the antiapoptotic effect of ADPN. (a) Representative photomicrographs showing TUNEL staining in the ischemic penumbra of mice at 72 h after reperfusion. (b) The percentages of TUNEL-positive cells in the ischemic penumbra. (c) Cleaved caspase-3 level in the ischemia penumbra. Data are presented as the mean ± SD and analyzed by the *Kruskal-Wallis* test followed by *Dunn's* test. $^*P < 0.05$ compared to ADPN group, $n = 4$.

content after treatment with ADPN and found that ADPN effectively mitigated oxidative stress as evidenced by MDA, 8-OHdG, the carbonyl content, and the nitrotyrosine protein content. Given that oxidative stress is an important cause of cell deaths and the antiapoptotic effect of ADPN treatment after experimental stroke, the mitigated oxidative stress by ADPN provides further strengths for its therapeutic potential.

Although the antioxidant effect of ADPN was well studied, the exact molecular mechanism of ADPN was unknown, especially in its neuroprotective effect on stroke. HIF-1α was an important regulatory node in reducing oxidative stress and inflammation in stroke [17] and was activated after cerebral ischemia [31]. As the key regulator of the transcriptional response to low-oxygen conditions in mammalian cells under both physiological and pathophysiological circumstances [32], HIF-1α is essential for the activation of endogenous neuroprotective mechanisms [33]. In fact, HIF-1α has been proposed as a potential target for neurodegenerative diseases [32], since it regulates the expression of a broad range of genes that facilitate cellular adaptation to low-oxygen conditions [32]. Furthermore, it has been shown that neuron-specific knockdown of HIF-1α increases tissue damage and reduces the survival rate of mice subjected to MCAO [17]. Indeed, HIF-1α has been reported to protect neurons from apoptosis caused by oxidative stress [34]. As we recently found out that HIF-1α was rapidly stimulated in the

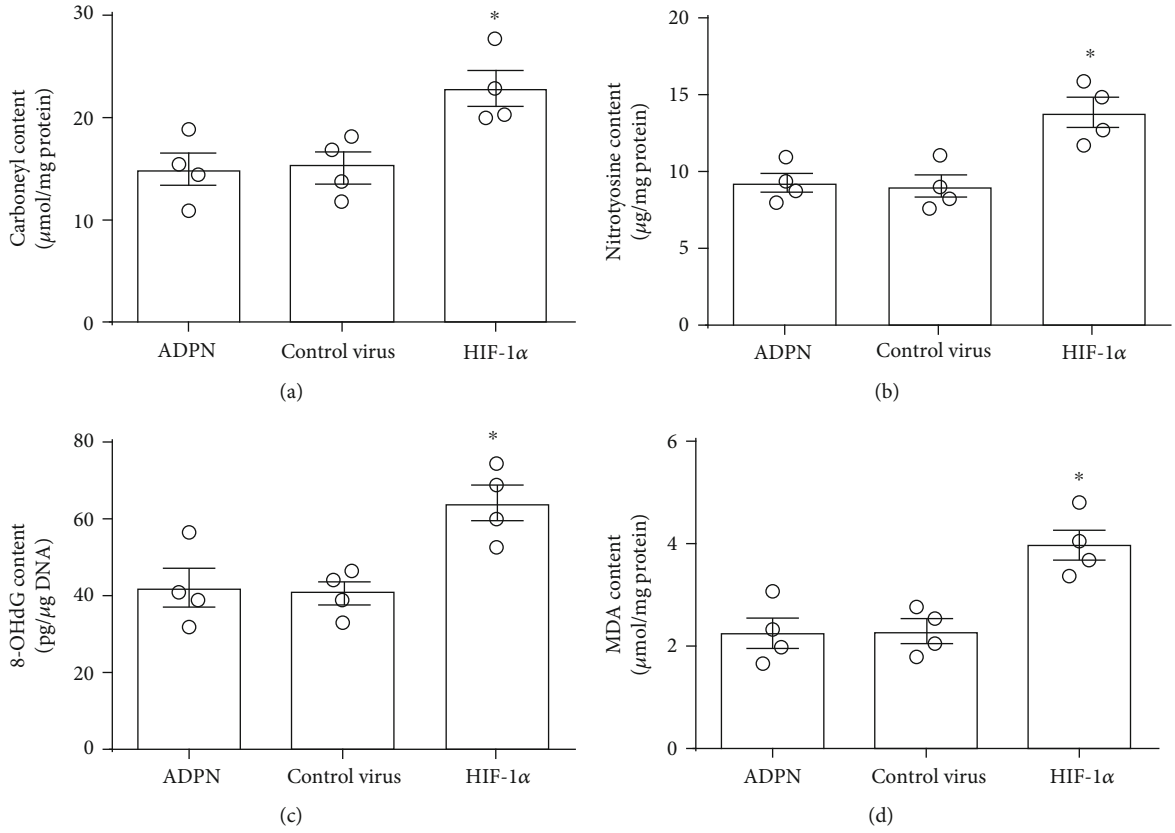

Figure 8: Downregulating HIF-1α with AAV-delivered siRNA reversed the antioxidant effect of ADPN. (a) The content of carbonyl protein in the ischemic penumbra. (b) The content of nitrotyrosine protein in the ischemic penumbra. (c) The content of 8-OHdG in the ischemic penumbra. (d) The content of MDA in the ischemic penumbra. Data are presented as the mean ± SD and analyzed by the *Kruskal-Wallis* test followed by *Dunn's* test. $^*P < 0.05$ compared to ADPN group, $n = 4$ per group.

penumbra after ischemic stroke [18], we thought that HIF-1α might be involved in the treatment effect of ADPN after ischemic stroke. The results of our study revealed that ADPN treatment increased HIF-1α expression in neurons following ischemia stroke, and by using AAV-delivered HIF-1α siRNA to neurons, we proved that HIF-1α was involved in ADPN-induced antioxidant and antiapoptotic effect. Nevertheless, several studies reported opposite effects of HIF-1α in cerebral ischemia. For instance, it was reported that HIF-1α increased apoptosis that led to ischemia-induced delayed neuronal death and HIF-1α deficiency reduced ischemia damage [35, 36]. The discrepancy in findings between these studies may reflect their use of different timings of interventions and multiple roles of HIF-1α in brain damage process after stroke.

Another question is how HIF-1α leads to the regulation of antioxidant function. This could be explained by its target gene products EPO and VEGF [37]. In the present study, we detected the levels of EPO and VEGF, and our results revealed that ADPN increased EPO and VEGF at 72 h after MCAO, which means that ADPN induces both the expression and activity of HIF-1α. Several studies reported that EPO may protect cells by reducing oxidative stress. EPO could exert its antioxidant effect directly by acting on HO-1 and also indirectly by acting on depleting body iron [38]. And exogenous EPO exerted neuroprotection through antioxidant activity after ischemia. In this study, we proved that ADPN increased EPO, suggesting that the antioxidant effect of ADPN may be related to EPO which was regulated HIF-1α. Although previous studies confirmed that HIF-1α/VEGF pathway plays an important role in promoting angiogenesis and cerebral functional repairment, recent studies show that VEGF had antioxidant effects [39], suggesting VEGF could be another important mediator of HIF-1α-regulated antioxidant response. In this study, the results showed that ADPN increased both EPO and VEGF by HIF-1α. However, which of the two was more important was undetermined and whether other reaction processes like anaerobic metabolism or inflammatory response was also involved in the effect of ADPN treatment remains to be further confirmed by experiments.

Many studies indicated that angiogenesis was beneficial for the stroke-injured brain, as high levels of new vessel formation following stroke were correlated with better functional recovery and prolonged survival. Angiogenesis was continued for 4 weeks in the penumbra after ischemia [40]. It was reported that overexpression of ADPN promoted angiogenesis in the mouse brain following MCAO [41], even the same results were found in aged mice [5]. The present study demonstrated that

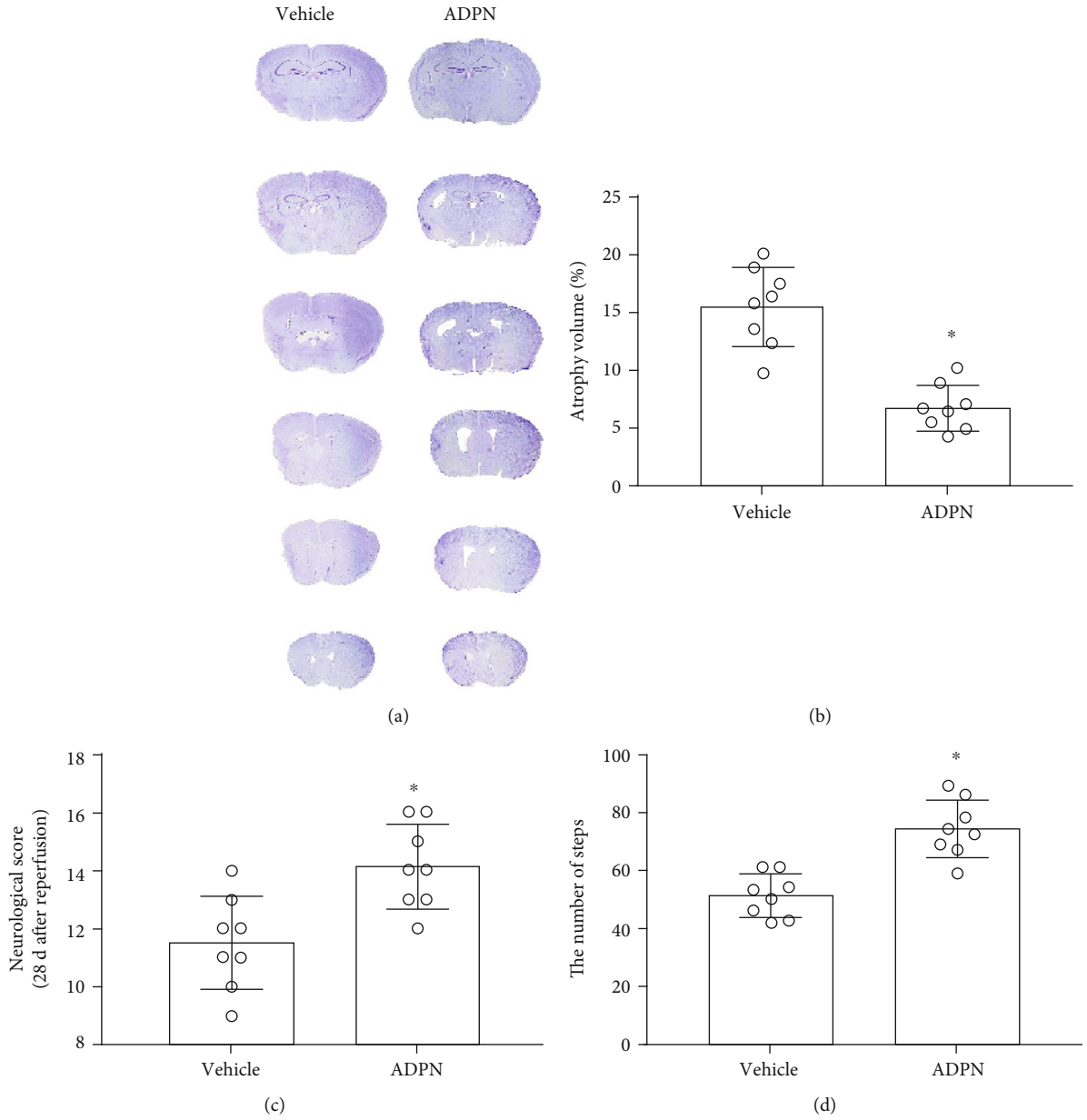

Figure 9: Continued.

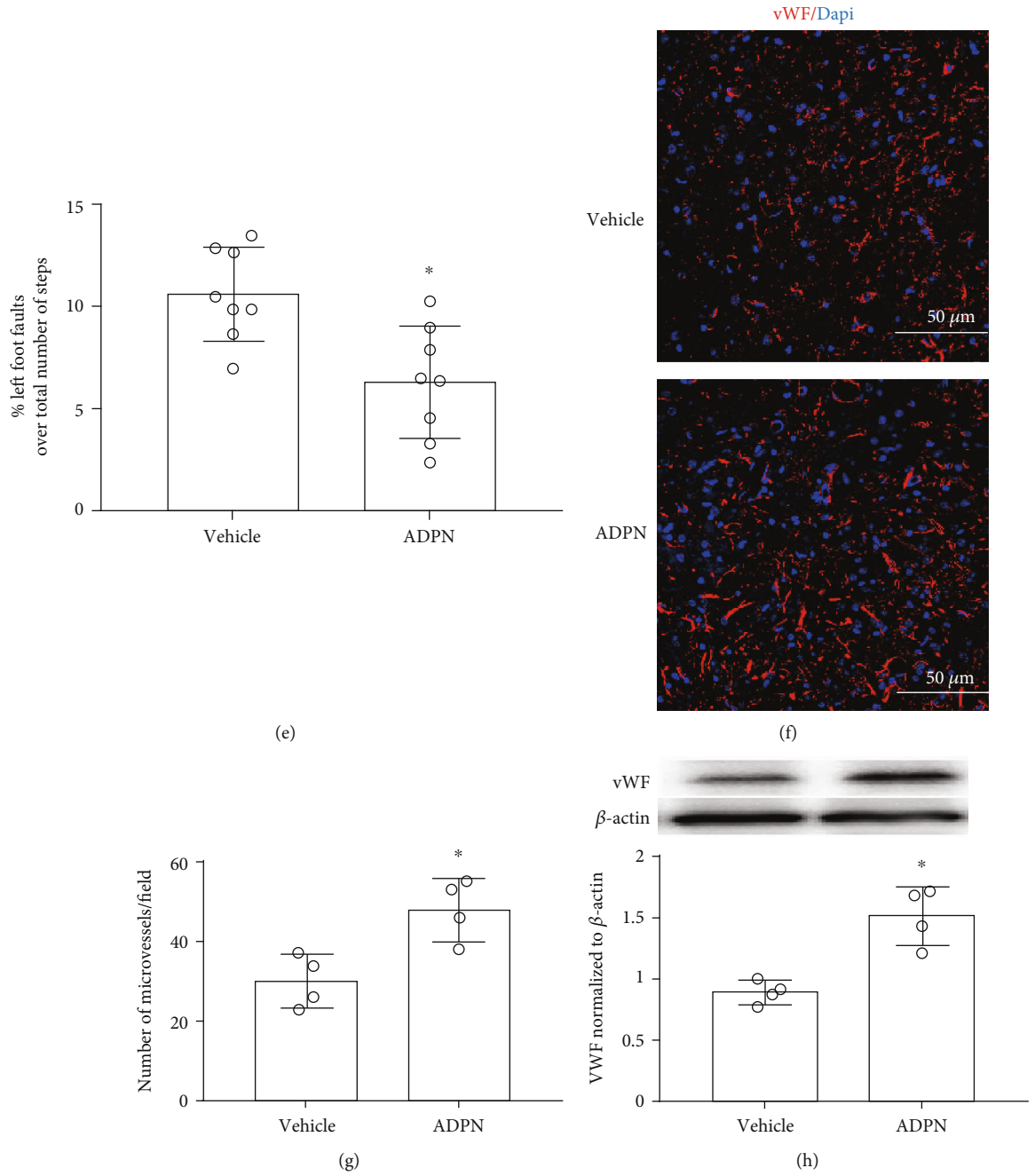

Figure 9: ADPN promoted angiogenesis and improved long-term neurobehavioral outcome. (a) Representative photomicrographs of atrophy volume. (b) The atrophy volume as percentages of the contralateral hemisphere is presented as the mean ± SD and analyzed by one-way ANOVA with Tukey's posttest. (c) The scoring system of Garcia et al. was evaluated on day 28 after reperfusion. The data are presented as the median with interquartile range and analyzed by the *Kruskal-Wallis* test followed by *Dunn's* test. (d) The total steps on day 28 after reperfusion. (e) The error ratio on day 28 after reperfusion. (f) Representative photomicrographs of angiogenesis. (g) Microvessel density statistics. (h) Western blotting analysis of vWF protein expression. These data except for the Garcia et al. score are presented as the mean ± SD and analyzed by one-way ANOVA with Tukey's posttest. $^*P < 0.05$ compared to the vehicle group. $n = 8$ per group.

exogenous ADPN promoted angiogenesis and reduced brain atrophy 28 days after MCAO. Although we did not demonstrate the mechanism of exogenous ADPN on angiogenesis during ischemia, it is possibly related to the HIF-1α/VEGF signaling, as it was reported that ADPN could promote angiogenesis via VEGF in human chondrosarcoma [42].

However, there are always limitations in studies. Since the knockout mice were not used in the present study, this might somewhat cause biased conclusions. To obtain higher validity, further experiments should include conditional gene knockout mice. Also, the effect of ADPN should be testified in both aged and female mice or even mice with

hypertension, for its therapeutic potential. Other limitations include lack of confirming the antioxidant function of EPO and VEGF and lack of examination for receptors of ADPN. Also, the exact molecular mechanism by which ADPN stimulated HIF-1α in ischemia penumbra was unknown, whether the ADPN receptor or other signaling pathway took part in this needs further exploration.

In conclusion, the present study demonstrated that ADPN treatment is effective in attenuation of cerebral ischemia-reperfusion injury, and HIF-1α-regulated antioxidant response is the main molecular mechanism responsible for ADPN treatment for stroke.

Data Availability

The data used to support the findings of this study are included within the article, and further details are available from the corresponding author upon request.

Conflicts of Interest

The authors declare no conflict of interest.

Authors' Contributions

Chan Zhang, Luming Zhen, and Zongping Fang are equally contributed to this work.

Acknowledgments

This work was supported by the National Natural Science Foundation of China (Nos. 81172848 and 81501060) and Natural Science Project of Shaanxi Province (No. 2020JM-330).

Supplementary Materials

Figure S1: the effect of control AAV virus or HIF-1α siRNA AAV virus. (A) Representative photographs of AAV virus expression and (B) the effect verification of HIF-1α siRNA by WB. Data are presented as the mean ± SD and analyzed by t-test followed by Mann–Whitney test. $^*P < 0.05$ compared to ADPN group, $n = 4$ per group. *(Supplementary materials)*

References

[1] J. Kim, T. Thayabaranathan, G. A. Donnan et al., "Global Stroke Statistics 2019," *International Journal of Stroke*, vol. 15, no. 8, pp. 819–838, 2020.

[2] A. Chamorro, U. Dirnagl, X. Urra, and A. M. Planas, "Neuroprotection in acute stroke: targeting excitotoxicity, oxidative and nitrosative stress, and inflammation," *Lancet Neurology*, vol. 15, no. 8, pp. 869–881, 2016.

[3] S. E. Khoshnam, W. Winlow, M. Farzaneh, Y. Farbood, and H. F. Moghaddam, "Pathogenic mechanisms following ischemic stroke," *Neurological Sciences*, vol. 38, no. 7, pp. 1167–1186, 2017.

[4] M. Nishimura, Y. Izumiya, A. Higuchi et al., "Adiponectin prevents cerebral ischemic injury through endothelial nitric oxide synthase dependent mechanisms," *Circulation*, vol. 117, no. 2, pp. 216–223, 2008.

[5] J. Miao, L. H. Shen, Y. H. Tang et al., "Overexpression of adiponectin improves neurobehavioral outcomes after focal cerebral ischemia in aged mice," *CNS Neuroscience & Therapeutics*, vol. 19, no. 12, pp. 969–977, 2013.

[6] H. Bai, L. Zhao, H. Liu et al., "Adiponectin confers neuroprotection against cerebral ischemia-reperfusion injury through activating the cAMP/PKA-CREB-BDNF signaling," *Brain Research Bulletin*, vol. 143, pp. 145–154, 2018.

[7] M. Sasaki, T. Kawano, T. Saito et al., "Hypoadiponectinemia in Patients with Cerebral Infarction: Comparison with Other Atherosclerotic Disorders," *The American Journal of the Medical Sciences*, vol. 333, no. 3, pp. 140–144, 2007.

[8] C. Prugger, G. Luc, B. Haas et al., "Adipocytokines and the risk of ischemic stroke: the PRIME study," *Annals of Neurology*, vol. 71, no. 4, pp. 478–486, 2012.

[9] A. M. MOURÃO, L. C. C. VICENTE, M. N. S. ABREU et al., "Clinical and molecular correlates of the ASPECTS in the acute phase of stroke," *Arquivos de Neuro-Psiquiatria*, vol. 78, no. 5, pp. 262–268, 2020.

[10] B. Chen, W. Q. Liao, N. Xu et al., "Adiponectin protects against cerebral ischemia-reperfusion injury through anti-inflammatory action," *Brain Research*, vol. 1273, pp. 129–137, 2009.

[11] W. Song, T. Huo, F. Guo et al., "Globular adiponectin elicits neuroprotection by inhibiting NADPH oxidase-mediated oxidative damage in ischemic stroke," *Neuroscience*, vol. 248, pp. 136–144, 2013.

[12] H. Fang and R. L. Judd, "Adiponectin regulation and function," *Comprehensive Physiology*, vol. 8, no. 3, pp. 1031–1063, 2018.

[13] S. Wang, J. Wang, H. Wei et al., "Genistein attenuates acute cerebral ischemic damage by inhibiting the NLRP3 inflammasome in reproductively senescent mice," *Frontiers in Aging Neuroscience*, vol. 12, p. 153, 2020.

[14] N. Chen, Z. Zhou, J. Li et al., "3-N-butylphthalide exerts neuroprotective effects by enhancing anti-oxidation and attenuating mitochondrial dysfunction in an in vitro model of ischemic stroke," *Drug Design, Development and Therapy*, vol. Volume 12, pp. 4261–4271, 2018.

[15] S. Wang, F. Ma, L. Huang et al., "Dl-3-n-butylphthalide (NBP): a promising therapeutic agent for ischemic stroke," *CNS & Neurological Disorders Drug Targets*, vol. 17, no. 5, pp. 338–347, 2018.

[16] H. Liu, X. Wu, J. Luo et al., "Adiponectin peptide alleviates oxidative stress and NLRP3 inflammasome activation after cerebral ischemia-reperfusion injury by regulating AMPK/GSK-3beta," *Experimental Neurology*, vol. 329, p. 113302, 2020.

[17] O. Baranova, L. F. Miranda, P. Pichiule, I. Dragatsis, R. S. Johnson, and J. C. Chavez, "Neuron-specific inactivation of the hypoxia inducible factor 1 alpha increases brain injury in a mouse model of transient focal cerebral ischemia," *The Journal of Neuroscience*, vol. 27, no. 23, pp. 6320–6332, 2007.

[18] S. Sarkar, D. Chakraborty, A. Bhowmik, and M. K. Ghosh, "Cerebral ischemic stroke: cellular fate and therapeutic opportunities," *Front Biosci (Landmark Ed)*, vol. 24, pp. 435–450, 2019.

[19] S. Wang, H. Wei, M. Cai et al., "Genistein attenuates brain damage induced by transient cerebral ischemia through up-regulation of ERK activity in ovariectomized mice," *International Journal of Biological Sciences*, vol. 10, no. 4, pp. 457–465, 2014.

[20] J. H. Garcia, S. Wagner, K. F. Liu, and X. J. Hu, "Neurological Deficit and Extent of Neuronal Necrosis Attributable to

Middle Cerebral Artery Occlusion in Rats," *Stroke*, vol. 26, no. 4, pp. 627–635, 1995.

[21] Y. Cai, H. Guo, Z. Fan et al., "Glycogenolysis Is Crucial for Astrocytic Glycogen Accumulation and Brain Damage after Reperfusion in Ischemic Stroke," *iScience*, vol. 23, no. 5, p. 101136, 2020.

[22] S. Ashwal, B. Tone, H. R. Tian, D. J. Cole, and W. J. Pearce, "Core and penumbral nitric oxide synthase activity during cerebral ischemia and reperfusion," *Stroke*, vol. 29, no. 5, pp. 1037–1047, 1998, discussion 1047.

[23] S. P. Efstathiou, D. I. Tsioulos, A. G. Tsiakou, Y. E. Gratsias, A. V. Pefanis, and T. D. Mountokalakis, "Plasma adiponectin levels and five-year survival after first-ever ischemic stroke," *Stroke*, vol. 36, no. 9, pp. 1915–1919, 2005.

[24] M. Almagor, I. Ivnitzki, H. Yaffe, and M. Baras, "Changes in semen quality in Jerusalem between 1990 and 2000: a cross-sectional and longitudinal study," *Archives of Andrology*, vol. 49, no. 2, pp. 139–144, 2003.

[25] K. Yatomi, N. Miyamoto, M. Komine-Kobayashi et al., "Pathophysiological dual action of adiponectin after transient focal ischemia in mouse brain," *Brain Research*, vol. 1297, pp. 169–176, 2009.

[26] Y. Okamoto, Y. Arita, M. Nishida et al., "An adipocyte-derived plasma protein, adiponectin, adheres to injured vascular walls," *Hormone and Metabolic Research*, vol. 32, no. 2, pp. 47–50, 2000.

[27] E. D. Kryl'skii, T. N. Popova, O. A. Safonova, A. O. Stolyarova, G. A. Razuvaev, and M. A. P. de Carvalho, "Transcriptional regulation of antioxidant enzymes activity and modulation of oxidative stress by melatonin in rats under cerebral ischemia / reperfusion conditions," *Neuroscience*, vol. 406, pp. 653–666, 2019.

[28] S. M. Davis and K. R. Pennypacker, "Targeting antioxidant enzyme expression as a therapeutic strategy for ischemic stroke," *Neurochemistry International*, vol. 107, pp. 23–32, 2017.

[29] B.-l. Ya, Q. Liu, H.-f. Li et al., "Uric acid protects against focal cerebral ischemia/reperfusion-induced oxidative stress via activating Nrf2 and regulating neurotrophic factor expression," *Oxidative Medicine and Cellular Longevity*, vol. 2018, Article ID 6069150, 10 pages, 2018.

[30] M. Cai, Y. Guo, S. Wang et al., "Tanshinone IIA elicits neuroprotective effect through activating the nuclear factor erythroid 2-related factor-dependent antioxidant response," *Rejuvenation Research*, vol. 20, no. 4, pp. 286–297, 2017.

[31] T. Higashida, C. Peng, J. Li et al., "Hypoxia-inducible factor-1alpha contributes to brain edema after stroke by regulating aquaporins and glycerol distribution in brain," *Current Neurovascular Research*, vol. 8, no. 1, pp. 44–51, 2011.

[32] A. Merelli, J. C. G. Rodríguez, J. Folch, M. R. Regueiro, A. Camins, and A. Lazarowski, "Understanding the role of hypoxia inducible factor during neurodegeneration for new therapeutics opportunities," *Current Neuropharmacology*, vol. 16, no. 10, pp. 1484–1498, 2018.

[33] Q. Zhang, H. Bian, Y. Li, L. Guo, Y. Tang, and H. Zhu, "Preconditioning with the traditional Chinese medicine Huang-Lian-Jie-Du-Tang initiates HIF-1alpha-dependent neuroprotection against cerebral ischemia in rats," *Journal of Ethnopharmacology*, vol. 154, no. 2, pp. 443–452, 2014.

[34] S. Guo, M. Miyake, K. J. Liu, and H. Shi, "Specific inhibition of hypoxia inducible factor 1 exaggerates cell injury induced by in vitro ischemia through deteriorating cellular redox environment," *Journal of Neurochemistry*, vol. 108, no. 5, pp. 1309–1321, 2009.

[35] M. W. Halterman, C. C. Miller, and H. J. Federoff, "Hypoxia-inducible factor-1alpha mediates hypoxia-induced delayed neuronal death that involves p53," *The Journal of Neuroscience*, vol. 19, no. 16, pp. 6818–6824, 1999.

[36] S. Bok, Y. E. Kim, Y. Woo et al., "Hypoxia-inducible factor-1alpha regulates microglial functions affecting neuronal survival in the acute phase of ischemic stroke in mice," *Oncotarget*, vol. 8, no. 67, pp. 111508–111521, 2017.

[37] H. Wang, F. Niu, W. Fan, J. Shi, J. Zhang, and B. Li, "Modulating effects of preconditioning exercise in the expression of ET-1 and BNP via HIF-1alpha in ischemically injured brain," *Metabolic Brain Disease*, vol. 34, no. 5, pp. 1299–1311, 2019.

[38] P. Katavetin, K. Tungsanga, S. Eiam-Ong, and M. Nangaku, "Antioxidative effects of erythropoietin," *Kidney International*, vol. 72, pp. S10–S15, 2007.

[39] R. Chen, C. Lee, X. Lin, C. Zhao, and X. Li, "Novel function of VEGF-B as an antioxidant and therapeutic implications," *Pharmacological Research*, vol. 143, pp. 33–39, 2019.

[40] M. Hatakeyama, I. Ninomiya, and M. Kanazawa, "Angiogenesis and neuronal remodeling after ischemic stroke," *Neural Regeneration Research*, vol. 15, no. 1, pp. 16–19, 2020.

[41] L. Shen, J. Miao, F. Yuan et al., "Overexpression of adiponectin promotes focal angiogenesis in the mouse brain following middle cerebral artery occlusion," *Gene Therapy*, vol. 20, no. 1, pp. 93–101, 2013.

[42] H. P. Lee, C. Y. Lin, J. S. Shih et al., "Adiponectin promotes VEGF-A-dependent angiogenesis in human chondrosarcoma through PI3K, Akt, mTOR, and HIF-alpha pathway," *Oncotarget*, vol. 6, no. 34, pp. 36746–36761, 2015.